Applications of the Periodic Electrostatic Embedded Cluster Method to Solid State Actinide Chemistry

Joseph Paul William Wellington

For the degree of

EngD Molecular Modelling and Materials Science

UCL

May, 2017

I, Joseph Paul William Wellington confirm that the work presented in this thesis is my own. Where information has been derived from other sources, I confirm that this has been indicated in the thesis.

Abstract

The work described in this thesis uses density functional theory (DFT) with an embedded cluster method, known as the periodic electrostatic embedded cluster method (PEECM) to study solid state actinide systems. The theoretical background of electronic structure calculations is discussed in the first chapter, while the remaining chapters deal with results of the studies.

In Chapter 2 the PEECM is used to include long-range electrostatic interactions in calculations of Quantum Theory of Atoms in Molecules (QTAIM) bond critical point and delocalisation index metrics for the actinide-element bonds in $Cs_2UO_2Cl_4$, $U(Se_2PPh_2)_4$ and $Np(Se_2PPh_2)_4$. The effects of the environment are seen to be minor, suggesting they do not account for the differences previously observed between the experimental and theoretical QTAIM data.

In Chapter 3 the electronic structure of actinide dioxide systems has been investigated by examining the projected density of states (PDOS). While PBE incorrectly predicts these systems to be metallic, PBE0 finds them to be insulators, with the composition of the valence and conduction levels agreeing well with experiment.

In Chapter 4 molecular and dissociative water adsorption on the (111) and (110) surfaces of UO_2 and PuO_2 has been investigated, with that on the (110) surface being stronger than on the (111). Similar energies are found for molecular and dissociative adsorption on the (111) surfaces, while on the (110) there is a clear preference for dissociative adsorption. Adsorption energies and geometries on the (111) surface of UO_2 are in good agreement with recent periodic DFT studies using the GGA+*U* approach.

In Chapter 5 oxygen vacancies are investigated on the actinide oxide surfaces. Oxygen vacancy formation energies are found to be much greater on UO_2 than PuO_2 surfaces. Oxygen vacancies lead to a preference for dissociative adsorption of water on both the (111) and (110) surfaces, with adsorption energies being much greater on PuO_2 than UO_2 surfaces.

Acknowledgements

Firstly I wish to thank my supervisors, Nik Kaltsoyannis and Andy Kerridge, for their continuous guidance, support, and patience during this project. Nik has supervised me for five years, through two Masters and an EngD project and throughout this time he has provided much needed assistance and encouragement. I want to thank Andy not only for his technical assistance, teaching me how to run the calculations in this project, but also for the insight he has offered throughout.

I would like to thank the National Nuclear Laboratory for providing funding. In particular I am grateful to my industrial supervisors Scott Owens and Jonathan Austin who also provided essential expertise.

I want to thank the Centre for Doctoral Training in Molecular Modelling and Materials Science at UCL whose funding has allowed me to attend various conferences in the UK and abroad.

I have been very lucky to have shared an office with so many great people over the course of my EngD and so I must thank all the inhabitants of G19 and the whole chemistry department at UCL – in particular Abi, Eszter, Eamonn, Toby, Poppy, Belle, and Rona who have made the experience so enjoyable.

I am grateful to my friends, who may not have provided any chemical insight to this thesis, but who are always the greatest distractions.

Finally I want to thank my family, to Katie and James for always looking out for me. To Jack for always making me laugh, and for his limitless encouragement while I wrote this thesis. And to my parents, Kay and Paul, who have supported me the whole way, for which I am truly grateful.

Contents

List of Figures

List of Tables

Introduction

The work in this thesis is comprised of studies of solid state actinide systems, and this introduction will give a brief overview of this series of elements. More detailed introductions on the chemistry and background of particular actinide systems will be given at the beginning of each results chapter.

The actinides, a group made up of metal elements with atomic numbers 89-103, lack the detailed study of other parts of the periodic table. They are all radioactive, often hard to obtain (the transuranic elements generally do not occur naturally), and as the actinide series is crossed they become increasingly short-lived, all of which make experimental studies of them difficult.

However, there is a clear interest in the actinide elements, in particular due to their use in the nuclear fuel cycle. Uranium, in the form of uranium dioxide, is used as fuel in most nuclear reactors, while many of the transuranic actinides are formed due to neutron capture steps in nuclear reactors. Plutonium, which due to neutron capture by uranium forms a small but important proportion of used nuclear fuel, also has an important role in the nuclear industry. It can be recycled with UO_2 to form mixed oxide (MOX) fuel which can be used in certain reactors. If it is not reused in MOX fuel then it poses a significant storage problem due to its radiotoxicity and the long half-lives of some of its isotopes (Pu-239 has a half-life of 24,000 years).

The actinides are also of interest due to their unique chemistry. In contrast to the lanthanides, the actinide series show a great deal of variety: the early actinides have a wide range of oxidation states, this can be seen in Figure I.1.1 which shows known oxidation states of the actinides. For example while Neptunium is most commonly found in the +5 oxidation state, and Plutonium in the +4, they both form compounds with oxidation states ranging from +2 to +7. This range in oxidation states is due to the closeness in energy of the 5f and 6d orbitals. The later actinides (from Curium onwards), however, act more like lanthanides mainly adopting the +3 oxidation state (Figure I.1.1).

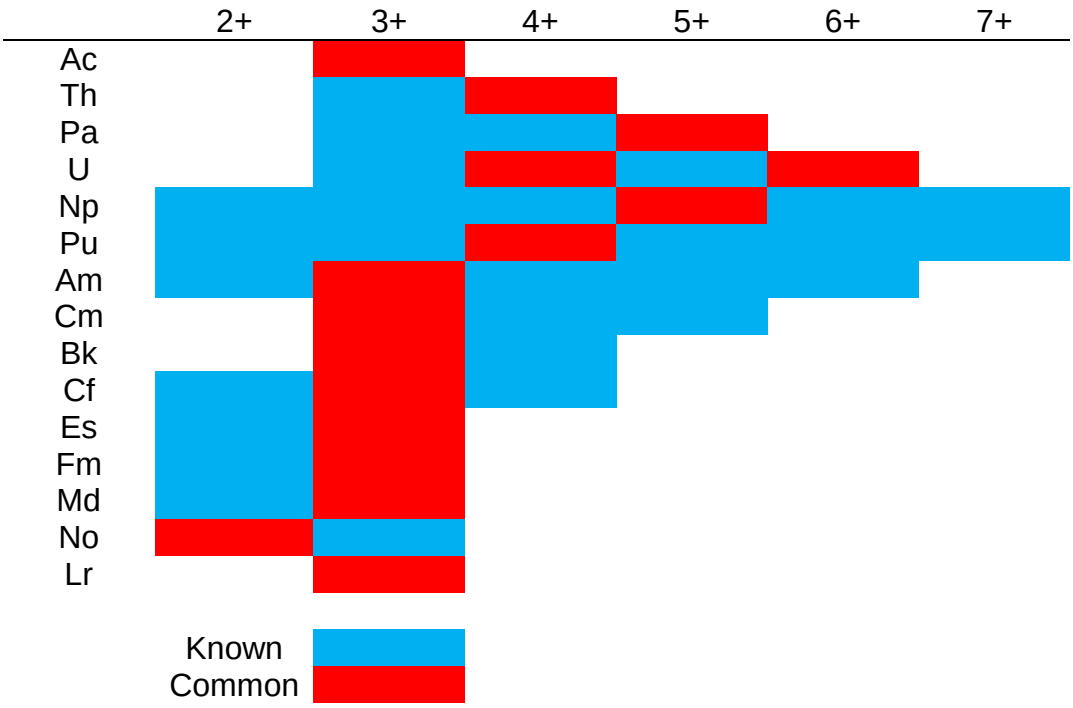

Figure I.1.1 Oxidation states of the actinides, adapted from ref.[1] Red indicates the most common oxidation states for each actinide, while blue indicates oxidation states that are known for each.

The variable oxidation state of the early actinides is attributed to a relative destabilisation of the 5f orbitals, as they contain a radial node (compared to 4f orbitals which have no radial nodes). This destabilisation of the 5f orbitals makes them chemically available, and there is good evidence for covalent character in the bonding of the early actinides. For these reasons the early actinides have been compared with the transition metals.

As the actinide group is crossed their ionic radii decrease (Figure I.1.2), an effect known as the actinide contraction. This effect is due to the poor shielding of the f electrons, therefore as the f orbitals are filled the effective nuclear charge for the valence electrons increases and the valence electrons are stabilised. This contraction also causes the later actinides to have less variable oxidation states.

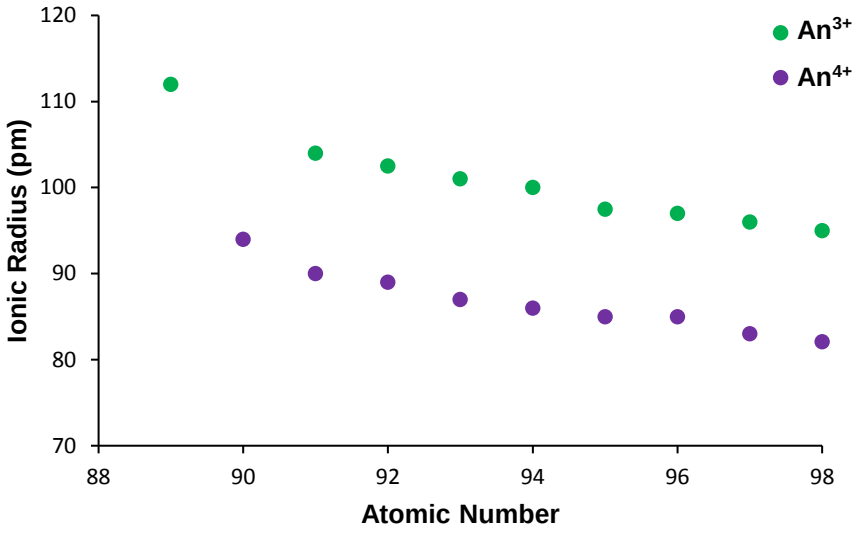

Figure I.1.2 Ionic radii of An^{3+} and An^{4+} actinide ions, data from[2]

Due to the difficulty in gaining empirical data on actinides, computational studies can provide important insight and help to aid understanding where experimental results are lacking or limited. This thesis involves investigations into solid state systems containing uranium, neptunium and plutonium, all elements towards the beginning of the actinide series.

Most quantum chemical studies of solid state actinide systems use periodic DFT, however alternative approaches can offer additional insights. Embedded cluster methods provide some particular advantages: the relatively simple implementation of QTAIM to solid state actinide systems, the study of defects in in isolation, and the computationally efficient (compared to periodic DFT) use of hybrid functionals.

The work in Chapter 2 investigates whether long-range electrostatic effects need to be considered when performing Quantum Theory of Atoms in Molecules calculations on actinide systems, this work has been published in the journal Polyhedron.[3] Chapter 3 focuses on using embedded cluster calculations to find the correct electronic structure of actinide dioxide systems. The work in Chapter 4 looks at the low index surfaces of actinide dioxide systems, in particular how water adsorbs on these surfaces. The work in Chapters 3 and 4 has been published in the Journal of Nuclear Materials[4] and a small subsection of the work in Chapter 4 was presented for a paper[5] at the Waste Management 2016

conference in Arizona. The work in Chapter 5 looks at how oxygen defects affect actinide dioxide systems, in particular what effect they have on water adsorption at the surface, this work is currently being written up for publication.

1 Theoretical Background

The aim of this first chapter is to give a brief overview of electronic structure theory, and in particular density functional theory, as well as particular computational methods used in this thesis. A more detailed description of the ideas discussed here can be found in quantum and computational chemistry textbooks[6–10] that have been used in the writing of this chapter.

1.1 Electronic Structure Theory

1.1.1 The Schrödinger Equation

The total energy, E, of a system with wavefunction, Ψ, is described by the non-relativistic time-independent Schrödinger equation (SE):

$$\hat{H}\Psi = E\Psi \tag{1.1}$$

The SE is an eigenvalue equation where Ψ and E are the eigenfunctions and eigenvalues respectively and $\hat{H}$ is the Hamiltonian operator for the non-relativistic time-independent SE given by (in atomic units):

$$\begin{aligned}\hat{H} &= \hat{T}_{\mathrm{n}} + \hat{T}_{\mathrm{e}} + \hat{V}_{\mathrm{ne}} + \hat{V}_{\mathrm{ee}} + \hat{V}_{\mathrm{nn}} \\ &= -\frac{1}{2}\sum_{A=1}^{M}\frac{1}{M_A}\nabla_A^2 - \frac{1}{2}\sum_{i=1}^{N}\nabla_i^2 - \sum_{i=1}^{N}\sum_{A=1}^{M}\frac{Z_A}{r_{iA}} + \sum_{i=1}^{N}\sum_{j>i}^{N}\frac{1}{r_{ij}} + \sum_{A=1}^{M}\sum_{B>A}^{M}\frac{Z_A Z_B}{r_{AB}}\end{aligned} \tag{1.2}$$

where $\hat{T}_{\mathrm{n}}$ is the kinetic energy operator for the nuclei and $\hat{T}_{\mathrm{e}}$ is the kinetic energy operator for the electrons in the system. The $\hat{V}$ terms are the potential energy operators, $\hat{V}_{\mathrm{ne}}$ for the attractive interactions between the electrons and the nuclei, and $\hat{V}_{\mathrm{ee}}$ and $\hat{V}_{\mathrm{nn}}$ for the repulsive electron–electron and nucleus–nucleus interactions respectively. M_A is the mass of nucleus A; Z_A the charge on nucleus A; and r_{iA}, r_{ij}, and r_{AB} the distances between electron i and nucleus A, electrons i and j, and nuclei A and B respectively.

The SE is too complicated to solve analytically for non-hydrogenic systems, where there is more than one electron, and so certain approximations must be made. The nuclei are much heavier than the electrons and consequently the

electrons move much faster than the nuclei; therefore we can assume that the electrons will react instantaneously to any motion of the nuclei. From this we can consider the movement of the nuclei and electrons separately and solve the SE for the electrons with the nuclei at fixed positions, this is known as the Born-Oppenheimer approximation. This approximation allows us to simplify (1.2): $\hat{T}_{\mathrm{n}} = 0$ and we can leave out $\hat{V}_{\mathrm{nn}}$ as it is a constant, allowing us to define an electronic time-independent SE:

$$\hat{H}_{\mathrm{elec}}\Psi = E_{\mathrm{elec}}\Psi \tag{1.3}$$

where

$$\begin{aligned}\hat{H}_{\mathrm{elec}} &= \hat{T}_{\mathrm{e}} + \hat{V}_{\mathrm{ne}} + \hat{V}_{\mathrm{ee}} \\ &= -\frac{1}{2}\sum_{i=1}^{N}\nabla_i^2 - \sum_{i=1}^{N}\sum_{A=1}^{M}\frac{Z_A}{r_{iA}} + \sum_{i=1}^{N}\sum_{j>i}^{N}\frac{1}{r_{ij}}\end{aligned} \tag{1.4}$$

The total wavefunction, $\Psi(\mathbf{x}_1, \mathbf{x}_2, \ldots, \mathbf{x}_{\mathrm{n}})$, can be formed from one electron wavefunctions, such as molecular orbitals or spin orbitals, $\phi_i(\mathbf{x}_i)$, (a spin orbital is the product of a spatial function, ψ_i, and a spin function, α or β, where $\mathbf{x}_i$ contains both spin and space coordinates, $\mathbf{x} = \{\mathbf{r}, \omega\}$, ω is the spin coordinate, which can be either α or β.) The simplest way to form the total wavefunction from one electron spin orbitals is to take the Hartree product:

$$\Psi(\mathbf{x}_1, \mathbf{x}_2, \ldots, \mathbf{x}_n) = \prod_{i=1}^{n}\phi_i(\mathbf{x}_i) \tag{1.5}$$

The antisymmetry principle, which states that a wavefunction describing fermions – such as electrons – must be antisymmetric when we interchange a set of space-spin coordinates for any pair of electrons, however, is not satisfied by our wavefunction. For example, when we have a two electron system and interchange the coordinates,

$$\Psi(\mathbf{x}_1, \mathbf{x}_2) = \phi_1(\mathbf{x}_1)\phi_2(\mathbf{x}_2) \tag{1.6}$$

$$\Psi(\mathbf{x}_2, \mathbf{x}_1) = \phi_1(\mathbf{x}_2)\phi_2(\mathbf{x}_1) \tag{1.7}$$

the wavefunction remains unchanged. Furthermore, the Hartree product implies that the electrons are distinguishable, i.e. electron 1 is in orbital a, electron 2 in orbital b, etc.

To obey the antisymmetry principle we can use a Slater determinant to describe the wavefunction:

$$\Psi_{\mathrm{SD}}(\mathbf{x}_1, \mathbf{x}_2, \ldots, \mathbf{x}_n) = \frac{1}{\sqrt{N!}} \begin{vmatrix} \phi_1(\mathbf{x}_1) & \phi_2(\mathbf{x}_1) & \ldots & \phi_n(\mathbf{x}_1) \\ \phi_1(\mathbf{x}_2) & \phi_2(\mathbf{x}_2) & \ldots & \phi_n(\mathbf{x}_2) \\ \vdots & \vdots & \ddots & \vdots \\ \phi_1(\mathbf{x}_n) & \phi_2(\mathbf{x}_n) & \ldots & \phi_n(\mathbf{x}_n) \end{vmatrix} \tag{1.8}$$

The columns in the Slater determinant are for a given spin orbital (ϕ_n), while the rows are for a given electron ($\mathbf{x}_n$). The properties of determinants make them useful to describe the wavefunction: if we exchange the coordinates of two electrons we will get a change in sign of the whole wavefunction and so the wavefunction now obeys the antisymmetry principle. Also, if any two lines of a determinant are the same the determinant is zero, hence no two electrons can have the same spatial and spin coordinates, satisfying the Pauli exclusion principle. Using a single determinant, however, implies that the coordinates of a particular electron are independent of the other electrons in our system, we will come back to this point later.

How do we decide on the form of the spin orbitals? One way is to expand the spin orbitals from a set of atom centred basis functions, known as Linear Combination of Atomic Orbitals (LCAO):

$$\phi_i = \sum_{k=1}^{n_{\mathrm{basis}}} c_{ik}\chi_k \tag{1.9}$$

where c_{ik} are coefficients and χ_k are the atom centred basis functions, or atomic orbitals, the form of the basis functions will be discussed in more detail in Section 1.2.4. The basis functions do not need to be atom centred but it can lead to useful chemical conclusions.

We need a way to decide what wavefunction best describes the system. The energy with a particular wavefunction Ψ will always be higher than the true ground

state energy, E_0, therefore if we minimise the energy with respect to Ψ by altering the coefficients of the basis functions, we can find the best estimate for the ground state wave function. This is known as the variation principle. The energy of the wavefunction is given by:

$$E_{\text{elec}} = \frac{\int \Psi(\mathbf{x}) \hat{H}_{\text{elec}} \Psi(\mathbf{x}) dx}{\int \Psi(\mathbf{x}) \Psi(\mathbf{x}) dx} \tag{1.10}$$

or more simply if the wavefunction is normalised,

$$\begin{aligned} E_{\text{elec}} &= \int \Psi(\mathbf{x}) \hat{H}_{\text{elec}} \Psi(\mathbf{x}) dx \\ &= \langle \Psi(\mathbf{x}) | \hat{H}_{\text{elec}} | \Psi(\mathbf{x}) \rangle \end{aligned} \tag{1.11}$$

1.1.2 Hartree-Fock Theory

The idea behind Hartree-Fock Theory is that instead of trying to solve the many electron SE, we solve a series of one-electron equations for each of the one-electron molecular orbitals.

In order to simplify $\hat{H}_{\text{elec}}$ we define operators that act on the one-electron molecular orbitals. Firstly we define a one-electron operator, $\hat{h}_i$, which is due to contributions from the electron kinetic energy and the attraction between the electrons and the nuclei. This operator is independent of the other electrons in the system, only depending on the electron in orbital i and the nuclear positions:

$$\hat{h}_i = -\frac{1}{2} \nabla_i^2 - \sum_{A=1}^{M} \frac{Z_A}{r_{iA}} \tag{1.12}$$

Two-electron operators are also defined, $\hat{J}_j$, the Coulomb operator, and $\hat{K}_j$, the exchange operator. These operators are not independent of the other electrons as they depend on the electron in orbital j:

$$\hat{J}_j |\phi_i(\mathbf{x}_1)\rangle = \langle \phi_j(\mathbf{x}_2) | \frac{1}{r_{12}} | \phi_j(\mathbf{x}_2) \rangle | \phi_i(\mathbf{x}_1) \rangle \tag{1.13}$$

$$\widehat{K}_j|\phi_i(\mathbf{x}_1)\rangle = \left\langle \phi_j(\mathbf{x}_2)\left|\frac{1}{r_{12}}\right|\phi_i(\mathbf{x}_2)\right\rangle|\phi_j(\mathbf{x}_1)\rangle \tag{1.14}$$

The Hartree-Fock energy is then calculated with the following equation:

$$\begin{aligned} E_{\mathrm{HF}} &= \langle \Psi_{\mathrm{SD}}|\widehat{H}_{\mathrm{HF}}|\Psi_{\mathrm{SD}}\rangle \\ &= \sum_{i=1}^{N} h_{ii} + \frac{1}{2}\sum_{i=1}^{N}\sum_{j=i}^{N}(J_{ij} - K_{ij}) \end{aligned} \tag{1.15}$$

where Ψ_{SD} is a wavefunction composed of a single Slater determinant. J_{ij} and K_{ij} are the Coulomb and exchange integrals respectively (the factor of ½ avoids double counting) and are related to the one- and two-electron operators described by

$$h_{ii} = \int \phi_i(\mathbf{x}_1)\hat{h}_i\phi_i(\mathbf{x}_1)\, d\mathbf{x}_1 \tag{1.16}$$

$$\begin{aligned} J_{ij} &= \langle \phi_i(\mathbf{x}_1)|\hat{J}_j|\phi_i(\mathbf{x}_1)\rangle \\ &= \iint |\phi_i(\mathbf{x}_1)|^2 \frac{1}{r_{12}} |\phi_j(\mathbf{x}_2)|^2 d\mathbf{x}_1 d\mathbf{x}_2 \end{aligned} \tag{1.17}$$

$$\begin{aligned} K_{ij} &= \langle \phi_i(\mathbf{x}_1)|\widehat{K}_j|\phi_i(\mathbf{x}_1)\rangle \\ &= \iint \phi_i^*(\mathbf{x}_1)\phi_j^*(\mathbf{x}_2)\frac{1}{r_{12}}\phi_i(\mathbf{x}_2)\phi_j(\mathbf{x}_1) d\mathbf{x}_1 d\mathbf{x}_2 \end{aligned} \tag{1.18}$$

The Coulomb integral represents the classical Coulombic interaction of an electron in orbital ϕ_i with an electron in orbital ϕ_j, whereas the exchange integral has no classical analogy. It is important to note that the interaction of an electron with all the other electrons in the system is by means of effective one-electron potentials, meaning that the electron experiences only the charge distribution associated with all other electrons, rather than instantaneous electron-electron interactions. This is an approximation, the electrons do not interact with a distribution of the other electrons but their positions are correlated to each other. At the end of this section I will briefly discuss the implications of this and methods to overcome it. It is also important to note that if $i = j$, then $J_{ij} = K_{ij}$, for this case the Coulomb and exchange integrals in (1.15) cancel each other out, hence there is no interaction of the electron with itself.

We now have a way to calculate the Hartree-Fock energy given a single determinantal wavefunction, but how do we find the wavefunction that gives the ground state energy? From the variation principle we need to minimize the energy with respect to the wavefunction, or more specifically the coefficients of the molecular orbitals. We do the minimization process subject to the constraint that the molecular orbitals remain orthonormal:

$$\langle \phi_i | \phi_j \rangle = \delta_{ij} \tag{1.19}$$

This constraint is achieved with a Lagrange multiplier which leads to the one-electron Hartree-Fock equations:

$$\begin{aligned} \hat{f}_i(\mathbf{x}_1)\phi_i(\mathbf{x}_1) &= \epsilon_i \phi_i(\mathbf{x}_1) \\ \hat{f}(\mathbf{x}_1) &= \hat{h}_i(\mathbf{x}_1) + \sum_j [\hat{J}_j(\mathbf{x}_1) - \hat{K}_j(\mathbf{x}_1)] \end{aligned} \tag{1.20}$$

$\hat{f}(\mathbf{x}_1)$ is the Fock operator and ϵ_i the energy of the orbital i. The Fock operator, however, depends on all the molecular orbitals through the Coulomb and exchange operators, hence to find the solution to the HF equations and obtain the molecular orbitals, we need to know the resulting molecular orbitals. Therefore the HF equations must be solved iteratively, an initial guess at the wavefunction is made, providing orbitals to use for the Fock operator, the HF equations are then solved to produce new orbitals, and the process is repeated until the difference between the orbitals used at the beginning of a cycle are within a convergence criteria of the resulting orbitals, and the system is deemed self-consistent.

One important thing to note from HF theory is the approximation of using a single Slater determinant to describe the wavefunction. This means the interactions between electrons are treated in an average way, as described above. The use of a single determinant neglects the fact that the motion of the electrons is correlated – on average they are further apart than described in HF theory. Due to this, even in the limit of an infinite basis set, the HF energy will always be higher than the true ground state energy and the difference between these two values is the correlation energy and accounts for ~1% of the total energy.

$$E_{\text{correlation}} = E_0 - E_{\text{HF}} \tag{1.21}$$

There are many methods which go beyond HF theory and include correlation energy including configuration interaction, second order Møller–Plesset perturbation theory (MP2), and coupled cluster calculations, however a discussion of these methods is beyond the scope of this thesis. Correlation energy is also included, to a certain degree, in density functional theory (DFT), the topic of the next section.

1.2 Density Functional Theory

Wavefunction based methods for solving quantum mechanical calculations become computationally very expensive in larger systems, this is due to the fact that for a system containing N electrons there are $3N$ spatial variables. DFT uses the electronic density to calculate molecular properties instead of the electronic wavefunction, and the electron density depends on only three spatial variables independent of how many electrons there are in the system.

1.2.1 Hohenberg-Kohn Theorems

DFT is founded on two theorems by Hohenberg and Kohn.[11] The first theorem states that the ground state electronic density, $\rho(\boldsymbol{r})$, of a system uniquely determines the external potential, $V_{\text{ext}}(\mathbf{r})$, and therefore determines all the ground state properties of the system including the ground state energy, E_0. The second Hohenberg-Kohn theorem states that for a trial density, $\rho(\mathbf{r}')$, $E_0 \leq E[\rho(\mathbf{r}')]$, which is an expression of the variation principle in terms of the electron density, where $E[\rho(\mathbf{r}')]$ is the energy of the system with density $\rho(\mathbf{r}')$. The ground state density is then found by minimizing $E[\rho(\mathbf{r}')]$ with respect to $\rho(\mathbf{r}')$, while fulfilling certain criteria such as having a constant number of electrons.

The total energy of an interacting system of electrons is then reformulated in terms of the electron density:

$$E[\rho(\mathbf{r})] = T[\rho(\mathbf{r})] + \int V_{\text{ext}}(\mathbf{r})\rho(\mathbf{r})\,\mathrm{d}\mathbf{r} + V_{\text{ee}}[\rho(\mathbf{r})] \tag{1.22}$$

where $T[\rho(\mathbf{r})]$ is the kinetic energy of a system with density $\rho(\mathbf{r})$; $\int V_{\text{ext}}(\mathbf{r})\rho(\mathbf{r})d\mathbf{r}$ the interaction energy between the nuclei and the electrons; and $V_{\text{ee}}[\rho(\mathbf{r})]$ is the

interaction energy between electrons, including Coulomb, exchange and correlation energies.

As a function depends on a variable, for example the value of the electronic density ρ depends on the value of the variable $\mathbf{r}$; a functional depends on the value of a function. Hence the energy depends on the electronic density, therefore $E[\rho(\mathbf{r})]$ is a functional of the electronic density, which is why it is called density functional theory.

We can group the energy functionals together and rewrite (1.22) as

$$E[\rho(\mathbf{r})] = \int V_{\text{ext}}(\mathbf{r})\rho(\mathbf{r})d\mathbf{r} + F[\rho(\mathbf{r})] \tag{1.23}$$

where

$$F[\rho(\boldsymbol{r})] = T[\rho(\boldsymbol{r})] + V_{\text{ee}}[\rho(\boldsymbol{r})] \tag{1.24}$$

$F[\rho(\boldsymbol{r})]$ is a universal functional of the electronic density; it represents the kinetic energy and the electron-electron interaction energy. With the exact form of $F[\rho(\mathbf{r})]$ the ground state energy could be calculated from its electronic density, in the limit of Born-Oppenheimer and relativistic approximations, however the exact form of the functional is unknown and approximations must be made. The difference between DFT methods is how they approximate this functional, as will be discussed later.

1.2.2 Kohn-Sham DFT

Kohn and Sham simplified the many-body problem of interacting electrons in an external field of the nuclei, $V_{\text{ext}}(\mathbf{r})$, by considering a non-interacting system of electrons in an effective potential, which has the same electron density as the interacting system[12]. We first consider the energy of the non-interacting system:

$$E[\rho(\mathbf{r})] = T_{\text{ni}}[\rho(\mathbf{r})] + \int V_{\text{ext}}(\mathbf{r})\rho(\mathbf{r})d\mathbf{r} \tag{1.25}$$

Here $T_{\text{ni}}[\rho(\mathbf{r})]$ is the kinetic energy of a fictitious system of non-interacting electrons, with the same electron density as the interacting system, $\rho(\mathbf{r})$. As this

is a system of non-interacting electrons there is no $V_{\mathrm{ee}}[\rho(\mathbf{r})]$ term. The ground state of the system of non-interacting electrons in the potential $V_{\mathrm{ext}}(\mathbf{r})$ is then found by solving the Schrödinger equation for the one-electron Hamiltonian;

$$\hat{h}_{\mathrm{ni}}\varphi_i = \left(-\frac{1}{2}\nabla^2 + V_{\mathrm{ext}}(\mathbf{r})\right)\varphi_i = \varepsilon_i\varphi_i \tag{1.26}$$

φ_i are one-electron spin-orbitals which are treated in a LCAO expansion (as for HF theory), hence Kohn and Sham introduced orbitals into the problem. The electron density for a system with orbitals φ_i is then given by

$$\rho(\mathbf{r}) = \sum_i^n |\varphi_i(\mathbf{r})|^2 \tag{1.27}$$

The kinetic energy of the non-interacting system is then defined as

$$T_{\mathrm{ni}}[\rho(\mathbf{r})] = \sum_{i=1}^{N} \langle \varphi_i \left| -\frac{1}{2}\nabla^2 \right| \varphi_i \rangle \tag{1.28}$$

The energy of an interacting system can now be rewritten including the non-interacting kinetic energy term:

$$E[\rho(\mathbf{r})] = T_{\mathrm{ni}}[\rho(\mathbf{r})] + \int V_{\mathrm{ext}}(\mathbf{r})\rho(\mathbf{r})d\mathbf{r} + J[\rho(\mathbf{r})] + E_{\mathrm{xc}}[\rho(\mathbf{r})] \tag{1.29}$$

where the universal functional $F[\rho(\boldsymbol{r})]$ is now

$$F[\rho(\boldsymbol{r})] = T_{\mathrm{ni}}[\rho(\boldsymbol{r})] + J[\rho(\boldsymbol{r})] + E_{\mathrm{xc}}[\rho(\boldsymbol{r})] \tag{1.30}$$

$J[\rho(\boldsymbol{r})]$is the classical Coulomb repulsion energy between electrons and $E_{xc}[\rho(\boldsymbol{r})]$ is the exchange-correlation energy defined as:

$$E_{\mathrm{xc}}[\rho(\mathbf{r})] = T[\rho(\mathbf{r})] - T_{\mathrm{ni}}[\rho(\mathbf{r})] + V_{\mathrm{ee}}[\rho(\mathbf{r})] - J[\rho(\mathbf{r})] \tag{1.31}$$

Hence $E_{\mathrm{xc}}[\rho(\boldsymbol{r})]$ contains the difference between the kinetic energy of a real system with density $\rho(\boldsymbol{r})$ and the kinetic energy of a non-interacting system of electrons with the same density, as well as all electron–electron interactions not described by the classical Coulombic repulsion.

Kohn and Sham noted that the real system is equivalent to the non-interacting electron system experiencing a modified external potential. The electron density for an interacting system could be obtained from the one-electron eigenvalue equations but where $V_{\mathrm{ext}}(\mathbf{r})$ was replaced by a modified external potential $V_{\mathrm{KS}}(\mathbf{r})$, known as the Kohn-Sham potential, where;

$$V_{\mathrm{KS}}(\mathbf{r}) = V_{\mathrm{ext}}(\mathbf{r}) + \int \frac{\rho(\mathbf{r}')}{|\mathbf{r} - \mathbf{r}'|} d\mathbf{r}' + V_{\mathrm{xc}}(\mathbf{r}) \tag{1.32}$$

Replacing $V_{\mathrm{ext}}(\mathbf{r})$ for $V_{\mathrm{KS}}(\mathbf{r})$ in the one electron Hamiltonian of (1.26);

$$\hat{h}\varphi_i = \left(-\frac{1}{2}\nabla^2 + V_{\mathrm{KS}}(\mathbf{r})\right)\varphi_i = \varepsilon_i \varphi_i \tag{1.33}$$

$$\hat{h}\varphi_i = \left(-\frac{1}{2}\nabla^2 + V_{\mathrm{ext}}(\mathbf{r}) + \int \frac{\rho(\mathbf{r}')}{|\mathbf{r} - \mathbf{r}'|} d\mathbf{r}' + V_{\mathrm{xc}}(\mathbf{r})\right)\varphi_i = \varepsilon_i \varphi_i \tag{1.34}$$

where $V_{\mathrm{xc}}(\mathbf{r})$ is the functional derivative of the $E_{\mathrm{xc}}[\rho(\mathbf{r})]$ with respect to ρ and $\mathbf{r}$;

$$V_{\mathrm{xc}}(\mathbf{r}) = \frac{\delta E_{\mathrm{xc}}[\rho(\mathbf{r})]}{\delta \rho(\mathbf{r})} \tag{1.35}$$

Similar to the way the Fock operator depends on the orbitals, the Kohn-Sham potential depends upon the density through (1.32), therefore the Kohn-Sham equations have to be solved self-consistently. To do this an initial set of one-electron orbitals φ_i are used, from which the initial electron density is obtained. From the initial electron density the initial $V_{\mathrm{KS}}(\mathbf{r})$ can be obtained and is used to find the new orbitals and hence the new density. This process is repeated until the density is self-consistent.

1.2.3 Exchange-Correlation Functionals

In the case of Kohn-Sham DFT, the exact form of the exchange correlation functional would give the true ground state energy (in the limit of the Born-Oppenheimer equation and not taking relativity into account), however, the exact form is not known. Therefore approximations must be made to its form; the approximations made for the functional are generally what distinguishes different

approaches of DFT. Typically exchange-correlation functionals deal with the exchange and correlation separately. In this section some of the most common forms are discussed.

1.2.3.1 LDA Functionals

The local density approximation (LDA) assumes that the electron density varies only slowly, so that the exchange-correlation energy density at a point is the same as that of the uniform electron gas (UEG) with the same electron density. The UEG is a system where the electron density is constant throughout—this is most similar to a metal system, where a "sea" of electrons surrounds the positively charged nuclei. An LDA functional is known as local because the exchange-correlation energy depends only on the local value of the electron density at a point r, having the following form:

$$E_{\mathrm{xc}}^{\mathrm{LDA}}[\rho(\mathbf{r})] = \int \rho(\mathbf{r})\varepsilon_{\mathrm{xc}}^{\mathrm{UEG}}\big(\rho(\mathbf{r})\big)d^3\mathbf{r} \tag{1.36}$$

$\varepsilon_{\mathrm{xc}}^{\mathrm{UEG}}\big(\rho(\mathbf{r})\big)$ is the exchange-correlation energy per particle of an electron gas and is well known from quantum Monte Carlo methods – the $\varepsilon_{\mathrm{xc}}^{\mathrm{UEG}}$ is made up of separate $\varepsilon_{\mathrm{x}}^{\mathrm{UEG}}$ and $\varepsilon_{\mathrm{c}}^{\mathrm{UEG}}$ parts. LDA works well for many solid systems where the electron density varies slowly, however for atoms and molecules where the electron density varies more quickly LDA often gives poor results, e.g. it tends to overestimate binding energies and underestimate bond lengths or lattice parameters.

1.2.3.2 GGA Functionals

For the generalised gradient approximation (GGA), the exchange correlation energy not only depends on the value of the electron density but also on the value of its gradient as well. These functionals are still considered local (or semi-local due to the inclusion of the gradient of the electron density) as they depend only on the local value of the density and its gradient:

$$E_{\mathrm{xc}}^{\mathrm{GGA}}[\rho(\mathbf{r})] = \int \rho(\mathbf{r})\varepsilon_{\mathrm{xc}}^{\mathrm{UEG}}\big(\rho(\mathbf{r})\big)F_{\mathrm{xc}}(\rho(\mathbf{r}), \nabla\rho(\mathbf{r}))d^3\mathbf{r} \tag{1.37}$$

$F_{\mathrm{xc}}(\rho(\mathbf{r}), \nabla\rho(\mathbf{r}))$ is an enhancement factor which depends on the density as well as its gradient and modifies the $\varepsilon_{\mathrm{xc}}^{\mathrm{UEG}}\big(\rho(\mathbf{r})\big)$ term. By incorporating the gradient of the density GGA functionals achieve a significant reduction in the overbinding found with LDA functionals. Unlike for LDA, there is no universal form for GGAs, and the various GGA functionals differ in the definition of $F_{\mathrm{xc}}(\rho(\mathbf{r}), \nabla\rho(\mathbf{r}))$. There are many GGA functionals; some of these contain empirical parameters that have been fitted to data, such as B-LYP, others include no empirical parameters, one of the most popular is the PBE functional[13] which is used for some calculations in Chapter 3. As mentioned the exchange and correlation terms can be treated separately, (1.38) and (1.39) show the form of the exchange and correlation terms for the PBE functional respectively.

$$\varepsilon_{\mathrm{x}}^{\mathrm{PBE}}[\rho(\mathbf{r})] = \varepsilon_{\mathrm{x}}^{\mathrm{UEG}} F(x)$$

$$F(x) = 1 + a - \frac{a}{1 + bx^2} \qquad (1.38)$$

$$x = \frac{|\nabla\rho|}{\rho^{4/3}}$$

where a and b are non-empirical parameters.

$$\varepsilon_{\mathrm{c}}^{\mathrm{PBE}}[\rho(\mathbf{r})] = \varepsilon_{\mathrm{c}}^{\mathrm{UEG}} + H(t)$$

$$H(t) = c f_3^3 \ln\left[1 + dt^2\left(\frac{1 + At^2}{1 + At^2 + A^2t^4}\right)\right]$$

$$A = d\left[\exp\left(-\frac{\varepsilon_{\mathrm{c}}^{\mathrm{LDA}}}{c f_3^3}\right) - 1\right]^{-1} \qquad (1.39)$$

$$f_3(\zeta) = \frac{1}{2}\left[(1+\zeta)^{2/3} + (1-\zeta)^{2/3}\right]$$

$$t = \left[2(3\pi^3)^{1/3} f_3\right]^{-1} x$$

where c and d are also non-empirical parameters and ζ is the relative spin polarization.

LDA and GGA functionals are unable to correctly describe strongly correlated materials, such as actinide dioxides, primarily due to the self-interaction error.

The self-interaction error arises from the form used for the Coulomb repulsion between electrons. In a one-electron system using Hartree-Fock theory the Coulomb repulsion of an electron with itself is cancelled by the exchange term, however this does not occur in DFT. This means that in a one-electron system with DFT the electron incorrectly experiences a Coulomb repulsion from itself. The self-interaction error also occurs in multi-electron systems and causes the delocalisation of orbitals, particularly evident in the spatially localised d and f orbitals. Therefore the use of LDA and GGA functionals will lead to the incorrect electronic structure for actinide dioxide systems. Various methods have been employed in order to obtain the correct electronic structure in DFT calculations of strongly correlated systems, including DFT+*U*[14], SIC-DFT[15] and using hybrid functionals. In this study hybrid functionals have been employed.

1.2.3.3 Hybrid Functionals

As has been mentioned, most exchange-correlation functionals split into terms for the exchange and terms for the correlation separately. Using the adiabatic connection method the exchange-correlation energy can be written as a linear combination of Hartree-Fock exchange and DFT exchange, as well as the DFT correlation energy. Hybrid functionals, therefore, incorporate a fixed proportion of the non-local Hartree-Fock exchange into E_{xc}, with the remaining exchange energy coming from the DFT functional employed, while all of the correlation energy comes from the DFT functional employed. A general expression for hybrid functionals is as follows,

$$E_{\mathrm{xc}} = (1-a)E_{\mathrm{x}}^{\mathrm{DFT}} + aE_{\mathrm{x}}^{\mathrm{HF}} + E_{\mathrm{c}}^{\mathrm{DFT}} \qquad (1.40)$$

The HF exchange energy term calculated within DFT differs from the exchange energy in a pure Hartree-Fock calculation as Kohn-Sham orbitals are used. The constant a determining the proportion of Hartree-Fock exchange must be fixed for each functional. In this study the PBE0[16] functional is used, which has a value of 0.25 for a, and uses the form of the PBE functional for the non-HF exchange and the correlation terms, (1.41).

$$E_{\mathrm{xc}}^{PBE0} = \frac{3}{4}E_{\mathrm{x}}^{\mathrm{PBE}} + \frac{1}{4}E_{\mathrm{x}}^{\mathrm{HF}} + E_{\mathrm{c}}^{\mathrm{PBE}} \quad (1.41)$$

Hybrid functionals incur a greater computational cost due to having to calculate the Hartree-Fock exchange energy; they are particularly expensive when used in periodic DFT calculations and hence are rarely used in such studies.

1.2.4 Basis Sets

As mentioned, Kohn-Sham DFT introduces molecular orbitals to represent the electron density of a system; these molecular orbitals are expanded in a set of known functions, commonly centred on atoms, it is these functions that form a basis set. A complete basis set would require an infinite number of functions and is clearly not practical, instead a finite basis set must be used. Increasing the size of the basis set increases the accuracy of the representation of the electron density, however it also increases the computational cost required so clearly a balance must be made between the two. Not just the number of basis functions but also the type of functions used in a basis set affects the quality of the set. The better the basis functions represent the system being described the smaller a basis set can be used to obtain the same accuracy.

The two most commonly used types of basis functions are Slater Type Orbitals (STO) and Gaussian Type Orbitals (GTO), with the following functional forms:

STO $$\chi_{\zeta,n,l,m}(r,\theta,\varphi) = NY_{l,m}(\theta,\varphi)r^{n-1}e^{-\zeta \mathrm{r}} \quad (1.42)$$

GTO $$\chi_{\zeta,n,l,m}(r,\theta,\varphi) = NY_{l,m}(\theta,\varphi)r^{2n-2-l}e^{-\zeta r^2} \quad (1.43)$$

where N is a normalization constant, $Y_{l,m}$ are spherical harmonic functions dependent on the quantum numbers l, the orbital angular momentum quantum number and m, the magnetic quantum number, r is the distance from the nucleus, n is the principal quantum number, and ζ is the orbital exponent. STOs reach a maximum at zero and decay exponentially with distance from the nucleus, showing the same dependence on distance from the nucleus as the solution to the Schrödinger equation for the hydrogen atom. However; three- and four-centre two-electron integrals are computationally expensive to calculate with STOs.

GTOs have an r^2 dependence in the exponential, hence falling off more rapidly away from the nucleus than the exact solutions for the hydrogen atom. Due to the r^2 dependence in GTOs the derivative is 0 at $r = 0$, unlike STOs, where it has a finite value, again like the solution to the Schrödinger equation for the hydrogen atom. The advantage of GTOs comes in that overlap and other integrals are much easier to calculate, the product of two GTOs on two different centres is another GTO at a third centre intermediate between the original two. This allows four-centre integrals over GTOs to be written as two-centre two-electron integrals. In addition STOs can be approximated by a linear combination of GTOs and although this means that when using GTOs more functions must be used than with STOs, the computational saving more than makes up for this. For these reasons most quantum mechanical calculations using orbitals will use GTOs, as have been used in this study.

As mentioned above, the size of the basis set is important, affecting both the accuracy and the computational cost of the calculation. A minimal basis set requires only enough functions needed for each atom. For hydrogen and helium this means only a 1s function, for the first row elements it means 1s, 2s, and 2p functions, and so on. Increasing the basis set from this we get a double zeta (DZ) basis set, with double the amount of radial functions to the minimal basis set. Hence for the first row elements there are four sets of s functions (two for 1s and two for 2s) and two sets of 2p functions. The basis set can be further increased in a similar manner, giving triple zeta (TZ) and quadruple zeta (QZ) basis sets.

The valence electrons are the most important during bonding, while the core electrons are altered little from the atomic case, so increasing the number of basis functions on the core orbitals increases the accuracy of the calculations very little. We can therefore split our core and valence electrons and only add basis functions to the valence orbitals, giving us split valence basis sets. For the first row elements a split valence DZ basis set would mean one set of 1s functions and two sets of 2s and 2p functions. Split valence DZ basis sets are often simply referred as SV basis sets, while TZ and QZ become TZV and QZV basis sets.

Basis functions of higher angular momentum can be added to the basis set; these are known as polarization functions. This means adding p functions to s valence

orbitals, d to p valence orbitals and so on. The addition of polarization functions increases the flexibility of the representation of the electron density around an atom. The basis sets are commonly labelled as SVP, TZVP and QZVP when including these polarization functions. Some basis sets include polarization functions on all atoms except hydrogen in order to save computational time, they are denoted as *x*V(P), where *x* = S, T, Q etc.

1.2.4.1 Effective Core Potentials (ECPs)

As mentioned above, the core electrons change little in different chemical environments, although the electron-electron repulsion with the valence electrons must be adequately described. ECPs replace the explicit treatment of the core electrons with an effective potential that describes the nucleus and core electrons. In this way only the chemically important valence electrons are treated explicitly, reducing the computational cost of the calculation. ECPs also allow for an efficient treatment of relativistic effects – particularly scalar relativistic effects – to be included, which is more important the further down the periodic table and especially so for actinide atoms.

The decision of which electrons are chemically important and considered outside of the core is debatable in each case, and again a compromise is made between computational saving and accuracy. A smaller core means more accurate results but increased computational cost. ECPs are often referred to as large core, where only electrons in the valence shell are considered outside the core, or small core, where some non-valence shell electrons are also considered outside of the core.

1.2.5 Relativistic Effects

According to the Special Theory of Relativity the mass of a particle, m, increases as the velocity of the particle, v, increases towards the speed of light, c. This is known as the relativistic mass increase; how the mass changes as the velocity increases is given in (1.44).

$$m = m_0 \left(\sqrt{1 - \frac{v^2}{c^2}} \right)^{-1} \quad (1.44)$$

where m_0 is the rest mass of the particle. The radial velocity of a 1s electron is approximately equal to Z, the atomic number of the atom, hence the velocity of a 1s electron increases with the size of the nucleus. For large atoms the velocities of the 1s electrons are significant in relation to the speed of light and therefore there is a significant increase in their masses, leading to a shrinking of the 1s orbital. The stabilization of the 1s orbitals leads to a stabilization of higher s-orbitals, which must be orthogonal to the 1s orbital, together these effects are known as the relativistic orbital contraction. The p-orbitals experience the stabilization to a much lesser degree and stay roughly the same size. A result of the relativistic orbital contraction is that the stabilized s-orbitals screen the nuclear charge more effectively, and this leads to a destabilization of the d- and f-orbitals, known as the indirect orbital expansion.

For small atoms the effects on energies and geometries are minor, and unless calculations need to be performed to very high accuracy relativistic effects can be neglected. As we go down the periodic table, however, including relativity in calculations becomes more important, by the fifth row somewhat crucial, for example the yellow colour of gold is only predicted when relativistic effects are included[17].

The Schrödinger equation is non-relativistic, a fully relativistic calculation is performed with the four-component Dirac equation. The Dirac equation is much more complicated to implement than the SE, therefore other methods are often used to incorporate relativistic effects into calculations: relativistic ECPs (RECPs) or approximate Hamiltonians based on the Dirac equation can be used.

The Schrödinger equation does not include spin and as such it has to be treated *ad hoc*, the Dirac equation, however, naturally leads to spin. A consequence of this is the inclusion of spin-orbit coupling in a fully relativistic quantum chemical calculation. Spin-orbit coupling is due to the interaction between the spin angular momentum of the electron and its orbital angular momentum, which can cause a

splitting of energy levels. The spin-orbit coupling is zero for s orbitals, largest for p orbitals, and then decreases to d and f orbitals. Like the scalar relativistic effects, the spin-orbit coupling increases with atomic number.

The orbital contraction mainly affects the core electrons, so if an RECP is used which describes this properly the impact on the valence orbitals, primarily the indirect expansion, can be accounted for, therefore the scalar relativistic effects can be accounted for with an RECP. RECPs are used to account for relativity in Chapters 3–5 of this thesis.

An alternative to accounting for the scalar relativistic effects with an RECP is to perform an all-electron calculation with a relativistic Hamiltonian. Two popular choices are the Zeroth-Order Approximation (ZORA) and the Douglas-Kroll-Hess (DKH) Hamiltonian. Both of these methods can be carried out with or without spin-orbit coupling; in this thesis DKH calculations have been performed without spin-orbit coupling. The DKH Hamiltonian is used in Chapter 2 of this thesis, where the calculations must be all-electron.

1.2.6 Basis Set Superposition Error

As mentioned above the basis functions – in molecular calculations at least – are generally centred on the nuclei. As the distance between nuclei decreases it is possible for basis functions centred on one nucleus to be able to describe electron density closer to another nucleus. This can occur when calculating binding energies, for example, ligand binding energies, adsorption energies, or complexation energies. If we consider two fragments, A and B, which come together to form a complex, AB, then the complexation energy would be:

$$E_{\text{complexation}} = E(\mathrm{AB}) - E(\mathrm{A}) - E(\mathrm{B}) \tag{1.45}$$

However, as the fragments A and B come closer to form the complex AB the basis functions centred on either A or B overlap with the electron density on the other fragment. Thus the complexation energy is not only due to the interaction between fragments A and B but also due to each fragment using the basis functions centred on the other fragment. This leads to an increase in the complexation energy known as the basis set superposition error (BSSE). The

BSSE can be pronounced when the basis sets are of poor quality or when they are unbalanced, i.e. when there is a larger basis set on one fragment relative to the other.

The BSSE can be estimated with the Counterpoise (CP) correction[18] as the difference between the energy of the fragments with and without the basis functions of the other fragments present:

$$BSSE = E(\mathrm{A})^{\mathrm{AB}} - E(\mathrm{A})^{\mathrm{A}} + E(\mathrm{B})^{\mathrm{AB}} - E(\mathrm{B})^{\mathrm{B}} \qquad (1.46)$$

The superscripts in (1.46) indicate which basis functions are used in each energy calculation, hence $E(\mathrm{A})^{\mathrm{AB}}$ is the energy of fragment A, with the basis functions of both fragment A and fragment B present. The geometries of the fragments A and B in (1.46) are at their positions in the optimized geometry of the complex AB (as opposed to their optimized geometry in isolation, as in (1.45)). The BSSE is then subtracted from the complexation energy to give the counterpoise corrected complexation energy, $E^{\mathrm{CP}}_{\mathrm{complexation}}$:

$$E^{\mathrm{CP}}_{\mathrm{complexation}} = E_{\mathrm{complexation}} - BSSE \qquad (1.47)$$

The inclusion of the BSSE via the CP correction leads to a reduction in the complexation energy. As larger basis sets are used the BSSE should decrease. The BSSE via the CP method is only an estimate, and there are other ways to calculate the BSSE, however the CP method is the most commonly used.

1.2.7 Dispersion

Dispersion can be viewed as the attractive interaction caused by electrons in one region responding to instantaneous charge density fluctuations in another region. Standard exchange-correlation functionals are unable to describe long-range correlation effects and therefore do not describe dispersion forces. This inability in describing dispersion is due to two factors. Firstly the exchange-correlation functionals only consider local properties when calculating the exchange-correlation energy. Secondly the electrons are considered to interact with the total electron density in a mean field way, instead of the instantaneous electron positions.

The simplest way to include the long range effects of dispersion into DFT calculations is to include an additional energy term which accounts for the long range $-1/r^6$ attraction:

$$E_{\mathrm{Tot}} = E_{\mathrm{DFT}} + E_{\mathrm{Disp}} \tag{1.48}$$

Where E_{DFT} is the total energy calculated from DFT with a particular exchange-correlation functional and E_{Disp} is the dispersion energy given by:

$$E_{\mathrm{Disp}} = -\sum_{\mathrm{A,B}} C_6^{\mathrm{AB}}/r_{\mathrm{AB}}^6 \tag{1.49}$$

Where C_6^{AB} is the dispersion coefficient depending on atoms A and B, and r_{AB} is the interatomic distance between A and B. As the dispersion energy is the sum of the dispersion interactions between atoms A and B it is considered pairwise additive.

The C_6/r^6 corrections diverge at short distances and therefore must be damped; the dispersion energy becomes:

$$E_{\mathrm{Disp}} = -\sum_{\mathrm{A,B}} f(r_{\mathrm{AB}}, \mathrm{A}, \mathrm{B}) C_6^{\mathrm{AB}}/r_{\mathrm{AB}}^6 \tag{1.50}$$

Where $f(r_{\mathrm{AB}}, \mathrm{A}, \mathrm{B})$is a damping function that is equal to one at large values of r and decreases to zero or a constant at small values. As the binding produced in a DFT calculation is affected by the exchange-correlation functional used, the damping function must be adjusted for each functional.

This method is used in the DFT-D[19] and DFT-D2[20] dispersion corrections of Grimme. An extension to this is used in the DFT-D3[21] method, where the C_6 coefficient changes depending on the environment the atom is in. The coefficient decreases as the number of neighbours an atom has increases, with more neighbours the atom is squeezed and its electron density is less polarizable. The number of neighbours an atom has can be easily obtained and so the computational cost of this step is small.

1.3 Computational Methods

1.3.1 The Periodic Electrostatic Embedded Cluster Method

The periodic electrostatic embedded cluster method (PEECM) was developed by Burow *et al.*[22] as a computationally cheap way to treat point defects at low concentrations in ionic systems.

Periodic calculations, the method most commonly used for studying water adsorption on AnO_2, involves describing the system by a unit cell with boundary conditions applied. Defects are therefore repeated in each unit cell and unless large enough unit cells are used the defects will experience interactions with their mirror image neighbours. Using larger unit cells can reduce the interactions the defects experience, however this greatly increases the computational time required. Conversely, embedded cluster methods, including the PEECM, treat a finite cluster of atoms in the system quantum mechanically, while the interactions of the rest of the system with the finite cluster are approximated to some extent. In the PEECM the rest of the system is approximated by point charges in order to reproduce the electrostatic interactions of the cluster with the rest of the ionic system.

The PEECM approach generally splits the system into three regions (Figure 1.1 gives a specific example of the PEECM with the AnO_2 (111) surface): an inner explicit cluster region, which is treated quantum mechanically; an outer embedding region, consisting of point charges; and an intermediate embedding region, consisting of negative point charges and pseudopotentials (PPs). The inner cluster region is then treated as a molecular quantum chemistry calculation and both Hartree-Fock and DFT type methods can be used. The intermediate region is in place to avoid positive point charges over-polarizing the electron density of the inner region. The outer region then reproduces the Madelung potential – due to long range electrostatic interactions – in the inner cluster region.

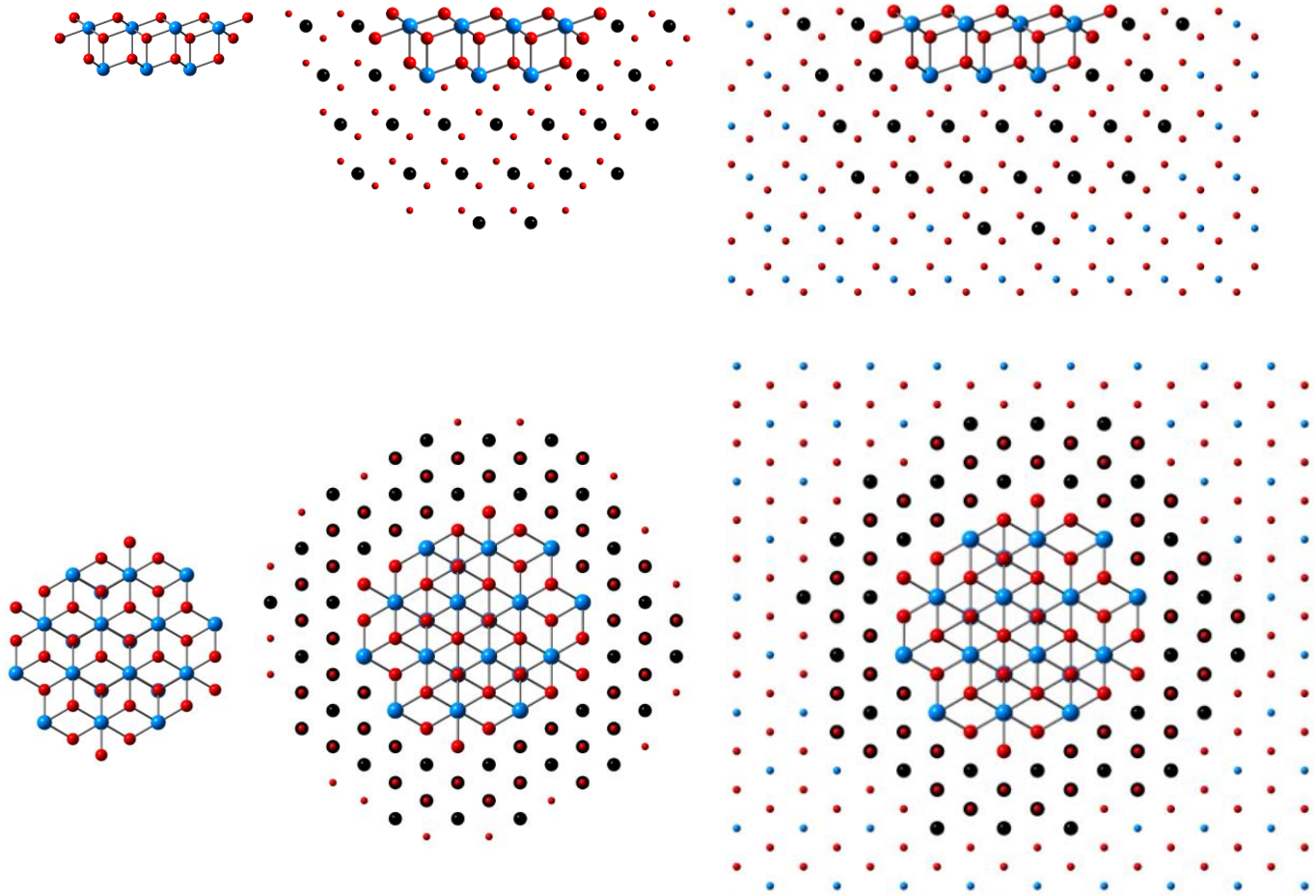

Figure 1.1 Embedding of an AnO_2 (111) surface cluster in the PEECM regime. The quantum mechanical cluster of the inner region (left) embedded in the intermediate region (centre) and outer region (right). Large blue spheres represent explicit actinide ions, large red explicit oxygen, large black, PPs of the intermediate region, small blue actinide point charges, and small red oxygen point charges. Top row shows side view of the surface, bottom row shows view down onto surface. Outer region truncated.

The periodic fast multipole method[23–25] (based on the multipole expansion) is used as a computationally cheap way to reproduce the Madelung potential due to a periodic array of point charges (the outer embedding region).

The PEECM was designed for ionic systems; there should be no covalent bonds between the inner cluster and the intermediate/outer regions as this would lead to dangling bonds. Although in Chapter 2 I investigate systems with covalent bonding (e.g. $U(Se_2PPh_2)_4$), there are no covalent bonds between the cluster and embedding regions.

The PEECM is able to treat periodic point charge arrays of one-, two- and three-dimensions, meaning that surfaces can be modelled as well as bulk systems. For surface calculations the point charge region is a two-dimensional slab with a finite thickness.

1.3.2 Quantum Theory of Atoms in Molecules

The Quantum Theory of Atoms in Molecules (QTAIM) was developed by Bader[9] as a way of using the topology of the electron density of a system to investigate its bonding properties and to partition the space in the system to individual atoms to investigate their properties. As the electron density can be measured experimentally – as well as being produced in calculations – QTAIM provides an important link between experimental and theoretical results.

The gradient of the electron density, $\nabla\rho(\mathbf{r})$, is used to determine critical points in the electron density distribution, where $\nabla\rho(\mathbf{r}) = 0$ there is a critical point in the electron density (a maximum, minimum or saddle point). The nature of the critical points can be determined by the curvature of the density at these points (by examining the sign of the curvature along three principle axes). Maxima occur at nuclei, known as nuclear critical points (NCPs); saddle points occur in bonds, bond critical points (BCPs), and in rings, ring critical points (RCPs); and minima occur in cages, cage critical points (CCPs).

The gradient of the electron density at a point in space gives a vector pointing in the direction of the greatest increase in $\rho(\mathbf{r})$ (hence it being zero at critical points)

and the magnitude of the resulting vector is equal to the rate of the increase in that direction.

Atoms which are bonded to each other, whether it be by closed-shell or open-shell interactions, are joined by a single line of locally maximum density (like a ridge between two peaks), known as the bond path, with a BCP along this path. The BCP lies along the bond path at the point where the electron density is a minimum, i.e. there are two gradient trajectories that start at the BCP, follow the two lines of greatest increase in $\rho(\mathbf{r})$ and end at the two nuclei of that bond. The BCP also lies at the point where the zero flux surface of the gradient vector field intersects the bond path.

At the BCP the values of $p(\mathbf{r})$, $\nabla^2\rho(\mathbf{r})$ (the Laplacian of the electron density), and H (the energy density) can be used to characterise the nature of the bond between two atoms, e.g. give insight into the covalency of a bond. This will be discussed further in Chapter 2.

Atoms are partitioned by surfaces where the gradient vectors do not cross the surface (where there is zero flux in the gradient vector field across the surface). The atoms are then bounded by these surfaces into atomic basins, Ω. This is where the name Atoms in Molecules comes from, as it allows a molecular space to be split up into certain atoms. Properties, such as the electron density, can then be integrated over the atomic basins, to give certain insight into the constituent atoms, such as their partial charges.

1.3.3 COSMO

The Conductor-like Screening Model (COSMO)[26] is a model which approximates the effects of a solvent on a molecular solute. It is a polarizable continuum model where the solute is inside a cavity. Outside the cavity the solvent is represented by a dielectric continuum of permittivity, ε. Although COSMO is often used to model solvent molecules surrounding a molecular solute, it can also be used as a very crude and simple way to model the electrostatic potential of a crystal around a system, as it is used in Chapter 2 of this thesis.

1.3.4 Population Analysis

The atomic charge (the sum of the nuclear and electronic charge on an atom) is not a physical observable and there is no unique way to define it. However, the idea of an atom's partial charge is a useful concept for chemists when considering bonding and chemical behaviour. Furthermore it can be used to approximate the electrostatic interactions of particular atoms in a system, as I will use with the PEECM.

To calculate a partial charge we need to divide the electron density in same way and assign these parts to particular atoms in the system. The partial charge, q_A, is then calculated as:

$$q_A = Z_A - \int \rho_A(\mathbf{r}) d\mathbf{r} \tag{1.51}$$

Where Z_A is the nuclear charge of atom A and ρ_A the density assigned to atom A. The way population analysis methods differ is the way they assign portions of the density to a particular atom. Generally there are two main methods to do this: partitioning the wavefunction based on the orbitals to particular atoms, or by partitioning the space in a molecule to particular atoms.

Mulliken population analysis is one of the oldest and simplest ways to calculate partial charges on atoms, and for those reasons it is one of the most widely used methods. The electrons are assigned to an atom based on the contribution of an atom's atomic orbitals to the molecular orbitals. We first define an overlap population, O_{kl}, that is the population shared by two atomic orbitals, χ_k and χ_l, across all molecular orbitals, ϕ_i.

$$O_{kl} = \sum_i c_{i,k} c_{i,l} S_{kl} \tag{1.52}$$

where S_{kl} are components of the overlap matrix:

$$S_{kl} = \int \chi_k \chi_l \mathrm{d}\boldsymbol{\tau} \tag{1.53}$$

If we sum the overlap population terms over all basis functions χ_l, we obtain the gross population for χ_k, P_k:

$$P_k = \sum_l O_{kl} \tag{1.54}$$

By summing the gross population for all basis functions centred on atom A, we obtain the gross atomic population, P_A.

$$P_A = \sum_{k \in \mathrm{A}} P_k \tag{1.55}$$

The partial charge for atom A is then simply:

$$q_A = Z_A - P_A \tag{1.56}$$

Certain problems can arise when performing Mulliken population analysis. Firstly, the atomic charges depend on the basis set used, a large basis set with diffuse functions can assign electron density to an atom far away. This also means that larger basis sets can often give what we might consider poorer results for the atomic charges. Mulliken charges, therefore, should not be compared between calculations using different basis sets. Secondly, we can also obtain values greater than 2 for the gross population of a particular basis function, or even negative values.

The molecular orbitals used to reproduce the charge distribution of the wavefunction are not a unique solution, another set of molecular orbitals – which also reproduces the charge distribution of the wavefunction – could also be used. In natural population analysis[27] a new set of orbitals is defined which is orthonormal.

Natural orbitals are derived by diagonalizing the reduced first-order density matrix. Pre-natural atomic orbitals (PNAOs) for atom A are then defined as the orbitals which diagonalize a block of the matrix corresponding to orbitals only on atom A. These PNAOs are then orthogonalized by a procedure which aims to have minimal change in the strongly occupied PNAOs, while the weakly occupied (or Rydberg) PNAOs are allowed to change more greatly in the orthoganilization

procedure. The occupations of the NAOs are guaranteed to be between 0 and 2, unlike in Mulliken, and so no negative populations are obtained. The occupations also converge as the basis set size is increased. The NAOs can still extend quite far from the atom they belong to, and hence, like Mulliken population analysis, can still account for electron density that is nearer to another atom centre.

Both Mulliken and natural population analysis used the first method described, where the electron density is assigned to particular atoms based on the orbitals used. The second way involves partitioning the space in our system, deciding which parts of space belong to which atom, creating boundaries between the atoms. The electron density can then be integrated over an atom's volume to give the population for that particular atom. As mentioned in Section 1.3.2, QTAIM provides a way to separate a system into atomic volumes based on the zero flux surface of the electron density gradient. Once the system has been separated into atomic volumes it is simple to integrate the electron density over this volume and calculate the atomic charges. Relative to the other methods, however, QTAIM charges are computationally expensive.

1.4 **Computational Codes**

1.4.1 Turbomole

Turbomole is a quantum chemistry code, developed by Ahlrichs at the University of Karlsruhe in 1987, it is now developed by Turbomole GmbH (Ltd.). The main focus of the program is to provide a fast and stable code for molecular calculations, an overview of its main features can be found at its website and in a recent review of the program.[28] Solvation or electrostatic environmental effects can be accounted for through COSMO, the PEECM or, more recently, periodic DFT – although periodic calculations cannot be implemented with hybrid functionals. The code uses Gaussian basis sets and has a range of LDA, GGA, meta-GGA, hybrid, and double hybrid exchange-correlation functionals. The code can be parallelised, although for the calculations in this study it has been noted that not much improvement is made above 30 cores. The code has been used in this thesis for electronic structure calculations, geometry optimizations, population analysis (through Mulliken and NPA).

1.4.2 AIMAll

The AIMAll program performs QTAIM analysis of molecular systems using the molecular wavefunction. AIMAll version 14[29] was used in the QTAIM analysis in Chapter 2 of this thesis.

2 The Effect of the Crystal Environment in the Topology of the Electron Density of $UO_2Cl_4Cs_2$, $U(Se_2PPh_2)_4$ and $Np(Se_2PPh_2)_4$

2.1 Introduction

It can be difficult to make connections between results obtained from experiment and those from quantum chemical calculations. Certain properties calculated quantum chemically, such as partial atomic charges and bond orders, are not directly observable experimentally and, while experimental techniques are available for determining atomic orbital mixing (e.g. ligand K-edge x-ray Absorption Spectroscopy[30,31] and Photoelectron Spectroscopy[32]) there is no unique computational way to express molecular orbital structure, with conclusions drawn from analysis of canonical orbitals often being rather different from those obtained from localised orbital descriptions.

The electron density, however, is a property that is both observable experimentally and can be calculated quantum mechanically – being readily available from both wavefunction and DFT calculations. The Quantum Theory of Atoms in Molecules (QTAIM),[9] which focuses on the topology of the electron density, therefore, provides a link between experiment and theory.

Comparisons between results obtained experimentally and theoretically and then analysed with QTAIM are well established for many organic and inorganic systems. However this comparison has rarely been made for systems involving the actinides. This is due to both the difficulty in obtaining high quality experimental electron densities from radioactive systems with heavy elements, and with QTAIM only recently being used to study actinide containing systems. QTAIM has been used on molecular actinide systems to study both covalency[33–45] and bond strength,[46–48] although the effect that the crystal field has on the electron density topology has not been investigated.

$Th(S_2PMe_2)_4$[49] and $Cs_2UO_2Cl_4$[50,51] are the only actinide systems to have been studied experimentally using QTAIM. The bonding in actinide complexes, such as these, is of real interest, particularly in the area of nuclear power generation

and nuclear waste management. For example, understanding the bonding between ligands and the metal centre in lanthanide and actinide systems can help in the design of species which are able to separate lanthanide and actinide ions, which is required in the nuclear cycle.

Zhurov *et al.* obtained the electron density of $Cs_2UO_2Cl_4$ from accurate x-ray diffraction experiments and subsequently performed QTAIM analysis. Vallet *et al.* then carried out a quantum chemical study of $[UO_2Cl_4]^{2-}$ using DFT and probed the electron density topology using QTAIM.[52] The electron density, ρ, and its Laplacian, $\nabla^2\rho$, at the bond critical point of the U-Cl bonds were found to be in good agreement with experiment. However, for the U-O bond they differ by 0.06 a.u. (24%) and 0.33 a.u. (51%) respectively. As the quantum chemical electron density was obtained from calculation of $[UO_2Cl_4]^{2-}$ in the gas phase, it was suggested that the differences could be related to the long-range influence of the crystal field.[52] I wanted to test this possibility by investigating the effect of the long range interactions on QTAIM parameters in 5f systems, and to see whether there is an improvement in the agreement between theory and experiment if these interactions are better represented.

To check that the effects found are not specific to the $Cs_2UO_2Cl_4$ system, I also investigate the $U(Se_2PPh_2)_4$ and $Np(Se_2PPh_2)_4$ systems, which have been recently studied[38] by QTAIM in the gas phase. The $U(Se_2PPh_2)_4$ and $Np(Se_2PPh_2)_4$ systems are examples of actinide coordination complexes containing soft ligands, these systems are of interest in terms of selective speciation, and the possibility of separating certain lanthanide and actinide ions in the nuclear fuel cycle.[38] Soft donor ligands have shown an affinity for bonding to An^{3+} ions, over lanthanide, Ln^{3+} ions, which has been rationalised in terms of covalent interactions in these systems.

To test the environmental effects I perform calculations in the gas phase, in a polarizable continuum with COSMO and embedded in point charges with the PEECM.

The PEECM acts as an intermediate between gas-phase molecular calculations, which have been used in studying actinide materials with QTAIM as described

above, and periodic DFT calculations. Periodic DFT has been used to study QTAIM in solid-state systems, and hence allows for a comparison with experiment, however, one of the most used codes for this purpose, CRYSTAL[53], does not implement QTAIM analysis with basis sets containing f-functions. PEECM therefore allows us to easily perform QTAIM analysis on f-element systems, while including long-range electrostatic effects.

2.1.1 QTAIM on experimentally derived electron densities

As has been stated, the electron density can be measured experimentally by diffraction experiments, often using x-rays. However, the charge density measured must be refined, as the charge density is a thermally averaged electron density – due to the vibrational motion of nuclei, even at low temperature – so the atomic positions must initially be defined. Then a model must be applied to the measured density to describe the charge distribution analytically so that the QTAIM can then be applied to it.

Most experimental studies adopt the Hansen-Coppens model[54], whereby the obtained electron density is projected on to atom-centred terms with non-spherical distributions. The electron density in a unit cell is initially split up into atomic contributions:

$$\rho_{unit\ cell}(\mathbf{r}) = \sum_{A} \rho_A(\mathbf{r} - \mathbf{r}_A) \tag{2.1}$$

where A counts over the nuclei in the unit cell, and the atomic contributions, ρ_A, are expanded as

$$\rho_A(\mathbf{r}) = P_{A,core}\rho_{A,core} + P_{A,valence}\kappa_A^3\rho_{A,valence}(\kappa_A\mathbf{r}) + \sum_{l=0,l_{max}} \sum_{m=0,l} P_{A,lm\pm} y_{lm\pm}(\mathbf{r}/r)\kappa'^3_{A,lm\pm} R_{A,lm\pm}(\kappa'_{A,lm\pm}\mathbf{r}) \tag{2.2}$$

where ρ are spherically averaged density functions for core and valence electrons calculated from free-atom Hartree-Fock wavefunctions represented with Slater functions. The P terms are population coefficients, κ are radial scaling factors, $R(\mathbf{r})$ are radial density functions (usually also Slater-type functions), and

$y_{lm\pm}(\mathbf{r}/r)$ are spherical harmonics. Hence $P_{A,core}\rho_{A,core}$ describes the core function of atom A with a fixed spherical density distribution, the populations of the core functions can be refined, although often they are fixed. The second term in (2.2) is the spherical valence function, which is allowed to expand or relax through the radial parameter κ. The population parameter in the second term can also be refined. The deformation term, the third term in (2.2), is again refinable through the radial and population parameters, and has a non-spherical distribution around the atom. The terms are refined to give an electron density which fits well to the measured density, this is usually done subject to certain constraints, such as maintaining charge neutrality of the system.

However, there are certain limitations to the model that have been noted. Firstly, the multipole refinement cannot account for two-centre electron density. Unlike molecular orbitals, which are formed from a combination of atom-centred functions, in the Hansen-Coppens model the functions are purely atom-centred, this affects their ability to describe the bonding region of the electron density. Secondly, the angular functions are truncated at a certain multipole level, for f-block elements it has been suggested that multipoles up to a hexacontatetrapole are included, [55] although this is not always done due to lack of data. For example in the study of $CsUO_2Cl_4$,[50,51] only multipoles up to hexadecapoles were included, as the program used for the multipole refinement, XD2006,[56] only includes multipoles up to this level.

2.1.2 Comparisons of QTAIM on experimentally derived and computationally derived electron densities

I described in the introduction the discrepancies between experiment and theory found in the U-O bond in the $Cs_2UO_2Cl_4$ system, aside from actinide systems QTAIM parameters have been compared between experimentally and computationally derived electron density on organic molecular crystals,[57–61] and inorganic systems.[62,63] The studies examining organic molecular crystals found good agreement between values for ρ and $\nabla^2\rho$ at the bond critical points, except for the values of $\nabla^2\rho$ in the polar C=O and N-H bonds. This discrepancy was attributed to the deficiency of the multipole model in describing polar covalent bonds, due to the inflexibility of the model in describing the bonding region. The

discrepancy in the values of $\nabla^2\rho$ was also noted in a $CoSb_3$ study[62] and again attributed to the multipole refinement model.

Other studies have highlighted that $\nabla^2\rho$ in polar bonds can be affected by the type of calculation (HF/DFT/MP2), or the basis set used. However, the range of theoretical values of $\nabla^2\rho$ beyond the HF level is small and does not include the experimental results, and hence cannot account for the difference found between experiment and theory.[61,64]

The theoretical density can also be refined with the multipole model,[58,62] the calculated density is projected onto atom-centred terms, as with an experimental density. This refinement has led to a better agreement between experiment and theory, reinforcing the conclusion that the discrepancy between theory and experiment is due to a deficiency in the multipole model.

In regards to the effects of the environment, Götz *et al.* investigated the effect of the crystal field on the topology of the electron density of methyl lithium, they found the effects to be fairly modest.[65] The study analysed calculations performed in the gas phase, in a polarizable continuum, with PEECM and with periodic boundary conditions; ρ and $\nabla^2\rho$ did not vary significantly between the methods, although no comparison was made with experiment. Other studies on organic molecules also found only small differences between molecular and periodic boundary condition DFT calculations.[57,58]

It should also be mentioned that Vallet *et al.* have previously studied the effect of environment on the electronic spectrum of the uranyl dication (UO_2^{2+}) in $Cs_2UO_2Cl_4$.[66] The most significant environmental effects were found to be due to the equatorial chloride ligands, with only small contributions from the crystal environment.

2.2 Computational Details

All quantum chemical calculations were performed using density functional theory (DFT) as implemented in the TURBOMOLE 6.5 program.[67] As the B3LYP exchange-correlation functional was used in the previous theoretical study[52] of $[UO_2Cl_4]^{2-}$ it has also been employed in the present calculations. The functional

dependence of the QTAIM parameters was probed with a range of exchange-correlation functionals: B3LYP,[68] LDA (VWN),[69] PBE,[13] PBE0,[16] TPSS,[70] and TPSSH[71]. The self-consistent field convergence criterion was set to $1x10^{-6}$.

The def-TZVPP basis sets contained in the TURBOMOLE library were used for all O, Se, P, C and H atoms[72], while the SARC-DKH basis sets were used for U[73], Np[73] and Cs (taken from the ORCA[74] basis set library).

Experimental crystal structures for $Cs_2UO_2Cl_4$,[50] $U(Se_2PPh_2)_4$,[38] and $Np(Se_2PPh_2)_4$[38] were used to provide the atomic positions, as well as the positions of the point charges in the embedding regions for the PEECM.

Wavefunction files were analysed with AIMAll version 14.[29]

COSMO calculations were performed using the TURBOMOLE 6.5 default parameters, i.e. a relative permittivity of $\varepsilon_r = \infty$ and molecular cavities constructed of spheres of radius 2.223 Å for U, Np and Cs, 1.720 Å for O, 2.050 Å for Cl, 2.200 Å for Se, 2.106 Å for P, 2.000 Å for C and 1.300 Å for H.

2.2.1 PEECM

In order to incorporate long range crystal field effects, calculations were performed using the PEECM[22] as implemented in TURBOMOLE 6.5. For these calculations I have not included an intermediate region as the wfn files required for QTAIM analysis must be generated using all-electron basis sets. Hence in order to probe, and if necessary mitigate, overpolarisation of the QM electron density, point charges in the embedding region have been assigned either formal or natural charges. The formal charges for $Cs_2UO_2Cl_4$ are +1, +6, -2, and -1 a.u. for Cs, U, O, and Cl respectively. The natural charges used for the $[UO_2Cl_4]^{2-}$, $Cs_2UO_2Cl_4$, and $(Cs_2UO_2Cl_4)_7$ calculations were obtained from the natural charges of the central $Cs_2UO_2Cl_4$ unit in a series of iterative $(Cs_2UO_2Cl_4)_7$ calculations. The iterative $(Cs_2UO_2Cl_4)_7$ calculations involved embedding the $(Cs_2UO_2Cl_4)_7$ system in an infinite array of formal charges within the PEECM framework, then taking the natural charges obtained on the central $Cs_2UO_2Cl_4$ unit to redefine the charges in the embedding region. The process was repeated until the natural charges were converged to 0.01 a.u. The natural charges for the

central $Cs_2UO_2Cl_4$ unit and hence used for the embedding are +0.96, +1.20, -0.68, and -0.44 a.u. for Cs, U, O, and Cl respectively. The formal charges for $U(Se_2PPh_2)_4$ and $Np(Se_2PPh_2)_4$ are +4, -1, +1, 0, and 0 a.u. on U, Se, P, C, and H respectively. The natural charges used for the two systems were again obtained from an iterative process. Two sets of natural charges were obtained for the C atoms, one for those in the phenyl ring which are bonded to P atoms and another for all the other C atoms in the phenyl ring. The natural charges for $U(Se_2PPh_2)_4$ and so used for the embedding are -0.68, -0.23, 1.09, -0.16, and 0.19 a.u. on U, Se, P, C, and H respectively, C atoms bonded to P have a natural charge of -0.38 a.u. The natural charges for $Np(Se_2PPh_2)_4$ and so used for the embedding are -0.60, -0.20, +1.07, -0.16, and 0.18 a.u. on Np, Se, P, C, and H respectively, C atoms bonded to P have a natural charge of -0.36 a.u.

2.3 **Results**

2.3.1 $Cs_2UO_2Cl_4$

As noted in the Introduction, Vallet *et al.* studied $[UO_2Cl_4]^{2-}$ quantum chemically;[52] here I calculate $[UO_2Cl_4]^{2-}$ as well as $Cs_2UO_2Cl_4$ and a cluster of seven formula units $(Cs_2UO_2Cl_4)_7$ in which the central $[UO_2Cl_4]^{2-}$ anion is surrounded by the next nearest six $[UO_2Cl_4]^{2-}$ units, along with the nearest 14 Cs atoms to make the cluster neutral (Figure 2.1). These three systems have been considered in the gas phase, in a polarizable continuum solvent model with COSMO and embedded in point charges with the PEECM. Both natural charges, obtained from an iterative natural population analysis, and formal charges have been used to define the values of the point charges in the PEECM. The electron densities obtained from these calculations have been analysed using the QTAIM, and the results for the U-O and U-Cl bonds are shown in Table 2.1 and Table 2.2 respectively. No data is given for the $(Cs_2UO_2Cl_4)_7$ with the PEECM approach using formal charges due to convergence issues, however the effect of the charges on this system should, arguably, be less significant than the $Cs_2UO_2Cl_4$ system, as the central unit is surrounded by six quantum mechanically described $Cs_2UO_2Cl_4$ units in $(Cs_2UO_2Cl_4)_7$.

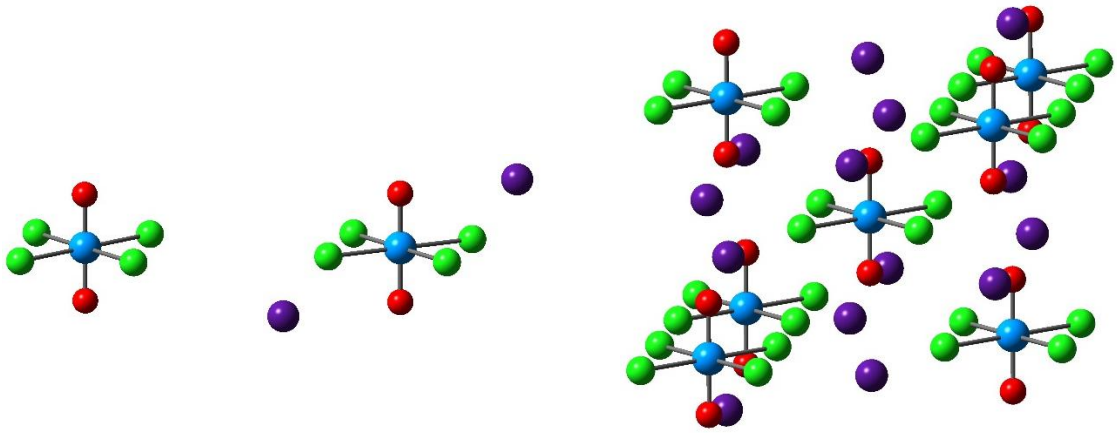

Figure 2.1 Ball and stick images of $[UO_2Cl_4]^{2-}$ (left), $Cs_2UO_2Cl_4$ (centre) and $(Cs_2UO_2Cl_4)_7$ (right). Chlorine atoms are shown in green, caesium atoms in purple, oxygen atoms in red and uranium atoms in blue. Atomic positions are taken from experiment[50].

As mentioned in Section 1.3.2, the QTAIM states that there is a bond critical point (BCP) between every two atoms bonded to each other, with the BCP located at the minimum in the electron density along the bond path, the line of maximum electron density between the two atoms.[9] The values of ρ, $\nabla^2\rho$, and the energy density, H, at the BCP can be used in analysing the nature of the bond. A value of ρ at the BCP (ρ_b) greater than 0.2 a.u. is a sign of a covalent interaction, whereas values less than 0.1 a.u. indicate a closed shell interaction such as ionic, hydrogen or Van der Waals bonding. A positive $\nabla^2\rho_b$ value means there is a depletion of charge at the BCP while a negative value means there is a local charge concentration and indicates a covalent interaction. H_b is negative for interactions with sharing of electrons, with its magnitude indicating the covalency of the interaction.[75] A bond is cylindrically symmetric when the bond ellipticity, ε, is 0, such as in single and triple bonds, with higher values otherwise. The delocalisation index, DI, between two bonded atoms gives an indication of the bond order between them.

In both this and previous studies the values of ρ_b for the U-O bonds are all greater than 0.2 a.u. and the relatively large, negative H_b support a strongly covalent description (Table 1). The values of ρ_b are similar to those found for M≡O (M = Cr, Mo and W) triple bonds.[63] The values of ε so close to zero suggest a triple bond for U-O, in keeping with a $\sigma+2\pi$ description. The strongly polar nature of the U–O bond accounts for the *DI* values (c. 1.9) being significantly lower than the formal value of 3 expected for a triple bond. The experimental papers suggest

that the U-Cl bond can be described as partially covalent[50,51]; however, as also noted by Vallet *et al.*[52], the small absolute values of H_b and ρ_b indicate a largely ionic interaction (Table 2).

There are small differences of approximately 0.01 a.u. and 0.03 a.u in ρ_b and $\nabla^2\rho_b$ for both bonds between our results and those of Vallet *et al.* These are likely to arise from the difference in geometry; whereas in the previous study the $[UO_2Cl_4]^{2-}$ unit was optimized, I have kept the geometry fixed at the experimentally-determined structure.

The results in Table 2.1 and Table 2.2 show that whether the clusters are in the gas-phase, a polarizable continuum solvent model or embedded in point charges has little effect on the topology of the electron density. For both the U-O and the U-Cl bonds in $[UO_2Cl_4]^{2-}$ the values of ρ_b, $\nabla^2\rho_b$, and H_b differ by less than 0.01 a.u. in the different environments. Nor do the QTAIM data change greatly between the different systems; for the gas phase calculation the values of ρ_b, $\nabla^2\rho_b$, and H_b differ by less than 0.01 a.u. between $[UO_2Cl_4]^{2-}$, $Cs_2UO_2Cl_4$ and $(Cs_2UO_2Cl_4)_7$.

		ρ_b (a.u.)	%	$\nabla^2\rho_b$ (a.u.)	%	H_b (a.u.)	%	ε	%	DI	%
$[UO_2Cl_4]^{2-}$	Gas phase	0.303		0.345		-0.272		0.002		1.881	
	COSMO	0.303	0.0	0.344	-0.5	-0.272	0.0	0.002	31.6	1.871	-0.5
	PEECM Natural	0.302	-0.2	0.350	1.2	-0.272	-0.3	0.005	189.2	1.882	0.0
	PEECM Formal	0.302	-0.2	0.350	1.3	-0.271	-0.3	0.003	39.4	1.879	-0.1
$Cs_2UO_2Cl_4$	Gas phase	0.303		0.343		-0.273		0.004		1.882	
	COSMO	0.303	-0.1	0.343	0.0	-0.273	-0.2	0.000	-92.1	1.874	-0.4
	PEECM Natural	0.302	-0.3	0.349	1.9	-0.272	-0.5	0.006	47.3	1.880	-0.1
	PEECM Formal	0.302	-0.4	0.350	2.0	-0.271	-0.6	0.003	-30.6	1.875	-0.4
$(Cs_2UO_2Cl_4)_7$	Gas phase	0.303		0.347		-0.273		0.008		1.877	
	COSMO	0.303	0.1	0.345	-0.5	-0.273	0.1	0.006	-22.3	1.877	0.0
	PEECM Natural	0.303	0.0	0.346	-0.3	-0.273	0.0	0.006	-28.2	1.870	-0.4
	PEECM Formal	-	-	-	-	-	-	-	-	-	-
	Experiment[51]	0.25		0.65	-	-0.23		-		-	
	Previous DFT[52]	0.31		0.32	-	-0.27		-		1.92	

Table 2.1 Bond critical point values of the electron density, ρ_b, Laplacian of the electron density, $\nabla^2\rho_b$, energy density, H_b, and ellipticity, ε, as well as delocalisation index, DI, for the U-O bonds in $[UO_2Cl_4]^{2-}$, $Cs_2UO_2Cl_4$ and the central $[UO_2Cl_4]^{2-}$ unit in $(Cs_2UO_2Cl_4)_7$. Each system is calculated in the gas phase, with a polarizable continuum solvent model *via* COSMO and with the PEECM with natural and formal charges in the embedding region. ρ_b, $\nabla^2\rho_b$, and H_b are in atomic units. Percentage differences from the gas phase data are given in the columns to the right of each metric.

		ρ_b (a.u.)	%	$\nabla^2\rho_b$ (a.u.)	%	H_b (a.u.)	%	ε	%	DI	%
$[UO_2Cl_4]^{2-}$	Gas phase	0.061		0.146		-0.011		0.054		0.571	
	COSMO	0.062	0.6	0.145	-0.6	-0.011	1.7	0.055	2.5	0.580	1.6
	PEECM Natural	0.062	0.5	0.145	-0.3	-0.011	1.4	0.058	7.7	0.574	0.5
	PEECM Formal	0.062	0.7	0.145	-0.5	-0.011	2.2	0.057	5.5	0.577	1.0
$Cs_2UO_2Cl_4$	Gas phase	0.062		0.146		-0.011		0.055		0.574	
	COSMO	0.062	0.3	0.145	-0.3	-0.011	0.9	0.055	-1.0	0.578	0.8
	PEECM Natural	0.062	0.1	0.145	-0.3	-0.011	0.6	0.056	1.4	0.573	-0.1
	PEECM Formal	0.062	0.5	0.145	-0.7	-0.011	1.7	0.053	-3.3	0.575	0.3
$(Cs_2UO_2Cl_4)_7$	Gas phase	0.061		0.147		-0.011		0.058		0.556	
	COSMO	0.062	0.1	0.146	-0.1	-0.011	0.4	0.056	-2.7	0.558	0.4
	PEECM Natural	0.062	0.3	0.146	-0.3	-0.011	1.0	0.055	-5.4	0.562	1.1
	PEECM Formal	-	-	-	-	-	-	-	-	-	-
	Expt[51]	0.07		0.14		-0.03		-		-	
	Prev DFT[52]	0.05		0.12		-0.01		-		0.53	

Table 2.2 Bond critical point values of the electron density, ρ_b, Laplacian of the electron density, $\nabla^2\rho_b$, energy density, H_b, and ellipticity, ε, as well as delocalisation index, DI, for the U-Cl bonds in $[UO_2Cl_4]^{2-}$, $Cs_2UO_2Cl_4$ and the central $[UO_2Cl_4]^{2-}$ unit in $(Cs_2UO_2Cl_4)_7$. Each system is calculated in the gas phase, with a polarizable continuum solvent model *via* COSMO and with the PEECM with natural and formal charges in the embedding region. ρ_b, $\nabla^2\rho_b$, and H_b are in atomic units. Percentage differences from the gas phase data are given in the columns to the right of each metric.

Götz *et al*. who, as noted in the Introduction, performed a similar theoretical study comparing QTAIM values for methyl lithium in different environments but with the same experimental geometry, saw changes of up to 10.8% and 3.3% in the ρ_b of Li-C and C-H bonds respectively[65] between the gas phase and embedding in point charges *via* the PEECM. These changes are larger than those found here for the U-O and U-Cl bonds which change by less than 1% between the polarizable continuum solvent model and the PEECM. The differences found in $\nabla^2\rho_b$ for methyl lithium were up to 1.2% and 6.7% for the Li-C and C-H bonds respectively, slightly larger than our differences (up to 2.0% for the U-O bonds). The percentage changes in ε for U-O bond are very large, but as the absolute data are so small (< 0.01) these percentage changes are arguably not meaningful.

The differences in the QTAIM data for the U-O bonds between gas phase, COSMO and PEECM calculations are very small and much less than those between the theoretical and experimental data, indicating that the latter differences are unlikely to be due to long range electrostatic effects within the crystal. As mentioned in the introduction, experimental charge density distributions are generally refined with the Hansen-Coppens multipole model,[54] as was the case for $Cs_2UO_2Cl_4$,[50,51] and several limitations in describing the electron density *via* the multipole model have been noted previously.[55] In the case of $Cs_2UO_2Cl_4$ in particular, the polar U-O bond and the level at which the multipoles were truncated in the experimental study could be important factors. This could be a source of difference between the QTAIM data obtained from experiment, and the data I have calculated.

Differences between QTAIM values obtained from theory and experiment using multipole models have also been reported in previous studies on organic molecules,[57–60] as well as other systems containing polar bonds[62,64]. In the organic molecule studies experimental values of the Laplacian were up to 1.3 a.u. higher than theory for C=O bonds and 0.5 a.u. lower for N-H bonds, and hence the present difference between experiment and theory of approximately 0.3 a.u. for $\nabla^2\rho_b$ in the U-O bonds is typical of the differences found in other bonds. Although differences between the experimental and theoretical values of ρ_b were

also noted in these studies, these were significantly smaller than for $\nabla^2\rho_b$. For example, in the study by Rykounov *et al.*, the maximum difference in ρ_b between theory and experiment was 0.04 a.u., with the largest differences seen for bonds involving N or O atoms.[57]

I was interested to establish if there is a density functional dependence of the QTAIM values and so re-calculated $[UO_2Cl_4]^{2-}$ in the gas phase with five other exchange-correlation functionals; the results for the U-O and U-Cl bonds are shown in Table 2.3 and Table 2.4 respectively. Leaving the LDA data aside, the variation in the QTAIM metrics is very small for the U-Cl bonds, with differences in ρ_b, $\nabla^2\rho_b$ and H_b of less than 0.01 a.u. (< 1% for ρ_b, 2% for $\nabla^2\rho_b$ and 6% for H_b) between the different functionals. The functional dependence is slightly larger for $\nabla^2\rho_b$ and H_b for the U-O bonds; < 0.08 a.u. and 0.02 a.u. respectively, the former corresponding to a change of 14% between the B3LYP and TPSS functionals. None of these differences between functionals is as large as the difference between the theoretical and experimental ρ_b and $\nabla^2\rho_b$ data for the U-O bonds. This is similar to the findings of a study on S-N polar bonds in organic molecules[64], which found a small difference in $\nabla^2\rho_b$ between functionals (as well as between DFT and MP2), which could not account for the difference in $\nabla^2\rho_b$ between experiment and theory for these bonds.

The differences between the LDA QTAIM data and those from the GGA and post-GGA functionals are much larger than between the latter, particularly for $\nabla^2\rho_b$ for U-O, and H_b and DI for U-Cl, which have differences of 26.7%, 90.7% and 57.0% respectively compared with B3LYP. Clearly the electron density in these systems is described significantly differently at the LDA level when compared with GGA and beyond. Although the LDA functional gives better agreement with experiment for ρ_b and $\nabla^2\rho_b$of the U-O bonds, this is most likely coincidental.

	ρ_b (a.u.)	%	$\nabla^2\rho_b$ (a.u.)	%	H_b (a.u.)	%	ε	%	DI	%
B3LYP	0.303		0.345		-0.272		0.002		1.881	
LDA	0.287	-5.3	0.438	26.7	-0.261	-4.2	0.001	-54.1	1.877	-0.2
PBE	0.301	-0.7	0.380	10.0	-0.267	-1.9	0.002	25.1	1.930	2.6
PBE0	0.306	0.9	0.316	-8.4	-0.280	2.8	0.002	15.8	1.887	0.3
TPSS	0.299	-1.2	0.392	13.5	-0.264	-3.0	0.002	19.0	1.920	2.1
TPSSH	0.301	-0.5	0.365	5.7	-0.270	-0.9	0.002	16.4	1.905	1.2

Table 2.3 Bond critical point values of the electron density, ρ_b, Laplacian of the electron density, $\nabla^2\rho_b$, energy density, H_b, and ellipticity, ε, as well as delocalisation index, DI, for the U-O bonds in $[UO_2Cl_4]^{2-}$, calculated in gas phase with different exchange-correlation functionals. Percentage differences from the B3LYP data are given in the columns to the right of each metric.

	ρ_b (a.u.)	%	$\nabla^2\rho_b$ (a.u.)	%	H_b (a.u.)	%	ε	%	DI	%
B3LYP	0.061		0.146		-0.011		0.054		0.571	
LDA	0.072	17.4	0.118	-18.8	-0.021	90.7	0.018	-66.7	0.896	57.0
PBE	0.062	0.7	0.143	-1.9	-0.011	2.1	0.061	14.6	0.626	9.7
PBE0	0.062	1.0	0.145	-0.6	-0.011	5.6	0.058	8.1	0.563	-1.4
TPSS	0.061	-0.7	0.149	1.9	-0.010	-6.0	0.066	22.4	0.613	7.4
TPSSH	0.061	-0.4	0.149	1.9	-0.010	-3.6	0.063	17.9	0.588	3.0

Table 2.4 Bond critical point values of the electron density, ρ_b, Laplacian of the electron density, $\nabla^2\rho_b$, energy density, H_b, and ellipticity, ε, as well as delocalisation index, DI, for the U-Cl bonds in $[UO_2Cl_4]^{2-}$, calculated in gas phase with different exchange-correlation functionals. Percentage differences from the B3LYP data are given in the columns to the right of each metric.

2.3.2 $U(Se_2PPh_2)_4$ and $Np(Se_2PPh_2)_4$

In order to see if the similarities in the QTAIM data between gas phase and embedded calculations is true beyond $[UO_2Cl_4]^{2-}$, I have calculated analogous QTAIM metrics for $U(Se_2PPh_2)_4$ (Figure 2.2) and $Np(Se_2PPh_2)_4$, both of which have been previously studied with the QTAIM – with electron densities obtained from calculations.[38] There is no discrepancy with experiment in these systems, as they have not been studied experimentally with QTAIM, but the aim was to test the effect of environment on the QTAIM data of a different actinide-containing system. As for $[UO_2Cl_4]^{2-}$, $Cs_2UO_2Cl_4$ and $(Cs_2UO_2Cl_4)_7$, the QTAIM data have been calculated for $An(Se_2PPh_2)_4$ in the gas phase, in a polarizable continuum with COSMO and embedded in point charges (both natural and formal) with the PEECM. The average values for the An-Se, Se-P and P-C bonds, as well as the C-H bonds of the carbons in the para position of the phenyl ring (chosen as these bonds are closest to the edge of the QM region), are collected in Table 2.5, Table 2.6, Table 2.7, and Table 2.8 respectively.

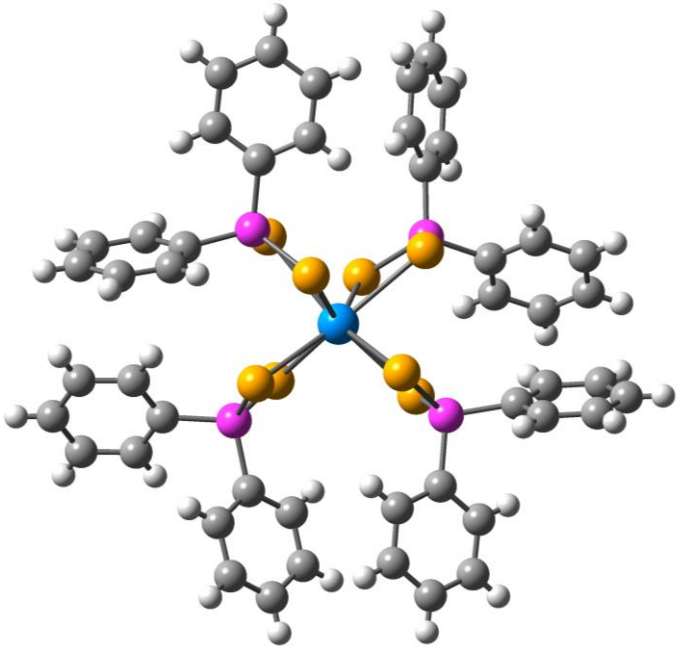

Figure 2.2 Ball and stick representation of $U(Se_2PPh_2)_4$. Carbon atoms are shown in grey, hydrogen atoms in white, phosphorus atoms in pink, sulfur atoms in yellow, and the uranium atom in blue. Atomic positions taken from reference[38].

As noted previously[38], the small values of ρ_b and H_b for the actinide-selenium bonds calculated in gas phase indicate that these are mostly ionic. These

conclusions are unaltered by the effects of COSMO solvation or embedding *via* the PEECM, especially so for the An-Se and para C-H bonds which have less than a 1% change in their ρ_{b}, $\nabla^2\rho_{\mathrm{b}}$, and H_{b} values, corresponding to differences of less than 0.01 a.u. in ρ_{b} and H_{b} and less than 0.02 a.u. in $\nabla^2\rho_{\mathrm{b}}$. The Se-P and P-C bonds show larger changes in $\nabla^2\rho_{\mathrm{b}}$, with up to 5% difference for the Se-P bond and 9% difference for the P-C bond, most notably for the COSMO calculations. However, even these changes are still rather modest, and it is worth noting that the changes are similar between the uranium and neptunium systems; hence a comparative trend in QTAIM data between actinides is largely unaffected by the environment.

		ρ_b (a.u.)	%	$\nabla^2\rho_b$ (a.u.)	%	H_b (a.u.)	%	ε	%	DI	%
$U(Se_2PPh_2)_4$	Gas phase	0.045		0.063		-0.008		0.174		0.495	
	COSMO	0.045	-0.1	0.063	0.1	-0.008	-0.5	0.167	-4.3	0.499	0.8
	PEECM Natural	0.045	-0.1	0.063	-0.1	-0.008	-0.1	0.162	-6.9	0.495	0.0
	PEECM Formal	0.045	-0.1	0.063	-0.1	-0.008	-0.1	0.160	-8.2	0.495	0.0
$Np(Se_2PPh_2)_4$	Gas phase	0.045		0.065		-0.008		0.159		0.505	
	COSMO	0.045	-0.1	0.065	0.2	-0.008	-0.5	0.155	-2.5	0.505	0.0
	PEECM Natural	0.045	0.0	0.065	0.1	-0.008	-0.1	0.154	-2.9	0.505	0.1
	PEECM Formal	0.045	0.0	0.065	0.1	-0.008	-0.1	0.157	-1.4	0.505	0.0

Table 2.5 Bond critical point values of the electron density, ρ_b, Laplacian of the electron density, $\nabla^2\rho_b$, energy density, H_b, and ellipticity, ε, as well as delocalisation index, DI, for the An-Se bond in $U(Se_2PPh_2)_4$ and $Np(Se_2PPh_2)_4$. Both systems are calculated in the gas phase, with a polarizable continuum solvent model *via* COSMO and with the PEECM with natural and formal charges in the embedding region. ρ_b, $\nabla^2\rho_b$, and H_b are in atomic units. Percentage differences from the gas phase data are given in the columns to the right of each metric.

		ρ_b (a.u.)	%	$\nabla^2\rho_b$ (a.u.)	%	H_b (a.u.)	%	ε	%	DI	%
$U(Se_2PPh_2)_4$	Gas phase	0.131		-0.123		-0.075		0.026		1.170	
	COSMO	0.131	0.2	-0.128	4.2	-0.075	0.5	0.023	-12.3	1.158	-1.0
	PEECM Natural	0.131	0.1	-0.125	1.7	-0.075	0.2	0.024	-6.5	1.165	-0.4
	PEECM Formal	0.131	0.0	-0.124	0.7	-0.075	0.1	0.026	-1.7	1.168	-0.2
$Np(Se_2PPh_2)_4$	Gas phase	0.131		-0.125		-0.076		0.031		1.170	
	COSMO	0.132	0.2	-0.131	4.2	-0.076	0.5	0.027	-11.5	1.158	-1.0
	PEECM Natural	0.132	0.1	-0.128	1.7	-0.076	0.2	0.029	-5.0	1.165	-0.4
	PEECM Formal	0.132	0.0	-0.127	0.8	-0.076	0.1	0.030	-2.0	1.168	-0.2

Table 2.6 Bond critical point values of the electron density, ρ_b, Laplacian of the electron density, $\nabla^2\rho_b$, energy density, H_b, and ellipticity, ε, as well as delocalisation index, DI, for the Se-P bond in $U(Se_2PPh_2)_4$ and $Np(Se_2PPh_2)_4$. Both systems are calculated in the gas phase, with a polarizable continuum solvent model *via* COSMO and with the PEECM with natural and formal charges in the embedding region. ρ_b, $\nabla^2\rho_b$, and H_b are in atomic units. Percentage differences from the gas phase data are given in the columns to the right of each metric.

		ρ_b (a.u.)	%	$\nabla^2\rho_b$ (a.u.)	%	H_b (a.u.)	%	ε	%	DI	%
U(Se2PPh2)4	Gas phase	0.172		-0.215		-0.175		0.067		0.777	
	COSMO	0.173	0.4	-0.234	8.5	-0.176	0.8	0.069	3.7	0.786	1.2
	PEECM Natural	0.172	0.2	-0.223	3.6	-0.175	0.3	0.068	1.4	0.781	0.5
	PEECM Formal	0.172	0.1	-0.218	1.3	-0.175	0.1	0.067	0.6	0.778	0.2
Np(Se2PPh2)4	Gas phase	0.173		-0.208		-0.178		0.066		0.773	
	COSMO	0.173	0.5	-0.226	8.8	-0.177	-0.2	0.069	3.5	0.783	1.2
	PEECM Natural	0.173	0.2	-0.216	3.7	-0.176	-0.7	0.067	1.4	0.777	0.5
	PEECM Formal	0.173	0.1	-0.211	1.6	-0.176	-0.9	0.067	0.7	0.775	0.2

Table 2.7 Bond critical point values of the electron density, ρ_b, Laplacian of the electron density, $\nabla^2\rho_b$, energy density, H_b, and ellipticity, ε, as well as delocalisation index, DI, for the P-C bond in $U(Se_2PPh_2)_4$ and $Np(Se_2PPh_2)_4$. Both systems are calculated in the gas phase, with a polarizable continuum solvent model *via* COSMO and with the PEECM with natural and formal charges in the embedding region. ρ_b, $\nabla^2\rho_b$, and H_b are in atomic units. Percentage differences from the gas phase data are given in the columns to the right of each metric.

		ρ_b (a.u.)	%	$\nabla^2\rho_b$ (a.u.)	%	H_b (a.u.)	%	ε	%	DI	%
$U(Se_2PPh_2)_4$	Gas phase	0.406		-2.016		-0.617		0.001		1.001	
	COSMO	0.408	0.6	-2.037	1.1	-0.615	-0.3	0.001	-45.7	0.998	-0.3
	PEECM Natural	0.407	0.3	-2.029	0.6	-0.616	-0.2	0.001	25.1	1.000	-0.2
	PEECM Formal	0.407	0.2	-2.025	0.5	-0.616	-0.1	0.001	12.6	0.999	-0.2
$Np(Se_2PPh_2)_4$	Gas phase	0.405		-2.008		-0.616		0.002		0.999	
	COSMO	0.407	0.6	-2.029	1.0	-0.614	-0.3	0.003	19.8	0.995	-0.3
	PEECM Natural	0.406	0.3	-2.020	0.6	-0.615	-0.2	0.003	16.6	0.997	-0.1
	PEECM Formal	0.406	0.2	-2.016	0.4	-0.616	-0.1	0.003	18.1	0.997	-0.2

Table 2.8 Bond critical point values of the electron density, ρ_b, Laplacian of the electron density, $\nabla^2\rho_b$, energy density, H_b, and ellipticity, ε, as well as delocalisation index, DI, for the para C-H bond in $U(Se_2PPh_2)_4$ and $Np(Se_2PPh_2)_4$. Both systems are calculated in the gas phase, with a polarizable continuum solvent model *via* COSMO and with the PEECM with natural and formal charges in the embedding region. ρ_b, $\nabla^2\rho_b$, and H_b are in atomic units. Percentage differences from the gas phase data are given in the columns to the right of each metric.

2.4 Conclusions

I wanted to consider whether, as had been suggested, environmental effects account for the differences observed in the experimental and theoretical QTAIM ρ_b and $\nabla^2\rho_b$ for the U-O bonds in $Cs_2UO_2Cl_4$. I have investigated the effects of environment on the QTAIM metrics of bonds in uranium and neptunium containing systems. These effects have been incorporated using the COSMO and PEECM approaches; both have very modest effects on the QTAIM data, and I conclude that they cannot account for the differences seen between theory and experiment in $Cs_2UO_2Cl_4$. The effect of the exchange-correlation functional on the QTAIM data was also tested, although the functional had a relatively more significant effect on the data, its impact was still too small to account for the difference between experiment and theory. Rather, these differences may be due to deficiencies in the refinement of experimental electron density data *via* the multipole model, as has been previously seen for other polar covalent bonds.

The effect of environment was then tested on two different systems (which contained actinide atoms) and again the effects of using the COSMO or PEECM approaches were modest. The data strongly suggest that QTAIM studies of molecular electron densities calculated in gas phase are adequate for the study of actinide systems, and also that, once beyond the local density approximation, there is only a small dependence of the QTAIM metrics on the exchange-correlation functional employed.

3 Electronic Structure of AnO_2 with PEECM

3.1 Introduction

The focus of the rest of the thesis is turned towards actinide dioxides, in particular UO_2 and PuO_2. The interest in PuO_2 is due to its industrial relevance: of the world's c. 250 tonnes of separated civil plutonium, more than 100 tonnes are stored at Sellafield in the UK.[76] The plutonium stock comes from two reprocessing plants, the Magnox reprocessing plant which deals with fuel from Britain's early nuclear reactors, and the Thermal Oxide Reprocessing Plant (Thorp), which deals with fuel from British Advanced Gas-cooled Reactors (AGR) and Light Water Reactors (LWR) from around the world.[77] The plants receive used nuclear fuel and separate out the uranium, plutonium and waste products. The uranium and plutonium are then converted into the oxides, which can be manufactured into new uranium oxide or mixed oxide (MOX) fuel.

The current UK government's policy is to store this stock of civil plutonium as PuO_2 until it can either be used in the production of MOX fuel for use in civil nuclear reactors, or otherwise immobilized and treated as waste for disposal.[78]

The PuO_2 is stored as powder in sealed steel cans (Figure 3.1), under certain circumstances, gas generation may occur in these cans, with consequent pressurisation. This is one of the most serious fault scenarios to be considered in the safety cases for PuO_2 interim storage. Several routes to gas production have been suggested, including (i) steam produced by H_2O desorption from hygroscopic PuO_2[79] (ii) radiolysis of adsorbed water (iii) generation of H_2 by chemical reaction of PuO_2 with H_2O, producing a PuO_{2+x} phase[80] and (iv) generation of He gas resulting from alpha decays within the PuO_2. In addition, the PuO_2 surface can act as a catalyst towards the recombination of gases to their more stable chemical form. Many of these processes involve PuO_2/H_2O interactions, and are complex, inter-connected and poorly understood. The interaction of water with the surface will be discussed in greater detail in Chapter 4 and the remaining chapters of this thesis.

Figure 3.1 Steel cans used for the storage of plutonium dioxide powder, from[76]

UO_2 is of interest in its own right, due its use in the nuclear fuel cycle (it is the primary component of fuels in many nuclear reactors, and is also used in the manufacture of MOX fuel), but it is also of interest in relation to PuO_2. UO_2 has been studied in much greater detail (both experimentally and theoretically) than PuO_2, so when creating a new model to investigate actinide dioxide systems, it can act as a better benchmark with previous results than PuO_2 can. Additionally, UO_2 can be used as a surrogate system in experimental studies – UO_2 and PuO_2 are isostructural – where it is difficult to work with PuO_2, so testing whether this is appropriate by seeing if water interacts in a similar way on both surfaces would also be useful.

The PEECM is useful for this study, it was developed to study ionic solids such as actinide dioxides, and has been used to investigate the isostructural CeO_2.[22] However, most studies on AnO_2 systems have been performed with periodic DFT, so the PEECM could offer additional insights. The PEECM offers certain advantages over periodic boundary condition (PBC) approaches; not only can all of the analysis tools of molecular quantum chemistry be applied, but it is relatively straightforward to employ DFT with hybrid functionals and makes the study of defects, such as oxygen vacancies, in isolation possible.

The remaining chapters therefore focus on developing a model for AnO_2, using the PEECM, to study the interaction of water on its surfaces. However, before going on to study this, we need to ensure when using the PEECM as a model

that the correct electronic structure can be calculated for UO_2 and PuO_2, which has been problematic for theoretical studies. The rest of this introduction will focus on the electronic structure of AnO_2 systems, and results that have been obtained from previous theoretical studies.

3.1.1 Experimental Studies of AnO_2 Electronic Structure

Actinide dioxides adopt the fluorite (CaF_2) structure, where the actinide ions are at the centre of a cube formed with oxygen ions at the corners and are 8-coordinate, while the oxygen ions lie in a tetrahedral 4-coordinate environment (Figure 3.2).

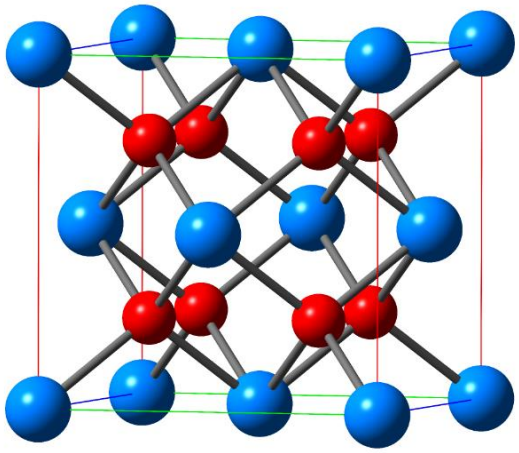

Figure 3.2 Unit cell of AnO_2 in fluorite structure. Actinide atoms shown in blue, oxygen atoms shown in red.

If the oxygen ions in AnO_2 are considered as divalent then the actinide ions are tetravalent which corresponds to $5f^2$, $5f^3$, and $5f^4$ configurations for U, Np, and Pu respectively. However, the electronic structure of the actinide oxides is complicated, as these systems can exhibit either electron localization or delocalization as well as having partially occupied f levels.

ThO_2,[81,82] UO_2,[83,84] NpO_2,[85] and PuO_2[85] are all known to be insulators, with ThO_2 having a large band gap of 6 eV[81], while UO_2, NpO_2, and PuO_2 have much smaller band gaps with experimental measurements of 2.1 eV,[83] 2.85 eV,[85] and 2.80 eV.[85]

As the actinide series is crossed the 5f levels move to lower energies; this can be seen in Figure 3.3, taken from periodic DFT calculations with the hybrid HSE

functional, where the composition of valence and conduction bands agree with that from experiment. For ThO_2, which has no 5f electrons, the unoccupied 5f levels are located in the 6d conduction band, and the valence band is comprised of oxygen 2p levels.

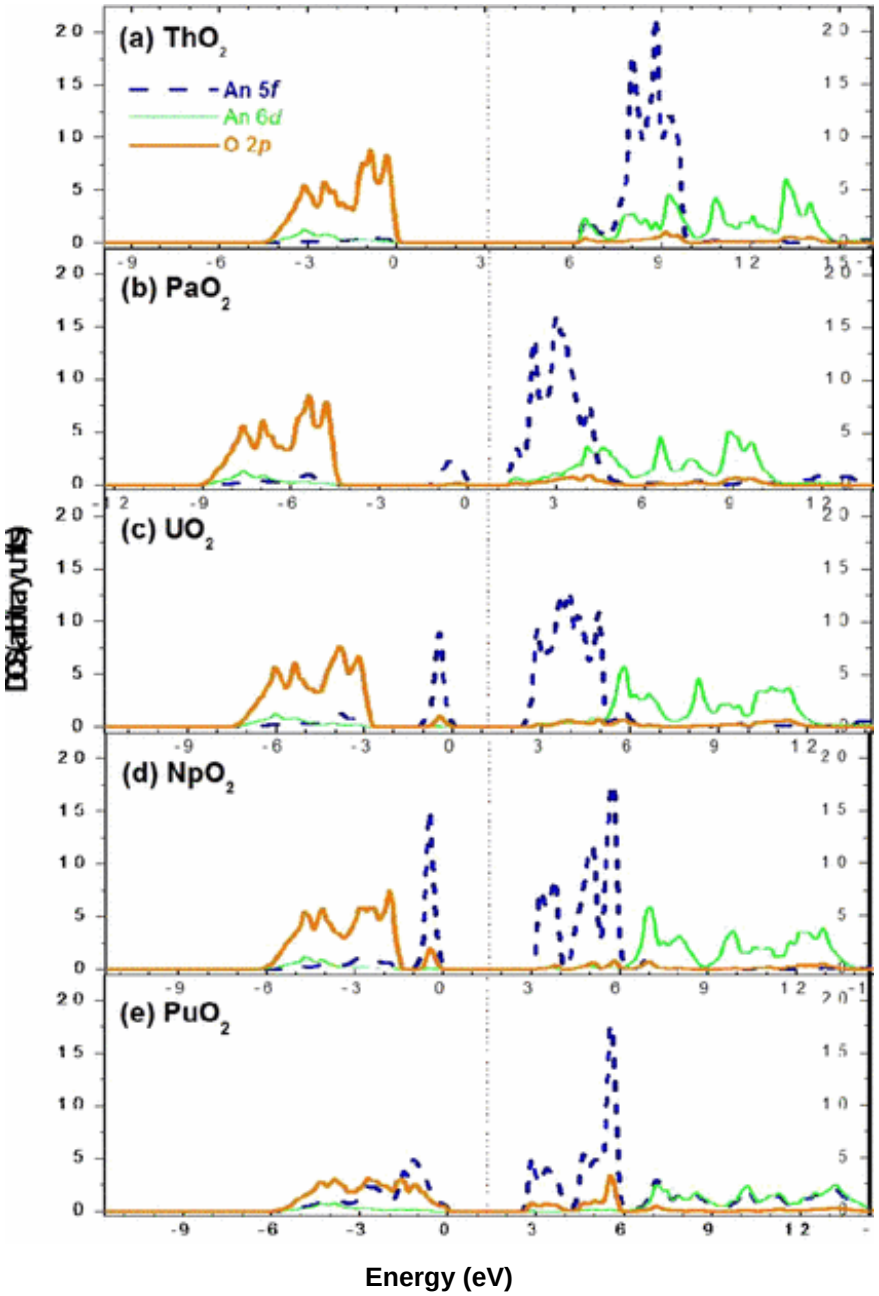

Figure 3.3 Partial density of states (PDOS) from DFT calculations with the HSE functional for optimized bulk AnO_2 structures (An = Th-Pu). The Fermi energy is defined as zero and placed at the top of the valence band. Position of An 5f, 6d and O 2p levels relative to each other agree with experiment for UO_2 and PuO_2. Modified from Prodan *et al.*[86]

For UO_2 the occupied 5f levels, as seen from photoelectron spectroscopy (PES), comprise the valence band,[84,87] they lie between the occupied oxygen 2p levels

and the unoccupied uranium 6d levels. In addition the unoccupied 5f levels are now lower in energy than the 6d levels, and comprise the conduction band, as seen from x-ray adsorption spectroscopy (XAS),[88] and hence UO_2 is a Mott-Hubbard insulator with f-f transitions.

NpO_2 has a similar electronic structure to UO_2; a PES study looking at oxidizing Np metal to NpO_2 found that the valence band of NpO_2 is comprised of Np 5f levels, with O 2p levels at lower energies.[89]

When PuO_2 is reached the occupied 5f levels have lowered further in energy and are now located at the top of the occupied oxygen 2p band, as seen from PES.[90] Therefore, as the top of the valence band now has oxygen character it is no longer a Mott-Hubbard insulator but a ligand to metal charge transfer (LMCT) insulator.

3.1.2 Computational Studies of AnO_2 Electronic Structure

The 5f electrons in actinide oxides, along with the 3d electrons in first row transition metal and 4f electrons in lanthanide oxides, are strongly correlated and localized on the metal ions. This leads to weak overlap, in the case of the actinide dioxides, with neighbouring oxygen ions. However, DFT within the LDA or GGA approaches poorly describes these systems due to the self-interaction error, predicting the actinide dioxides to be metallic.[91–93] Various methods have been used to account for this including DFT+*U*,[88,94–98] SIC,[15] DMFT,[99] and hybrid functionals, [86,91,92,100] in this section I will discuss DFT+*U*, arguably the most widely used method, and hybrid functionals, which are used for the majority of calculations in this thesis.

DFT+*U* is a method often used when investigating the actinide dioxides, in order to correct the LDA and GGA electronic structure, i.e. to find the AnO_2 systems to be insulators. The DFT+*U* method involves including a Hubbard term, *U*, in the Hamiltonian, which helps to better describe the onsite correlation of localized electrons.

U is applied to only a subset of electrons, usually the localized and highly correlated d or f electrons. In the case of actinide oxides, the *U* term is applied to only the 5f electrons.

U can be estimated either experimentally or theoretically, however it is most often selected in calculations to give agreement with certain values, such as the lattice parameters or the band gap. Using a value of *U* greater than 0 will usually open up a band gap in the system, with increasing values of *U* leading to a larger band gap, however, matching the value of *U* to the band gap can lead to discrepancies with other values, such as the lattice parameters.

DFT+*U* calculations on UO_2 have predicted the correct Mott-Hubbard insulating system that is seen experimentally, and has been achieved with both LDA+*U*,[94,95] as well as GGA+*U* methods.[88,96] The value of *U* used is usually ~4 eV, which has been justified due to experimental results,[94,95] as well adjusting its value to give band gaps[88] or lattice parameters[101] that agree with experiment.

As mentioned, from experiment NpO_2 is known to be a Mott-Hubbard insulator, however DFT+*U* studies have differed in finding NpO_2 to be a Mott-Hubbard insulator or a LMCT insulator, with the occupied 5f levels in the O 2p valence band. Increasing the value of *U* moves the occupied 5f levels to lower energies; Wang *et al.*[97] investigated the effect of increasing the value of *U* with LDA+*U* and GGA+*U*, from *U*=0 eV to *U*=6 eV. They found at *U*=4 eV the occupied 5f levels formed the valence band, in agreement with experiment, however, when the value of *U* is increased to 6 eV the occupied 5f band is further lowered in energy and the valence band is comprised mainly of the O 2p levels.

Similarly on PuO_2 with LDA+*U* and GGA+*U*, increasing the *U* value moves the occupied 5f levels to lower energies[98]. With a *U* value of 4 eV the valence band contains a significant proportion of the O 2p level, indicating a LMCT insulator, as is found from experiment, while for smaller values of *U* an f-f transition Mott-Hubbard insulator is predicted.

Within periodic DFT, the HSE and PBE0 hybrid exchange-correlation functionals have also been used to study AnO_2 predicting the correct insulating state for UO_2,[86,91,92,100] NpO_2,[86] and PuO_2.[86,91,102] Hybrid functionals offer an advantage that there is no *U* value that has to be fitted to produce the results (although the amount of exact exchange has been pre-fitted to empirical data in producing the functional). The use of hybrid functionals in periodic systems has been limited as

they are computationally expensive due to their inclusion of exact exchange. However, when used with cluster based systems the increase in computational expense is reduced, therefore it was my hope that I could use them to calculate the correct electronic structure in the clusters.

Although hybrid functionals have been shown to give the correct electronic structure in periodic calculations on AnO_2, they have not been used with cluster based calculations of these systems. I therefore test the GGA PBE functional and the hybrid PBE0 functional, to see if the correct insulating nature of the AnO_2 systems and the composition of their valence and conduction bands can be calculated.

3.2 Computational Details

Again the TURBOMOLE program[67] was used for calculations, implementing DFT with the PBE[13] (GGA) and PBE0[16] (hybrid-GGA) exchange-correlation functionals.

The self-consistent field convergence was set to $1x10^{-6}$ a.u. The def-SV(P) basis sets[103,104] contained in the TURBOMOLE library were used for all oxygen atoms and actinides that used a small core pseudopotential (PP) (see below), and the double-zeta MWB-AVDZ[105] basis set was used for actinide atoms using a large core PP.

PPs were used for the actinide ions in the quantum mechanically treated cluster; small-core (60 electron) def-PPs from the TURBOMOLE library[106,107] or, where stated, large-core PPs incorporating the 5f electrons,[105] corresponding to 80, 81, or 82 electron cores for U, Np, and Pu respectively – these are electrons with principal quantum number 5 or lower. These 5f-in-core PPs have been parameterized specifically for tetravalent states. When the 5f-in-core PPs are used the clusters are written as $An_xAn_yO_{2(x+y)}$ where x refers to the number of actinide ions with explicit 5f electrons and y to the number of actinide ions described by 5f-in-core PPs.

Density of states (DOS) diagrams were produced for the bulk AnO_2 electronic structure calculations by Gaussian smearing of Kohn-Sham orbital energies; the

Fermi energy is taken as the top of the highest occupied band. The projected (P)DOS were produced by Mulliken partitioning of orbitals into s, p, d and f contributions within the TURBOMOLE 6.5 program.

As lattice parameters cannot be optimized within the PEECM, experimental lattice parameters were used, a = 5.470, 5.420, 5.398 Å for UO_2, NpO_2 and PuO_2 respectively, which are all in the space group $Fm\bar{3}m$. Theoretical values of the lattice parameter of UO_2 span a wide range of almost 0.3 Å, from 5.28 Å calculated with LDA[92], to 5.568 Å calculated with PBE+U.[93] GGA+U generally overestimates the lattice parameters of actinide dioxides,[97,98,108,109] while hybrid functionals tend to slightly underestimate the lattice parameters,[91,92,102] hence the preference for the experimental values.

In the calculations the metals ions are coupled ferromagnetically, in which there are 2, 3, or 4 unpaired electrons per actinide ion for UO_2, NpO_2, and PuO_2 respectively. The difference in energy between ferromagnetic and antiferromagnetic magnetic ordering in actinide oxides has been seen in previous theoretical studies to be in the order of tens of meV with a hybrid functional.[91,102,110] I tried to calculate a singlet state for the UO_2 bulk cluster, although I could not obtain a sensible electronic structure. Therefore, as has been done in some previous studies on water adsorption on actinide dioxide surfaces,[108,111] to simplify the calculations I do not consider antiferromagnetic ordering in the systems.

3.2.1 PEECM

The single-point bulk AnO_2 calculations were all performed with the PEECM; AnO_2 clusters were embedded in 3D point charge arrays to simulate the bulk. The PPs used in the intermediate region were the Ce CRENBL PPs,[112] employed in order to avoid overpolarization of the electron density in the explicit cluster, while -2 charges again represented the oxygen ions. The Ce CRENBL PP, which corresponds to a +4 charge when used without any basis functions, was used since no actinide PPs corresponding to a +4 charge were available. The 8-coordinate Ce(IV) ionic radius, 0.97 Å, is similar to that of U(IV), 1.00 Å, Np(IV), 0.98 Å and Pu(IV) 0.96 Å.[2] Formal charges had to be used in the intermediate

region for oxygen in order to counterbalance the +4 charge of the PPs, therefore I also used formal charges for the infinite outer embedding region: +4 for actinide ions and -2 for oxygen ions.

3.3 **Results**

I began by studying the electronic structure of bulk AnO_2; single point calculations were performed on $An_{16}O_{32}$ clusters, shown in Figure 3.4, embedded in 3D arrays of point charges to simulate the bulk.

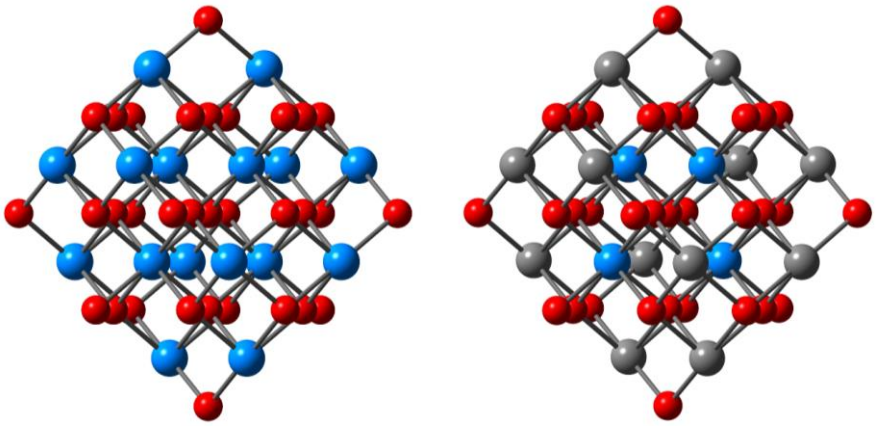

Figure 3.4 $An_{16}O_{32}$ cluster (left) and $An_4An_{12}O_{32}$ cluster (right), oxygen ions shown in red, actinide ions in blue and grey. Grey spheres represent actinide ions treated with 5f-in-core PPs. Embedding ions not shown.

The PBE exchange-correlation functional was initially used to produce a PDOS plot of the three bulk AnO_2 systems studied, which can be seen in Figure 3.5. The PBE functional predicts the three AnO_2 systems studied to be metallic, with the Fermi level cutting through the 5f levels for each one. Furthermore for PuO_2 there is a gap between the Pu 5f and the O 2p levels, with the O 2p levels not comprising the valence band.

Hence the PBE functional incorrectly describes the electronic structure, which is experimentally characterised as a Mott-Hubbard insulator for UO_2[88] and NpO_2[89] and a LMCT insulator for PuO_2[90]. As mentioned in the introduction, this deficiency of GGA (and LDA) functionals has been noted in periodic DFT too.

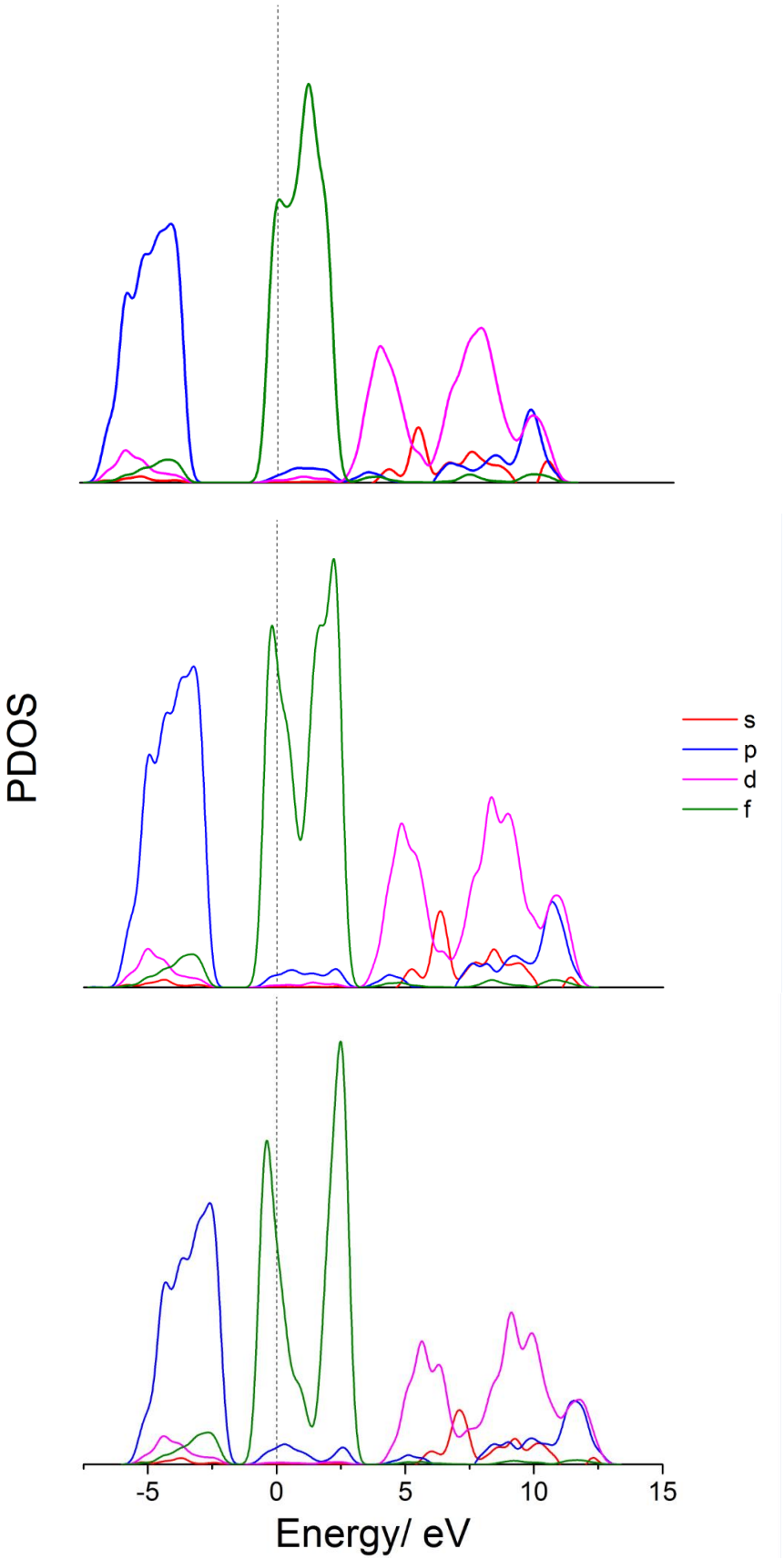

Figure 3.5 PDOS of bulk AnO_2 (An = U (top), Np, Pu (bottom)) modelled as $An_{16}O_{32}$ clusters with the PEECM and the PBE functional. Vertical line shows Fermi level. Vertical scale in arbitrary units.

When the PBE0 functional is used it can be seen from the PDOS plots, Figure 3.6, that each AnO_2 cluster is predicted to be an insulator. From the decomposition of the states into their s, p, d, and f contributions it can be seen that UO_2 and NpO_2 both have valence and conduction levels of f character. They are hence both predicted to be Mott-Hubbard insulators, exhibiting f-f transitions.

The occupied f levels in NpO_2 are more stabilized than in UO_2, lying closer in energy to the valence oxygen p levels, in agreement with a hybrid functional study using periodic DFT.[86] The HOMO-LUMO gaps are 3.2 eV and 3.6 eV for UO_2 and NpO_2 respectively, higher than the experimental band gaps of 2.1 eV[83] and 2.85 eV.[85] This overestimation arises in part as we are considering gaps between discrete energy levels and not band gaps; a previous periodic DFT study using PBE0 calculated a gap of 2.6 eV[92], closer to the experimental value of 2.1 eV. However, the aim is not to predict the band gaps quantitatively, arguably something that cannot be achieved with standard DFT, rather to qualitatively predict the correct insulating state with an embedded cluster method.

PuO_2 has 5f levels that are more stable than those of UO_2 and NpO_2, with energies comparable with the highest O 2p valence levels. Thus, as noted in the introduction, PuO_2 is not a Mott-Hubbard insulator, as there is a significant contribution of oxygen 2p valence levels at the valence band edge. PuO_2 is better described as an LMCT system, in agreement with experiment.[90] The HOMO-LUMO gap for the cluster is 3.3 eV, again larger than the experimental value of 2.80 eV[85] as we are considering gaps between discrete energy levels.

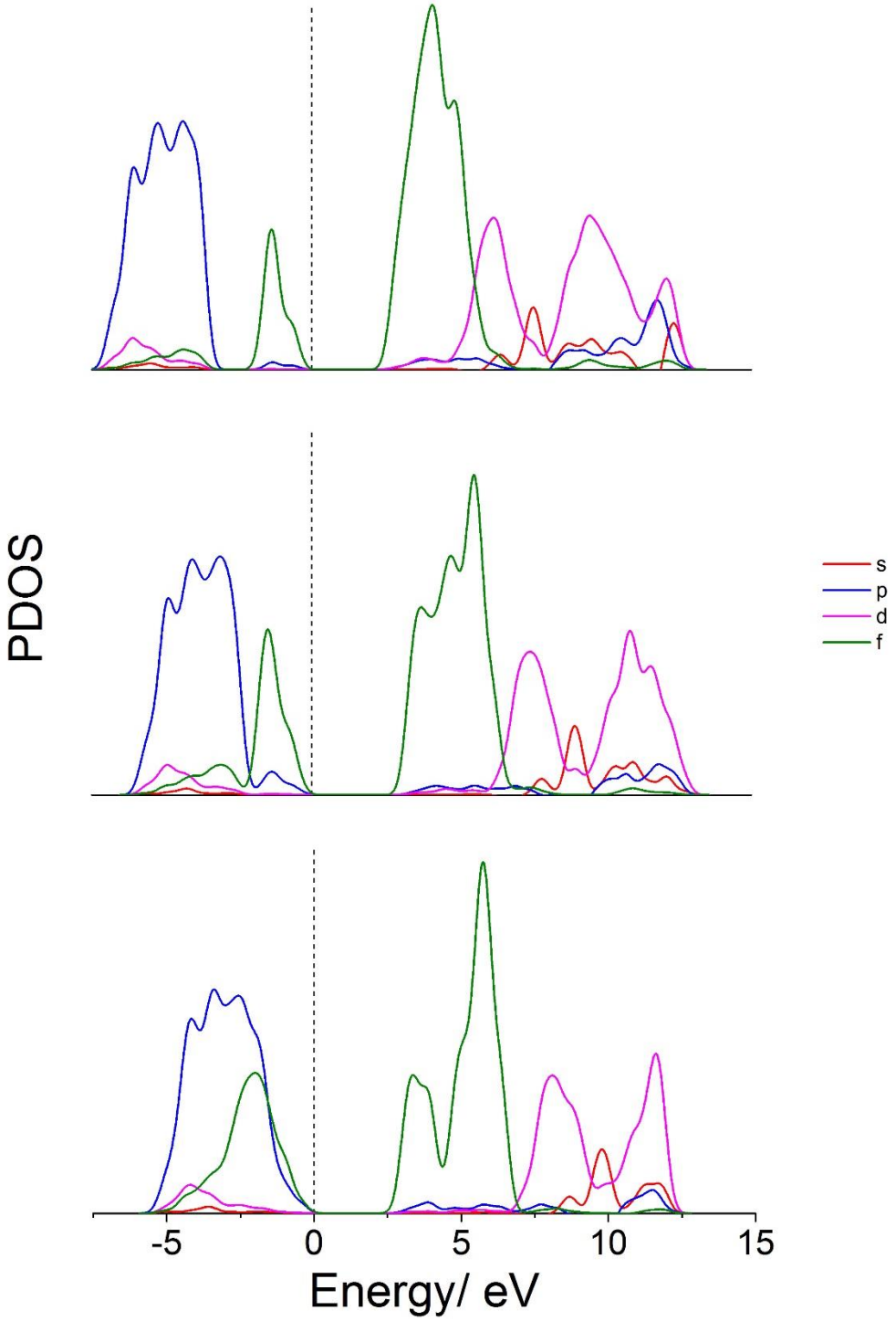

Figure 3.6 PDOS of bulk AnO_2 (An = U (top), Np, Pu (bottom)) modelled as $An_{16}O_{32}$ clusters with the PEECM and the PBE0 functional. Vertical line shows Fermi level. Vertical scale in arbitrary units.

These electronic structure calculations are computationally not too expensive, however in the following chapters when I will be using surface clusters, I will be performing geometry optimizations, which will greatly increase the computational cost. In order to explore approaches to speeding up the calculations, I have considered using large-core PPs, where the 5f electrons of the actinides are considered to be in the core, these PPs would be used for actinide atoms not directly involved in adsorption in the surface clusters. However, I wanted to first check the effect of using these large core PPs on the electronic structure of the bulk clusters. Therefore the electronic structure of the $An_{16}O_{32}$ clusters were recalculated with the outer 12 actinide ions described with 5f-in-core PPs, while the inner 4 ions were still treated with explicit 5f electrons, i.e. $An_4An_{12}O_{32}$ (Figure 3.4).

The PDOS plots for the bulk $An_4An_{12}O_{32}$ clusters are shown in Figure 3.7. A similar electronic structure to that shown in Figure 3.6 is obtained, i.e. for UO_2 and NpO_2 insulators with valence and conduction 5f levels, and for PuO_2 an insulator with a valence band comprised of O 2p levels, and a conduction band of 5f levels (Figure 3.7). The PDOS of the 5f levels is lower due to fewer 5f electrons being described explicitly.

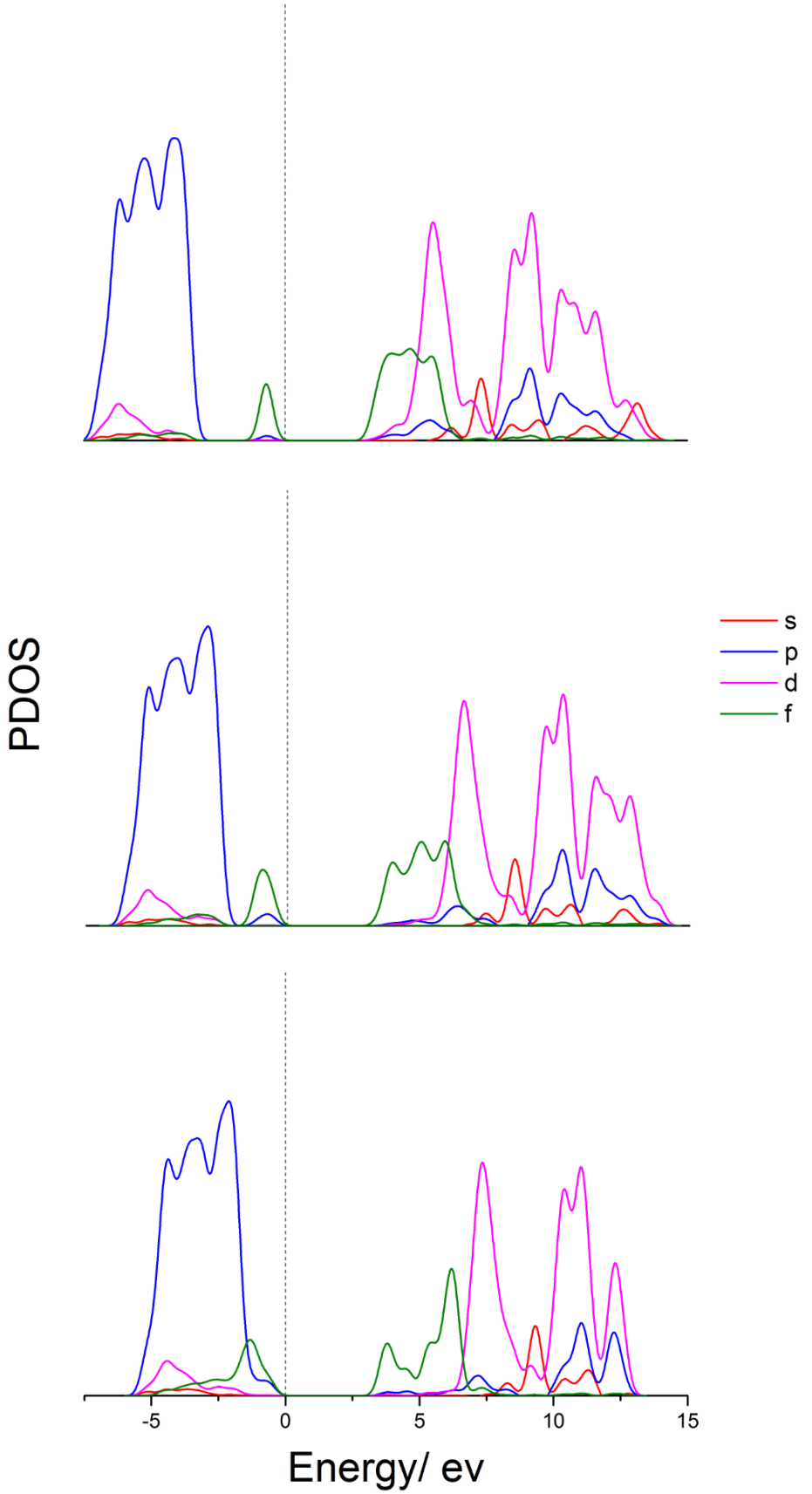

Figure 3.7 PDOS of bulk AnO_2 (An = U (top), Np, Pu (bottom)) modelled as $An_4An_{12}O_{32}$ clusters (Figure 3.4) with the PEECM and the PBE0 functional, where 12 uranium ions are described with 5f-in-core PPs. Vertical line shows Fermi level. Vertical scale in arbitrary units.

The spin densities were calculated and are shown for $U_{16}O_{32}$ and $U_4U_{12}O_{32}$ in Figure 3.8. The unpaired electrons are clearly localized on the uranium ions; in the case of the $U_4U_{12}O_{32}$ cluster the unpaired electrons are localized on the four uranium ions which treat the 5f electrons explicitly. The spin densities, from Mulliken analysis, of each uranium ion in the $U_{16}O_{32}$ cluster range from 2.04–2.07 a.u., with the f contribution to this spin density being 1.99–2.00 a.u., i.e. two unpaired f electrons on each uranium ion. The spin densities of the four inner uranium ions of the $U_4U_{12}O_{32}$ cluster are similar to that of $U_{16}O_{32}$, with the number of unpaired electrons and their f contribution differing by less than 0.03 a.u.

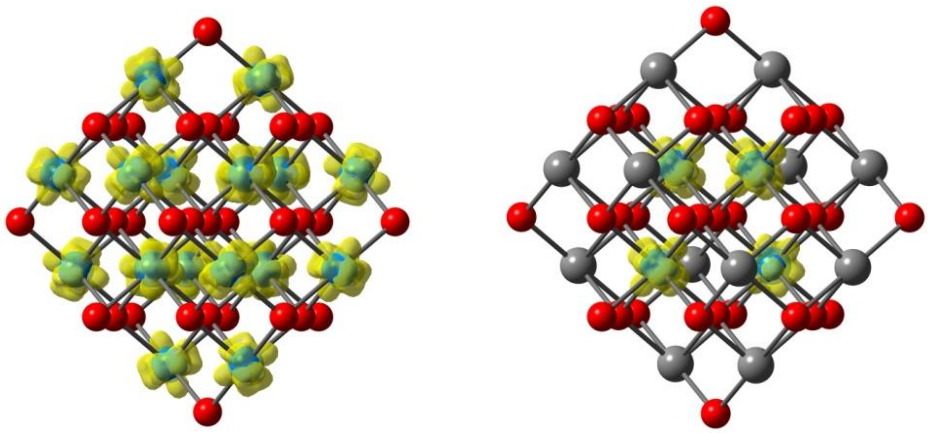

Figure 3.8 Spin density, shown in yellow, of $U_{16}O_{32}$ (left) and $U_4U_{12}O_{32}$ (right), oxygen ions shown in red. Grey spheres represent uranium ions treated with 5f-in-core PPs.

The spin densities were also calculated for $Pu_{16}O_{32}$ and $Pu_4Pu_{12}O_{32}$, when plotted they look like Figure 3.8, i.e. the spin density is localised on the plutonium atoms (and in the case of $Pu_4Pu_{12}O_{32}$ on the inner four plutonium atoms). From Mulliken analysis the spin densities in the $Pu_{16}O_{32}$ cluster range from 4.09–4.12 a.u., with f contributions to the spin density ranging from 4.02–4.03 a.u., i.e. four unpaired electrons localised on each plutonium atom. As for uranium dioxide, the spin densities of the four inner plutonium atoms in $Pu_4Pu_{12}O_{32}$ do not differ greatly from the same atoms in $Pu_{16}O_{32}$, with a maximum difference of 0.02 a.u. in either the total spin density on an atom, or the f contribution to the spin density on a particular atom.

3.4 **Conclusions**

The PBE functional has been shown in an embedded cluster method to incorrectly describe the electronic structure of UO_2, NpO_2, and PuO_2, predicting a

metallic system, as is found in periodic DFT studies. When the hybrid PBE0 functional is used all three AnO_2 systems are predicted to be insulators, with the composition of the valence and conduction bands agreeing with experimental and previous theoretical results. As the PBE functional incorrectly describes the electronic structure, the PBE0 functional, although more expensive, is used for the subsequent studies on AnO_2 systems.

It has also been shown that when describing the cluster with a subset of actinide ions described by 5f-in-core PPs the correct electronic structure is still obtained, while significantly reducing the computational expense. This is important when geometry optimizations have to be performed – as in subsequent chapters – which becomes computationally very expensive.

4 Water Adsorption on UO_2 and PuO_2 (111) and (110)

4.1 Introduction

In the introduction of Chapter 3 I discussed why the study of PuO_2 and UO_2 is of industrial relevance – in particular how water adsorption has an impact on the surfaces of these materials – before going on to study the electronic structure of these systems with an embedded cluster method. I will now go on to consider water adsorption in more depth, firstly reviewing the literature on experimental as well as theoretical work, before investigating water adsorption myself with the PEECM.

4.1.1 Low Index Surfaces of AnO_2

The low index surfaces of the fluorite structure were classified as types I, II, and III by Tasker.[113] Type I surfaces are neutral, with stoichiometric numbers of ions in each plane, the AnO_2 (110) surface is type I (Figure 4.1). Actinide ions in the first layer of the (110) surface are six-coordinate and oxygen ions three-coordinate (compared to eight-coordinate and four-coordinate in the bulk respectively).

Type II surfaces, which include fluorite (111) surfaces, form a repeating layered structure, in the case of AnO_2 the layers are O-An-O, with an oxygen terminated surface (Figure 4.1). As the layers are stoichiometric charge neutrality is maintained through the surface and there is no dipole moment perpendicular to the surface. In the first layer the actinide ions are seven-coordinate, with oxygen ions three-coordinate.

The AnO_2 (100) surface is a type III surface, with O-An repeating layers (Figure 4.1), as these are not stoichiometric there is a dipole perpendicular to the surface, causing the surface to be unstable and undergo significant reconstructions. At this termination the oxygen ions at one side of the surface slab are only two-coordinate, while the actinide ions are eight-coordinate. The actinide and oxygen ions at the other side of the slab are both four-coordinate. Due to the dipole perpendicular to the surface, theoretical studies often move half of the surface oxygen atoms from one side of the slab to the other. This results in actinide ions

at both sides of the slab being six-coordinate, and oxygen ions being two-coordinate.

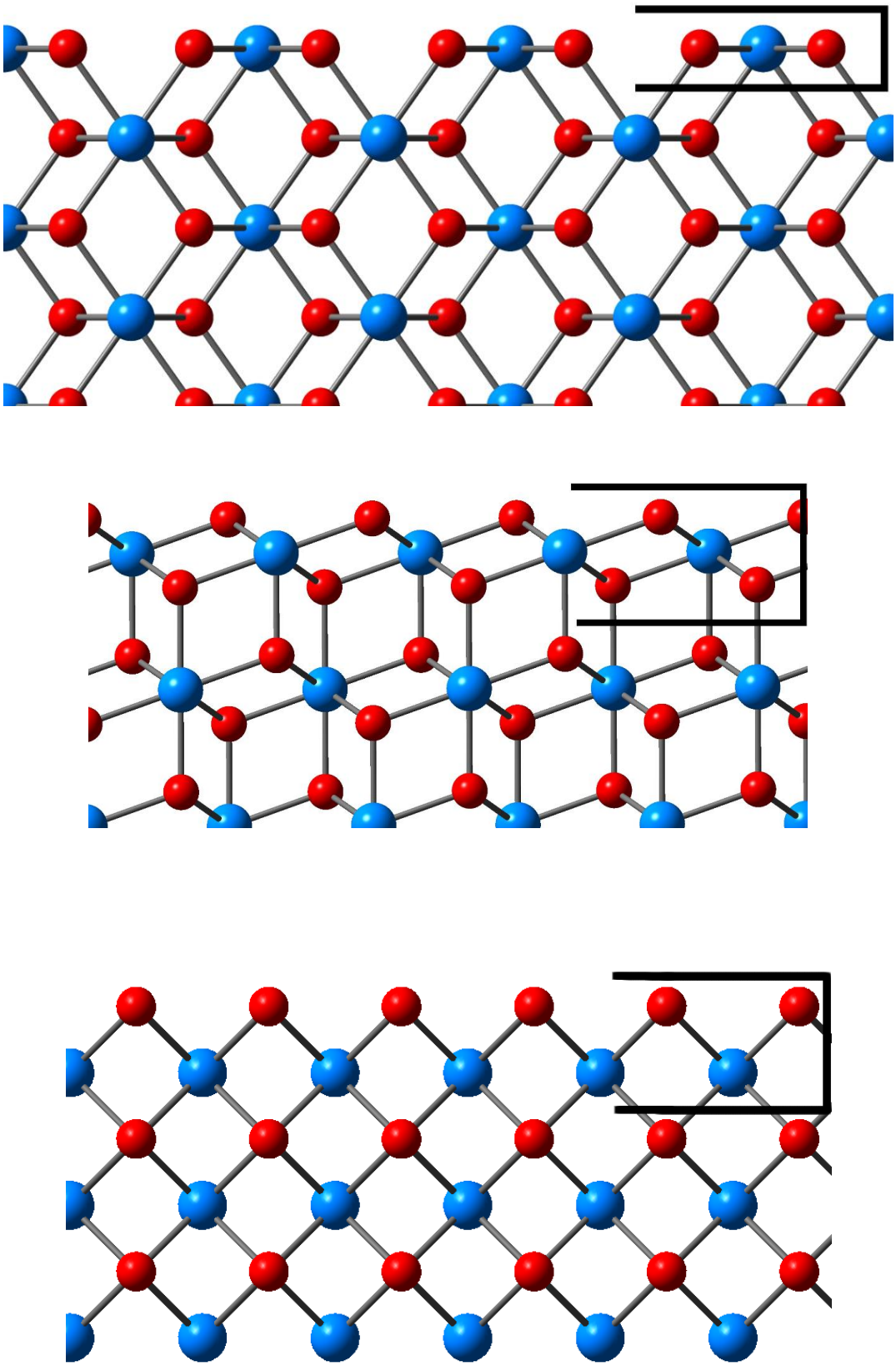

Figure 4.1 (110) type I (top), (111) type II (middle), and (100) type III (bottom) surfaces of AnO_2. Oxygen atoms are shown in red and actinide atoms in blue. Black lines indicate the repeating unit of each surface.

Theoretical studies have shown the stability of these three surfaces to be in the order (111) > (110) > (100).[111,114] The higher stability of the (111) surface is attributed to its high density as well as the higher coordination number of its surface ions. However atomistic[115,116] and DFT+*U*[111] studies have indicated that after becoming fully hydroxylated the order of surface stabilities on UO_2 can reverse to (100) > (110) > (111). Indeed the (100) and (110) are seen to have higher surface reactivities than the (111).

This chapter will focus on the (111) and (110) surfaces, as they are the most stable, and therefore don't undergo large surface reconstructions, which makes them easier to model. Furthermore, most theoretical studies in this area have focused on these two surfaces, so the results obtained here can be compared to those studies.

4.1.2 Experimental Studies of Water Adsorption on UO_2

A significant proportion of experimental work on UO_2 surfaces has investigated whether water adsorbs molecularly or dissociatively. Water is known to adsorb weakly and reversibly on UO_2 (111) single crystal surfaces[117] and thin films,[118] indicating that it adsorbs molecularly. However if the UO_2 surface is sputtered, creating a substoichiometric UO_{2-x} prior to water adsorption, then H_2 desorbs from the surface.[117] Furthermore increasing the amount of time the surface undergoes sputtering, i.e. making a more defective surface, increases the amount of H_2 desorbing. Similarly D_2 desorbs from polycrystalline UO_2 surfaces after temperature programmed desorption (TPD) experiments with D_2O.[119] Hence on substoichiometric or polycrystalline UO_2, which contains many defects, dissociative adsorption of water occurs followed by H_2/D_2 desorption. H_2 desorption is attributed to the adsorbing water molecules healing the defective surface, with oxygen filling the surface vacancies.

4.1.3 Experimental Studies of Water Adsorption on PuO_2

Experimental studies of water adsorption on PuO_2, obtained from various means including interim storage, have shown that water adsorbs *via* a multi-step process with initial strong chemisorption due to dissociation, forming a hydroxylated surface, followed by successive layers of H_2O physisorbed above the

hydroxylated layer.[120] Stakebake found, from a TPD study on PuO_2 prepared from Pu metal, that water desorbed in two temperature ranges, one between 373−423 K, and a second between 573−623 K.[121] It was assumed that the reversible adsorption of water is a non-activated process and so the enthalpy of adsorption is equal to the activation energy of desorption. He attributed the higher temperature desorption to dissociatively adsorbed water forming a hydroxylated layer, estimating an adsorption energy of -2.94 eV, while the lower temperature was thought to be due to molecular water hydrogen bonded to the hydroxyl layer, with an estimated adsorption energy of -0.88 eV. Paffet *et al.* revised these estimations based on a Redhead analysis of the results, estimating adsorption energy values of -1.82 eV for dissociative adsorption and -1.11 eV for water molecularly adsorbing to the hydroxyl layer at 371 K.[79] However as these studies were not performed on single crystal surfaces, the results obtained here will not be directly comparable.

PuO_2 was considered to be the highest oxide of plutonium and therefore stable in water with respect to oxidation. However more recently evidence for the formation of a superstoichiometric PuO_{2+x} has emerged. The formation of higher oxides was first noted in studies of the reaction of Pu metal with water[122,123]. The reaction resulted in a multi-layer oxide forming on the metal, with a layer of Pu_2O_3 adjacent to the metal, followed by a layer of PuO_2, then at the solid-gas interface a layer of PuO_{2+x}, containing Pu(VI). The higher oxide has also been formed in the reaction of PuO_2 with adsorbed water at 25 to 350 ^oC[124]:

$$PuO_2\,(s) + xH_2O\,(ads) \rightarrow PuO_{2+x}\,(s) + xH_2\,(g)$$

PuO_{2+x} can be formed in moist air or moist oxygen with the additional oxygen incorporated into interstitial sites of the fluorite structure. Hence the reaction of PuO_2 with H_2O can lead to the formation of H_2, which could lead to can pressurisation in the storage of plutonium dioxide. However theoretical studies have predicted that the reaction between water and PuO_2 to form PuO_{2+x} is highly endothermic.[125] Still, the presence of water seems to be important in the oxidation of PuO_2; in the presence of atomic oxygen bulk oxidation of PuO_2 does not take place when water is absent, with only a chemisorbed surface layer of oxygen being formed, as identified by UPS[126].

4.1.4 Computational Studies of Water Adsorption on UO_2 and PuO_2

There is a significant amount of literature investigating water adsorption on UO_2 surfaces using computational methods. However, the range of adsorption energies obtained for water on the UO_2 surfaces is substantial, and there is still disagreement upon whether dissociative or molecular adsorption is more energetically favourable.

On the (111) surface Skormurski *et al.*[127] and Weck *et al.*,[128] the former using GGA and the latter GGA+*U*, both found molecular adsorption to be more favourable, with adsorption energies of -0.69 (-0.25 for 1 ML) and -0.8 eV while dissociative adsorption energies were lower with -0.43 (-0.22 for 1 ML) and -0.6 eV respectively, for a coverage of ½ ML, agreeing with the experimental results on UO_2 (111) thin films and single crystal surfaces described above. More recent studies using DFT+*U* have found dissociative adsorption to be more favourable at a low coverage of 0.25 ML, albeit by only 0.02 eV[14] and 0.07 eV[108], with an adsorption energy of 1.12 eV and 0.68 eV respectively. However, at higher coverage a mixture of molecular and dissociative adsorption (Figure 4.2) was found to be the most favourable arrangement, with adsorption energies per molecule of -1.09 eV[14] and -0.65 eV[108] with 1 ML of coverage.

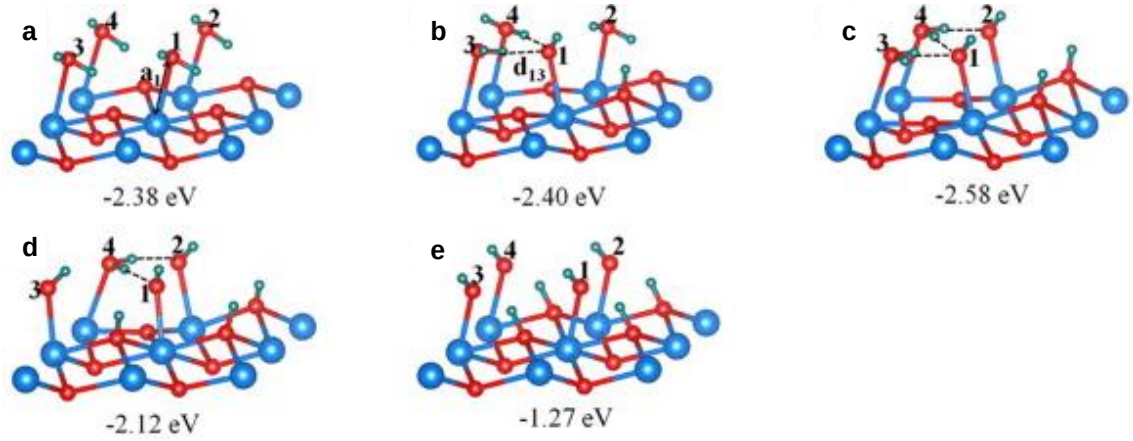

Figure 4.2 Optimized molecular (a), mixed (b–d), and dissociative (e) adsorption structures and energies of four water molecules (1 ML) on the UO_2 (111) surface. The oxygen and hydrogen atoms are plotted in red and green, respectively, while the uranium atoms are blue. The adsorption energies are given for all four molecules. Adapted from reference.[108]

Dissociative adsorption could be energetically more favourable, but not seen experimentally due to an energy barrier for dissociation of an adsorbed water

molecule. Bo *et al.* calculated the reaction pathway for dissociation of molecular water on the (111) surface with the climbing image nudged elastic band method (CI-NEB), with one water molecule in their unit cell (corresponding to a coverage of ¼ ML) they found an energy barrier of only 0.13 eV, concluding that water could readily dissociate to a hydroxyl radical and a hydrogen atom on the UO_2 (111) surface.[129] However, in a separate paper they calculated the dissociation for a monolayer of coverage,[108] the calculation was performed stepwise, with four water molecules in the unit cell they calculated the activation energy going from four water adsorbed molecularly, to three adsorbed molecularly and one dissociatively and so on. The activation energies for each step ranged from 0 to 0.69 eV, indicating at a full coverage there may be a significant barrier to forming a hydroxylated surface.

Other studies have focused on just the hydroxylated surface, calculating dissociative adsorption energies of -0.29 eV[111] and -1.08 eV[130] for 1 ML coverage. Hence for 1 ML of coverage the adsorption energy for dissociative adsorption can range from -0.22 eV[128] to -1.08 eV[130] depending on the study.

Water adsorption on the (110) surface of UO_2 has been less well studied than on the (111) surface. Bo *et al.* found that at a low water coverage (¼ ML) dissociative adsorption was more favourable than molecular adsorption by 0.65 eV, with a dissociative adsorption energy of -1.27 eV.[108]

The molecular adsorption on the (110) surface occurred with the water molecule almost perpendicular to the surface, forming one short hydrogen bond (Figure 4.3), this is different to the molecular adsorption of water found in other studies on the (110) surface of systems with the fluorite structure. In theoretical studies of water adsorption on the (110) surface of CeO_2[131] and PuO_2[132], molecular adsorption occurred with the water molecule parallel to the surface, forming two hydrogen bonds between the water and the surface (Figure 4.3 for adsorption on PuO_2 (110)).

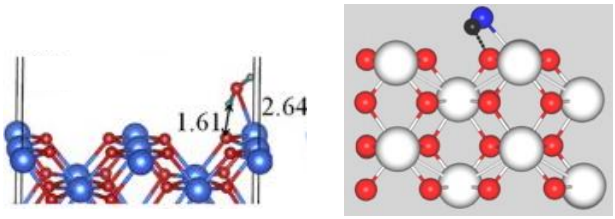

Figure 4.3 Optimized molecular water adsorption structure on the UO_2 (110) surface by Bo *et al.*[108] (left) and the PuO_2 (110) surface by Jomard *et al.*[132] (right). In the left image the oxygen and hydrogen atoms are plotted in red and green, respectively, while the uranium atoms are blue. In the right image the oxygen atom of water is plotted in blue, the oxygen atoms of the PuO_2 surface in red, the hydrogen atoms in black, and the plutonium atoms in white.

At a higher coverage of 1 ML, Bo *et al.* found that the fully hydroxylated surface was still energetically more favourable than the surface covered with water molecules (by 0.16 eV per molecule), however, a mixed case where half the water molecules adsorbed molecularly and half dissociatively was the most stable configuration (0.08 eV per molecule more stable than the fully hydroxylated surface, Figure 4.4). The stability of this mixed adsorption case was explained by the formation of hydrogen bonds between the molecularly adsorbed water and the hydroxyls formed from dissociative adsorption.

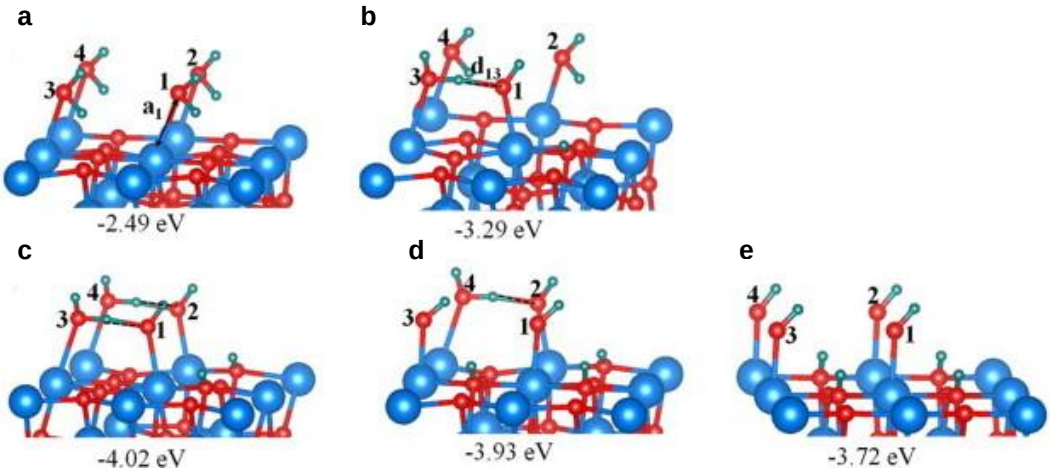

Figure 4.4 Optimized molecular (a), mixed (b–d), and dissociative (e) adsorption structures and energies of four water molecules on the UO_2 (110) surface. The oxygen and hydrogen atoms are plotted in red and green, respectively, while the uranium atoms are blue. The adsorption energies are given for all four molecules. Adapted from reference.[108]

The activation energy for dissociation of a water molecule on the (110) surface was calculated – again with CI-NEB – and found to be barrierless with a single molecule in the unit cell (coverage of ¼ ML).[129] With four molecules in the unit cell (coverage of 1 ML), the activation energies for each step of dissociating one of the four water molecules ranged from 0.06 to 0.54 eV.[108]

Studies which have compared water adsorption on the (111) and (110) surfaces have found that dissociative adsorption is significantly stronger on the (110); 0.76 eV[111] and 0.61 eV[108] stronger on the (110) than the (111) surface for 1 ML. Molecular adsorption was found to have a similar energy between the two surfaces, being only 0.02 eV[108] stronger on the (110) surface.

Although less extensive than the theoretical work on UO_2, there are periodic boundary conditions (PBC) DFT studies on PuO_2, which compare either water adsorption on different actinide dioxide systems,[111,130] or look solely at PuO_2 surfaces.[132,133]

The two studies comparing water adsorption on different actinide systems (UO_2, NpO_2, and PuO_2[111]; and ThO_2, UO_2, and PuO_2[130]) both examine dissociative adsorption forming a fully hydroxylated surface (1 ML). They find dissociative adsorption to be more favourable on UO_2 than PuO_2, by 0.22 eV[130] or 0.06 eV[111] on the (111) surface and 0.08 eV[111] on the (110) surface. Additionally, dissociative adsorption was more stable by 0.74 eV on the (110) than the (111) surface.[111]

The other two theoretical studies[132,133], which focused solely on PuO_2, calculated water adsorption on the (110) surface only, but compared molecular and dissociative adsorption. They both found dissociative adsorption to be more favourable than molecular, by 0.11 eV[133] and 0.16 eV[132] for 1 ML of coverage. For water adsorption on PuO_2, the dissociative adsorption energies range from -0.23 to -0.86 eV on the (111) surface, and from 0.01 to -0.95 eV on the (110) surface, while molecular adsorption energies range from -0.10 to -0.79 eV on the (110) surface.

While two theoretical studies compared water adsorption between UO_2 and PuO_2 surfaces, they considered only dissociative adsorption, and only one of them compared the adsorption across different surface terminations. Therefore there has not been a systematic theoretical study comparing water adsorption between UO_2 and PuO_2 across different surface terminations and with both molecular and dissociative adsorption considered. This would be useful, as has been mentioned previously, experimental work on PuO_2 is difficult, and so if it was known that

water interacts with UO_2 and PuO_2 surfaces in a similar way, then UO_2 could be considered as an analogue for PuO_2.

In this chapter I will study adsorption on both UO_2 and PuO_2, looking at both molecular and dissociative adsorption on the (111) and (110) surfaces. Adsorption geometries and energies will be calculated for 1–4 water molecules on the surfaces, this will aid comparison to previous theoretical studies which have 1–4 adsorption sites in their unit cells (¼–1 ML), as well as being able to investigate whether there are any interactions between water molecules on the surface.

4.2 Computational Details

Calculations in this chapter were performed with the TURBOMOLE 6.5 program using the PBE0 exchange-correlation functional.

The self-consistent field convergence was set to $1x10^{-6}$ a.u. while geometry optimizations were performed with convergence criteria of $1x10^{-6}$ a.u. for the total energy and $1x10^{-3}$ a.u. for the maximum norm of the cartesian energy gradient.

The def-SV(P)[103,104] and MWB-AVDZ[105] basis sets were again used, with the corresponding small and large core PPs, noted from now on as the SV(P) basis set. Larger basis sets were also used: SVP calculations with def-SVP[103,104] and MWB-AVDZ basis sets, TZVP calculations with def-TZVP[104,134] and MWB-AVTZ[105] and QZVP calculations with def-QZVP[104,135]and MWB-AVQZ[105] basis sets.

Again PPs were used for the actinide ions in the quantum mechanically treated cluster; small-core (60 electron) def-PPs from the TURBOMOLE library[106,107] or, where stated, large-core PPs incorporating the 5f electrons.[105]

Dispersion corrections have been included with the Grimme D3 parameters.[21]

The coordinates of ions in the cluster coordinated only to other quantum mechanical ions were optimized. When performing adsorption calculations, the coordinates of the water molecules were additionally allowed to relax. Adsorption

energies, E_{ads}, were calculated using the following equation, with each species being optimized as described above:

$$E_{\mathrm{ads}} = E_{\mathrm{Surf+H_2O(opt)}} - E_{\mathrm{Surf(opt)}} - E_{\mathrm{H_2O(opt)}} \quad (4.1)$$

Negative values of adsorption energies indicate the adsorption of water is stable.

I have calculated the basis set superposition error (BSSE) by the counterpoise correction method; the BSSE energy is calculated using (4.2):

$$BSSE = E_{\mathrm{Surf}}^{\mathrm{Surf+H_2O}} - E_{\mathrm{Surf}}^{\mathrm{Surf}} + E_{\mathrm{H_2O}}^{\mathrm{Surf+H_2O}} - E_{\mathrm{H_2O}}^{\mathrm{H_2O}} \quad (4.2)$$

The energies for the surface and the water molecule in (4.2) are all calculated at their geometries in the presence of each other, i.e. at the optimized geometry of the water molecule on the surface. The basis sets used are shown in superscript, so $E_{\mathrm{Surf}}^{\mathrm{Surf+H_2O}}$, is the energy of the surface calculated without an explicit water molecule but with the basis functions of water. The BSSE is then added onto the adsorbed water calculation, hence (4.1) becomes:

$$E_{\mathrm{ads}}^{\mathrm{CP}} = E_{\mathrm{Surf+H_2O(opt)}} - BSSE - E_{\mathrm{Surf(opt)}} - E_{\mathrm{H_2O(opt)}} \quad (4.3)$$

The BSSE always leads to a reduction in the adsorption energy.

4.3 **Results**

4.3.1 Building the model

For my MRes project I investigated small molecule adsorption with the PEECM on the (110) surface of CeO_2 – which is isostructural to the AnO_2 systems. The study showed that the size of the cluster is important when using PEECM; when a small CeO_2 cluster was used water migrated towards the edge to adsorb. The edge atoms in PEECM clusters have a higher charge and can lead to a larger adsorption energy. Therefore a cluster large enough to avoid these issues without becoming too computationally expensive needs to be used, in that study I found that a $Ce_{24}O_{48}$ cluster was large enough to avoid migration of the water molecule to the edge (which occurred on a $Ce_{12}O_{24}$ cluster).

In my EngD project I started by investigating a single water molecule on the (111) and (110) surfaces of UO_2 and PuO_2. I performed geometry optimization and energy calculations with small clusters, ranging from $An_{10}O_{20}$ to $An_{16}O_{32}$, again the size of the cluster affected the adsorption energy. This was most likely, in part, because the water molecules were adsorbing above actinide ions which were not always fully coordinated by explicit oxygen ions, which, as I'd seen with my study on cerium dioxide, had a big impact on the charge of these cerium or actinide atoms.

From this work I knew that I would have to create clusters where the surface atoms to which the water molecule were adsorbing, whether actinide or oxygen atoms, would have to be coordinated only by other atoms in the explicit cluster region.

After I had performed these initial test calculations on a single water molecule adsorbing, I wanted to investigate multiple water molecules adsorbing onto a cluster to investigate how they interact with each other.

I will discuss how I decided on the particular cluster I used for the (111) surface and (110) surface at the beginning of Sections 4.3.2 and 4.3.3 respectively.

4.3.2 Water Adsorption on the (111) Surface

4.3.2.1 Geometries

As mentioned previously, two recent periodic DFT+*U* studies investigated water in a supercell in which there were four distinct adsorption sites and hence 1-4 water molecules could be adsorbed, which corresponds to ¼ to 1 ML of coverage on the surface.[14,108] To make comparisons between the results here and those from the two studies I decided to create a cluster with four adsorption sites. These adsorption sites are above, or close to, surface actinide ions, I chose these as adsorption sites, as I had seen them with my own calculations on CeO_2 as well as previous studies on both CeO_2[131] and AnO_2[14,108,128] systems. Therefore the clusters I created for the (111) surface were centred on the mid-point between four surface actinide ions, with each actinide ion fully coordinated to explicit oxygen atoms (i.e. 7 coordinate)

I started with a $An_4An_{11}O_{30}$ cluster (Figure 4.5) and performed calculations on 1-4 molecules in orientations similar to those found from the Oppeneer *et al.* paper.[14] This cluster contains four actinide sites which are coordinated by only the inner cluster region; these are the sites where adsorption is considered, the rest of the actinide atoms use 5f-in-core PPs.

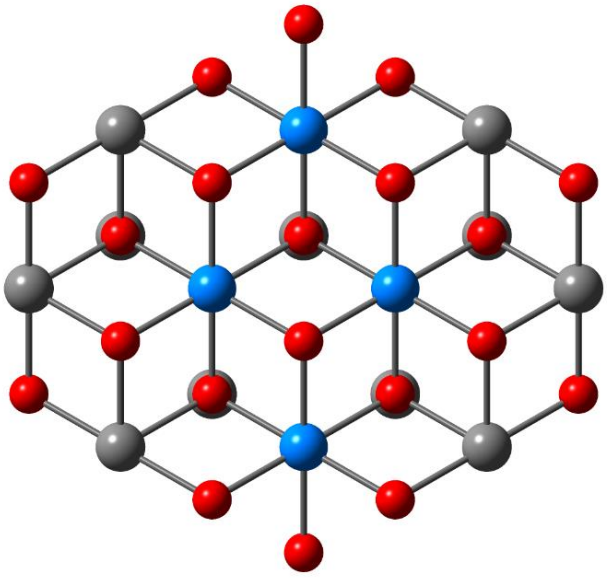

Figure 4.5 $An_4An_{11}O_{30}$ cluster viewed from above. Oxygen atoms are shown in red and actinide atoms in blue and grey. Grey spheres represent actinide atoms treated with 5f-in-core PPs.

I increased the size of the cluster to $An_4An_{15}O_{38}$ (Figure 4.6), now each adsorption site actinide ion had its 6 nearest neighbour actinide ions treated explicitly. Furthermore any surface oxygen atoms, which could bond to adsorbing water molecules, were coordinated to only explicit actinide atoms in the cluster.

The change in the adsorption energy going from the smaller to the larger cluster was small for the adsorption of 1-4 molecules that had been found by Oppeneer et al.[14] (0.00–0.03 eV), although was higher for a single molecular adsorption (0.11 eV). Despite the larger difference for the molecular adsorption the results indicated I had a suitably sized surface. However, I decided to use the larger $An_4An_{15}O_{38}$ cluster for subsequent work, as the computational time for geometry optimizations with this cluster were still feasible, and a larger cluster should give a better representation of the surface.

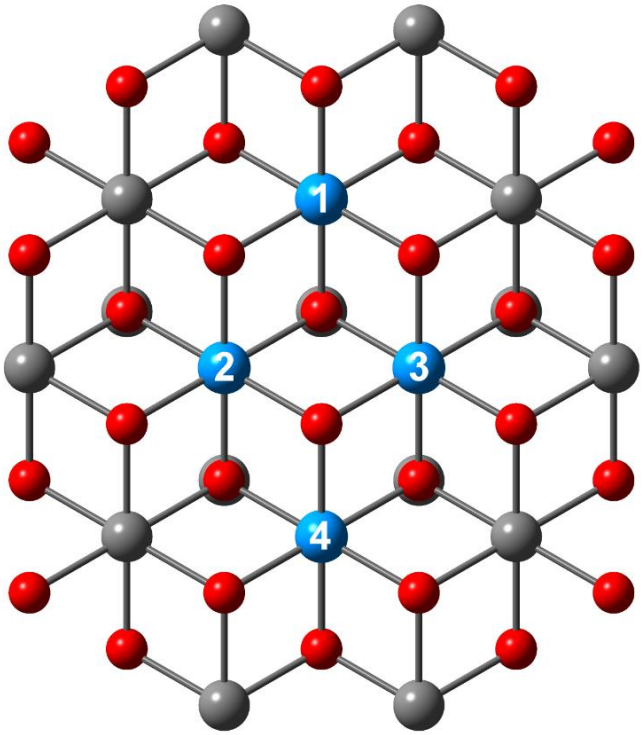

Figure 4.6 $An_4An_{15}O_{38}$ cluster viewed from above. Oxygen atoms are shown in red and actinide atoms in blue and grey. Grey spheres represent actinide atoms treated with 5f-in-core PPs. Embedding ions not shown. Sites where adsorption is considered are labelled 1 to 4.

The $An_4An_{15}O_{38}$ cluster representation of the (111) surface has 3 layers of oxygen atoms (top images in Figure 4.7), the surface layer contains 14 atoms, 8 of which can relax during geometry optimizations; the second layer also contains 14 atoms, 5 of these can relax during geometry optimizations; and the last oxygen layer contains 10 atoms, 2 of which can relax during geometry optimizations. The cluster has a surface layer of 14 actinide atoms, 8 of these are allowed to relax during geometry optimizations and one subsurface layer of 5 actinide atoms, all of which are held fixed during geometry optimizations.

Water can adsorb onto AnO_2 surfaces in two ways: molecularly, where the water molecule remains intact on adsorption, or dissociatively, where an O-H bond is heterolytically broken. Molecular adsorption on the (111) surface occurs with an oxygen adsorbing above an actinide ion and two hydrogen atoms pointing towards two surface oxygen atoms. Dissociative adsorption forms two hydroxyl groups: the first formed from a hydrogen of the water molecule binding to a surface oxygen, which will be referred to as the surface hydroxyl, and a second in which an OH group of water adsorbs above an actinide ion, which will be referred to as the adsorbed hydroxyl. These adsorptions, at site 1, are shown in

Figure 4.7. The oxygen atom in a water molecule will be referred to as O_W, oxygen in an adsorbed hydroxyl O_{OH} and oxygen at the surface O_S.

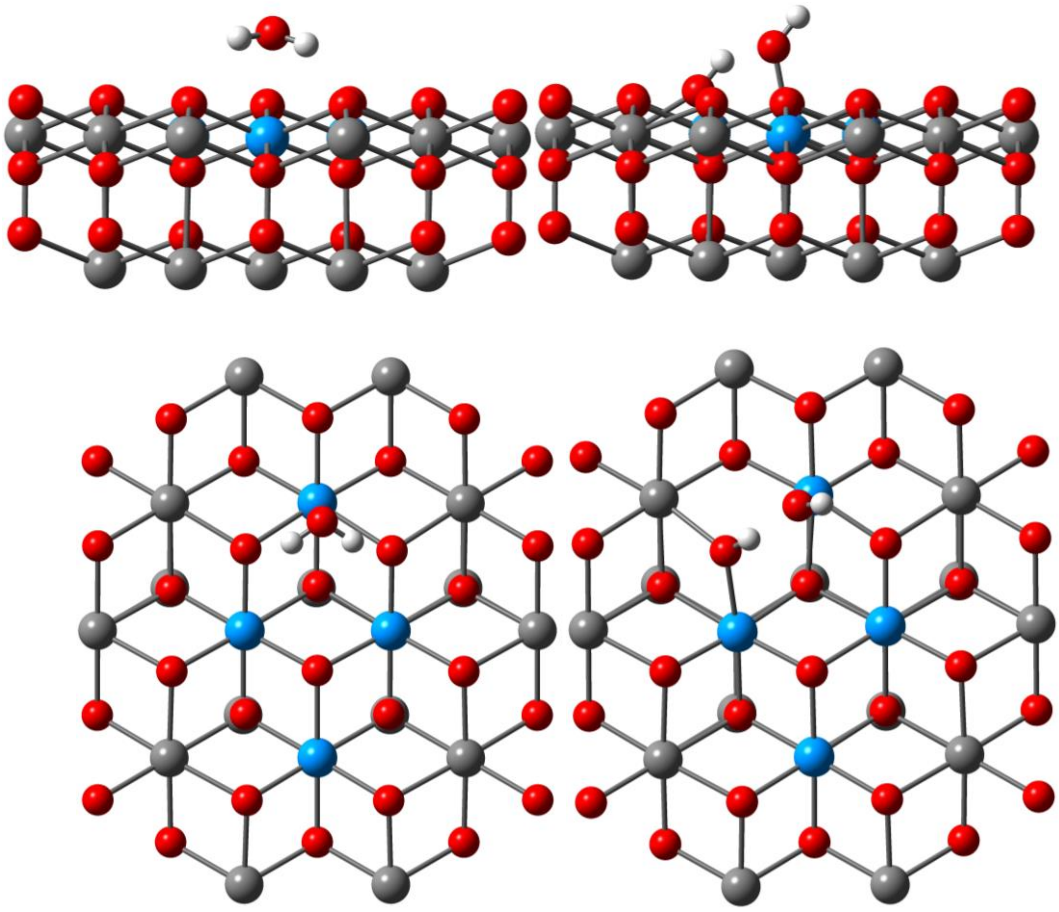

Figure 4.7 Molecular (left) and dissociative (right) adsorption of a single water molecule on the (111) surface of a $U_4U_{15}O_{38}$ cluster. Top view shows the cluster in the plane of the surface, while the bottom view is from above the surface. Hydrogen atoms are shown in white, oxygen atoms in red and uranium atoms in blue and grey. Grey spheres represent uranium atoms treated with 5f-in-core PPs. Embedding ions not shown.

Molecular adsorption occurs with the oxygen of the water molecule above a surface uranium atom at an empty oxygen site, restoring the coordination of the surface uranium to 8. The U-O_W distance for molecular adsorption is 2.57 Å, 0.20 Å longer than the bulk UO_2 value of U-O (2.37 Å) and it lies between recently calculated distances of 2.48 Å[14] and 2.60 Å.[108] The H-O_S distance is 1.76 Å, slightly longer than previously calculated values of 1.72 Å[14] and 1.61 Å.[108] This short H-O_S distance shows that a hydrogen bond is formed between a hydrogen

of the water molecule and an oxygen surface atom. The second H-O_S distance is longer at 1.99 Å, showing that two hydrogen bonds are formed with the surface.

For dissociative adsorption the hydrogen of the surface hydroxyl points towards the oxygen of the adsorbed hydroxyl (Figure 4.7), with a distance of 1.58 Å; hence there is a short hydrogen bond between the two OH species. Recent theoretical studies calculated H-OH distances of 1.45 Å[14] and 1.66 Å[108] on the UO_2 surface. The U-O_{OH} distance is 2.21 Å and agrees very well with recent theoretical studies which both calculated a distance of 2.23 Å[14,108] and 2.24 Å[111]. The U-O_{OH} is relatively short, 0.16 Å shorter than the experimental U-O bond length in bulk UO_2, and 0.36 Å shorter than for molecular adsorption.

In order to see the effect of the 5f-in-core PPs on the geometries obtained, I optimized the geometries of one water molecule adsorbing either molecularly or dissociatively on the $U_{19}O_{38}$ cluster (where no 5f-in-core PPs are used). The geometries of the water/surface interactions are affected very little; the U-O_{OH} bond for dissociative adsorption differs by only 0.02 Å. Therefore all geometry optimizations were performed on the $U_4U_{15}O_{38}$ cluster, in order to speed up the calculation time.

Multiple water molecules adsorb in a broadly similar way to single molecules. However, for two water molecules adsorbing, one molecularly and one dissociatively (Figure 4.8), the H-O distance between the hydrogen of the adsorbed water molecule and the oxygen of the adsorbed hydroxyl species is 1.81 Å, suggesting a hydrogen bond is formed between the two adsorbates. This hydrogen bonding, between a molecularly adsorbed and dissociatively adsorbed water molecule, then occurs for all cases of mixed adsorption when there are 3 or 4 water molecules adsorbing on the cluster. The hydrogen bond lengths range from 1.69–1.81 Å.

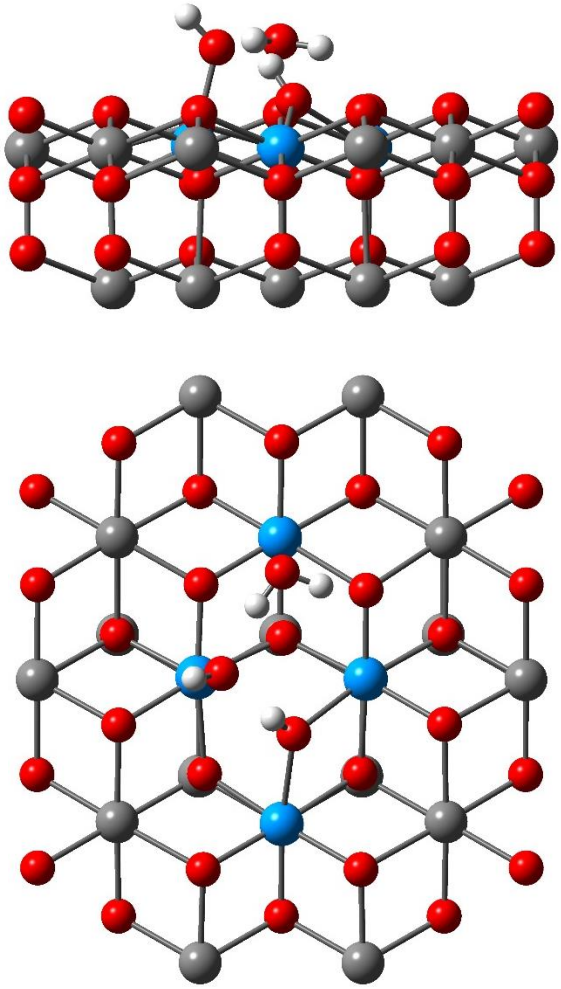

Figure 4.8 Mixed (1m,1d) molecular and dissociative adsorption of two water molecules on the (111) surface of a $U_4U_{15}O_{38}$ cluster. Top view shows the cluster in the plane of the surface, while the bottom view is from above the surface. Hydrogen atoms are shown in white, oxygen atoms in red and uranium atoms in blue and grey. Grey spheres represent uranium atoms treated with 5f-in-core PPs. Embedding ions not shown.

Water adsorbs on the PuO_2 (111) surface in a similar way to the UO_2. For molecular adsorption the Pu-O_W distance is 2.50 Å, 0.07 Å shorter than the U-O_W distance, in agreement with the smaller ionic radius of Pu^{4+} *vs* U^{4+}, 0.96 Å and 1.00 Å respectively.[2]

For dissociative adsorption the H-OH distance between the two hydroxyl species is 1.59 Å, only 0.01 Å longer than on the UO_2 surface, and the Pu-O_{OH} distance is 2.20 Å, 0.01 Å shorter than the U-O_{OH} distance. This is slightly shorter than the length calculated by Rák *et al.* of 2.22 Å[111], however they also calculated the Pu-O_{OH} length to be shorter than the U-O_{OH} length, by 0.02 Å.

4.3.2.2 Energies

The size of the basis set can often have an effect on the adsorption energy, with more sophisticated (larger) basis sets providing in principle better energies. To test the effect of basis set size on this model I performed single point energy calculations of (1m), (1d), and (1m,1d) adsorption configurations with increasing basis set size at their SV(P) optimized geometries; the results are collected in Table 4.1. The geometry optimisations and energies were obtained with the $U_4U_{15}O_{38}$ cluster, i.e. where fifteen uranium atoms use the large-core PP.

Basis Set	**Adsorption energies/ eV**		
	(1m)	(1d)	(1m,1d)
SV(P)	-1.04	-1.08	-1.19
SVP	-0.95	-0.88	-1.09
TZVP	-0.62	-0.70	-0.82
QZVP	-0.46	-0.65	-0.69

Table 4.1 Energies of (1m), (1d) and (1m,1d) adsorption configurations of water on the $U_4U_{15}O_{38}$ cluster calculated at the SV(P) optimized geometry with increasing basis set size. Adsorption energy shown is per water molecule.

It can be seen from Table 4.1 that the adsorption energy has a clear dependence on the size of the basis set used. As the size of the basis set increases the adsorption energy decreases, with a difference of up to 0.58 eV between the SV(P) and QZVP basis sets. In addition the adsorption energy does not converge with respect to basis set size, even when the QZVP basis set is used. The adsorption energies obtained with the QZVP basis set should be considered the best estimate. It should be noted that although the TURBOMOLE basis set library provides valence basis sets for the actinides from the SV(P) level up to QZVP, in fact the same basis, the QZVP, is used at each level. Hence only the oxygen and hydrogen basis sets change from the SV(P) calculations to the QZVP, and thus the decreasing adsorption energies in Table 4.1 are obtained from increasingly well-balanced basis sets.

Two recent theoretical studies using PBC DFT calculated adsorption energies for (1m) of -1.10 eV[14] and -0.60 to -0.61 eV (dependent on unit cell size),[108] while (1d) adsorption was calculated to be stronger at -1.12 eV[14] and -0.68 to -0.77 eV.[108] The (1m,1d) adsorption was calculated with adsorption energies of -1.23

eV[14] and -0.65 to -0.76 eV.[108] Hence the energies obtained with the smallest basis set (SV(P)) are in good agreement with those of the LDA+*U* study[14] while the energies obtained with the highest-quality QZVP basis set are closer to those from the PBE+*U* study.[108] The LDA exchange-correlation functional is known often to overestimate binding energies, and indeed the results of the previous LDA study are in close agreement with the adsorption energies calculated with the lowest-quality basis set here.

The effect of basis set size on the adsorption geometries was also explored. As calculations with the larger basis sets are very expensive it was hoped that, as I have done when producing the data in Table 4.1, geometry optimizations could be performed with the SV(P) basis set, with subsequent single point energy calculations performed at a higher quality basis set. The change in adsorption energy when optimizing the geometry with the SVP and TZVP basis sets is shown in Table 4.2, given as the difference between single point calculations on the SV(P) optimized structures with the higher basis set and the higher basis set optimized structure with the higher basis set. Geometry optimizations with the QZVP basis set are prohibitively expensive and were not performed.

Basis Sets	**Adsorption Energy/ eV**		
	(1m)	(1d)	(1m,1d)
SVP	-0.04	-0.10	-0.03
TZVP	-0.03	-0.01	-0.02

Table 4.2 Change in adsorption energy as a function of basis set for water on the $U_4U_{15}O_{38}$ cluster representation of the (111) surface of UO_2. Adsorption energy shown is per water molecule.

The changes in adsorption energy when the geometries are re-optimized at the higher basis set are small, with the only significant difference at the SVP level for the (1d) adsorption, which at the TZVP level again has a very small difference to the SV(P) level.

The changes in geometric parameters when optimizing the geometry with the SVP and TZVP basis sets, compared to the SV(P), are shown in Table 4.3 for the U-O_{water} bond lengths and Table 4.4 for the bond angles.

Basis sets	(1m)	(1d)	(1m,1d)	
SVP	0.009	-0.013	-0.009	0.043
TZVP	0.030	-0.016	0.000	-0.024

Table 4.3 Change in U-O_{water} bond lengths (Å) as a function of basis set for water on the $U_4U_{15}O_{38}$ cluster representation of the (111) surface of UO_2.

Basis sets	(1m)	(1d)	(1m,1d)	
	<H-O-H	<U-O-H	<H-O-H	<U-O-H
SVP	-1.63	2.96	-1.783	-0.975
TZVP	-0.83	2.99	-0.656	1.749

Table 4.4 Change in bond angles (°) as a function of basis set for water on the $U_4U_{15}O_{38}$ cluster representation of the (111) surface of UO_2.

Clearly, the changes in the bond lengths and bond angles are modest when optimizing the structure with a higher basis set.

In order to see if the significant adsorption energy differences arise as a function of basis set superposition error (BSSE) due to the imbalance between the relatively large basis set on the actinide ions and the smaller basis set on the oxygen and hydrogen atoms, I calculated adsorption energies including the counterpoise correction (CP) at the SV(P) level. The counterpoise correction calculations are, computationally, significantly less expensive than the QZVP calculations.

Table 4.5 shows the adsorption energies for 1-4 water molecules on the $U_{19}O_{38}$ cluster, with the small SV(P) basis set, the large QZVP basis set and the small basis set with the counterpoise correction to account for the basis set superposition error. This allows comparison between the large basis set and the small basis set with the counterpoise correction, which is, computationally, significantly cheaper. I also include the energies calculated with the SV(P) basis set, counterpoise correction, and the Grimme D3 dispersion parameters, to see the effect of dispersion on the adsorption energies. Geometry optimisations were performed with the $U_4U_{15}O_{38}$ cluster, i.e. fifteen uranium atoms have the large-core PP, and then single point energy calculations were performed with the $U_{19}O_{38}$ cluster, where all uranium atoms have the small-core PP.

Site	Type	SV(P)	QZVP	SV(P) + CP	SV(P) + CP + D3
1	1m	-1.06	-0.58	-0.52	-0.70
	1d	-1.24	-0.84	-0.63	-0.81
1,2	2m	-	-	-	-
	1m,1d	-1.24	-0.77	-0.78	-0.97
	2d	-1.12	-0.65	-0.56	-0.74
1,2,3	3m	-1.10	-0.61	-0.64	-0.83
	2m,1d	-1.22	-0.69	-0.76	-0.95
	1m,2d	-1.17	-0.65	-0.68	-0.87
	3d	-1.07	-0.57	-0.53	-0.72
1,2,3,4	4m	-	-	-	-
	3m,1d	-1.19	-0.69	-0.71	-0.91
	2m,2d	-1.21	-0.70	-0.74	-0.94
	1m,3d	-1.15	-0.62	-0.68	-0.87
	4d	-	-	-	-

Table 4.5 Adsorption energies (eV) per molecule of water on a $U_{19}O_{38}$ cluster representation of the (111) surface of UO_2 within the PEECM. Type of adsorption is denoted by m for molecular or d for dissociative. The adsorption sites (see Figure 4.6) are given in the first column.

The energies calculated at the QZVP and the SV(P) + CP levels are in good agreement with each other, the difference between the two being less than 0.1 eV in all systems, except for the case of one water molecule adsorbing dissociatively where the energies differ by 0.21 eV.

In all cases with one water molecule, dissociative adsorption is more favourable than molecular. However, for two or more water molecules adsorbing a mixture of molecular and dissociative adsorption is favourable on UO_2. This is in agreement with the two recent theoretical studies mentioned above, which found dissociative adsorption to be more favourable at low coverage while a mixture of molecular and dissociative adsorption is most favourable at higher coverage.[14,108] This stabilisation of mixed adsorption over purely molecular or purely dissociative is likely due to the hydrogen bonding that occurs between molecularly and dissociatively adsorbed waters on the cluster.

The inclusion of the D3 dispersion corrections increases the adsorption energies by 0.18–0.20 eV, without changing the ordering in any of the energies obtained. It should be noted that the two previous DFT+*U* studies,[14,108] with which the energies here are compared, did not include dispersion effects.

Given the similarity of the QZVP and SV(P) + CP data to one another (and to the PBE+*U* results of Bo *et al.*[108]), and the much smaller computational cost of the CP calculations, I have used this approach throughout the rest of the study.

Table 4.6 presents data for water adsorbing on the (111) surface of PuO_2. For one water molecule, molecular adsorption is more favourable than dissociative by 0.08 eV, in contrast to UO_2, for which dissociative adsorption is more favourable.

For more than one water molecule, the all molecular cases are always more favourable than the all dissociative. However, as with UO_2, for two or more water molecules adsorbing a mixture of molecular and dissociative adsorption is most favourable on PuO_2. Again this stabilisation of mixed adsorption is likely due to the hydrogen bonding that occurs between molecularly and dissociatively adsorbed water on the cluster.

Site	Type	SV(P) + CP	SV(P) + CP + D3
1	1m	-0.53	-0.77
	1d	-0.45	-0.68
1,2	2m	-0.52	-0.75
	1m,1d	-0.74	-0.99
	2d	-0.39	-0.63
1,2,3	3m	-0.53	-0.77
	2m,1d	-0.66	-0.90
	1m,2d	-0.62	-0.88
	3d	-0.42	-0.66
1,2,3,4	4m	-0.59	-0.83
	3m,1d	-0.55	-0.79
	2m,2d	-0.65	-0.90
	1m,3d	-0.55	-0.80
	4d	-0.32	-0.56

Table 4.6 Adsorption energies (eV) per molecule of water on the (111) surface of PuO_2 modelled as a $Pu_{19}O_{38}$ cluster for SV(P) + CP within the PEECM. Type of adsorption is denoted by m for molecular or d for dissociative. The adsorption sites (Figure 4.6) are given in the first column.

The inclusion of the D3 dispersion contributions causes an increase in the adsorption energy of 0.23–0.25 eV, a slightly larger effect than seen on the UO_2 surface. The larger effect of the D3 dispersion contributions on PuO_2 than UO_2 is

likely due to the smaller lattice parameter of PuO_2, as well as the shorter distances between the water molecules and the PuO_2 surface.

Without D3, analogous adsorption energies are all larger on the UO_2 than PuO_2 surface, in agreement with previous theoretical studies which examined dissociative water adsorption on the (111) surface of AnO_2.[111,130] Some of the analogous adsorption energies are higher on PuO_2 than UO_2 when D3 is included (for 2 water molecules (1m,1d) and for 3 water molecules (1m,2d)), however generally the adsorption energies are still higher on UO_2.

Charges, obtained from natural population analysis, of atoms in the water molecule, and on the surface and bonded to the water molecule, have been calculated at the SV(P) level and are shown in Table 4.7. The partial charges differ by 0.10 a.u. or less between the two systems, with the charge on plutonium being slightly greater than the charge on uranium for both molecular and dissociative adsorption. However, these data suggest that the different adsorption energies are unlikely to be due to differences in ionic bonding.

Type of absorption	Atom	Natural charges/ a.u.	
		UO_2	PuO_2
1m	O_{water}	-0.87	-0.88
	H	0.51	0.51
	H	0.52	0.51
	An	1.23	1.33
1d	$O_{ads\ OH}$	-0.96	-0.94
	$H_{ads\ OH}$	0.49	0.49
	$O_{surf\ OH}$	-0.91	-0.94
	$H_{surf\ OH}$	0.54	0.54
	An	1.31	1.38

Table 4.7 Natural charges on key atoms in the $An_{19}O_{38}$ cluster representation of the AnO_2 (111) surface for adsorption of a single water molecule either molecularly or dissociatively. Type of adsorption is denoted by m for molecular or d for dissociative.

As has been mentioned previously, the ionic radius of 8 coordinate Pu(IV) is smaller than that of U(IV) by 0.04 Å, therefore we would expect the Pu-O bonds involving the actinide and adsorbed species should be shorter than the same U-O bonds. This is the case for molecular adsorption, with the Pu-O_W bond 0.07 Å shorter than the U-O_W bond and the similar adsorption energies between the two

AnO_2 systems. However, for dissociative adsorption the Pu-O_{OH} bond is only 0.01 Å shorter than the U-O_{OH} bond, this corresponds to a weaker dissociative adsorption energy on PuO_2 than UO_2.

4.3.3 Water Adsorption on the (110) Surface

4.3.3.1 Geometries

The adsorption of one to four water molecules was investigated on an $An_4An_{21}O_{50}$ cluster representation of the (110) surface (Figure 4.9) to obtain adsorption geometries and energies, with different ratios of molecular and dissociative adsorption. Water adsorption is considered at 4 actinide sites, where the actinide is coordinated by only the inner cluster region. As with the (111) surface, these 4 actinide atoms have their 5f electrons treated explicitly, while the rest of the actinide atoms use 5f-in-core PPs.

I decided to use a slightly larger cluster than the (111) surface, as I wanted the actinide ions to the left and the right of the cluster to be fully coordinated. This is because when I performed water adsorption calculations on CeO_2 with similar clusters, and these edge atoms were not fully coordinated, the water molecule migrated to these edge sites upon geometry optimization.

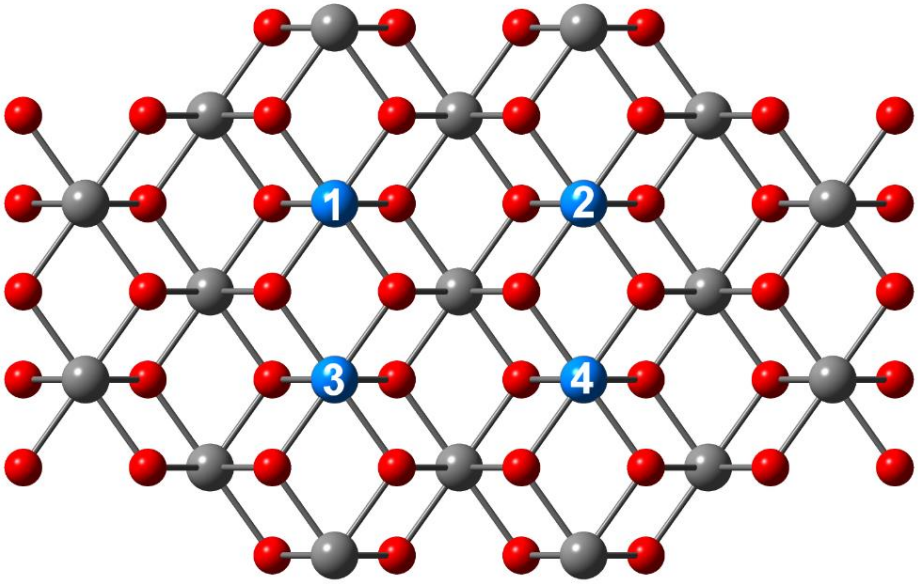

Figure 4.9 $An_4An_{21}O_{50}$ cluster viewed from above the (110) surface. Oxygen atoms are shown in red and actinide atoms in blue and grey. Grey spheres represent actinide atoms treated with 5f-in-core PPs. Embedding ions not shown. Sites where adsorption is considered are labelled 1 to 4.

The $An_4An_{21}O_{50}$ cluster has three layers of both actinide and oxygen atoms (Figure 4.10). The 1st layer contains 12 actinide atoms, 8 of which are allowed to relax during geometry optimizations, and 24 oxygen atoms, 14 of which are allowed to relax during geometry optimizations. The 2nd layer has 9 actinide atoms, 1 of which is allowed to relax during geometry optimizations, and 24 oxygen atoms, 8 of which are allowed to relax. The 3rd layer has 4 actinide atoms and 2 oxygen atoms, which are all fixed during geometry optimizations.

There are two types of adsorption on the (110) surface, as on the (111), molecular and dissociative. Molecular adsorption occurs with the hydrogen atoms tilted towards the surface, the oxygen atom is now not directly above the actinide ion, as on the (111) surface, but lies in the position of one of the two empty oxygen sites at each surface actinide atom (Figure 4.10). This increases the coordination of the surface actinide from 6 to 7.

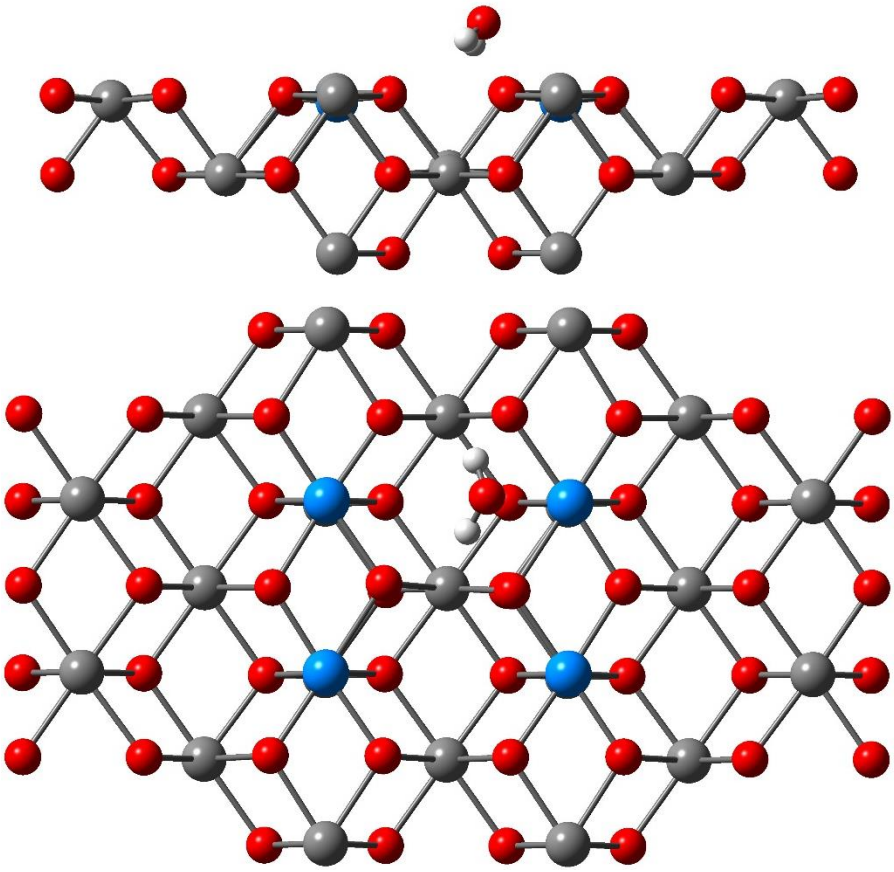

Figure 4.10 Molecular adsorption of a single water molecule on the (110) surface of a $U_4U_{21}O_{50}$ cluster. Top view shows the cluster in the plane of the surface, while the bottom view from above the surface. Hydrogen atoms are shown in white, oxygen atoms in red and actinide atoms in blue and grey. Grey spheres represent actinide ions treated with 5f-in-core PPs.

For the adsorption of one water molecule on UO_2 (110), the U-O_W distance for molecular adsorption is 2.65 Å, 0.09 Å longer than on the (111) surface. The H-O_S distances are 1.78 Å and 2.13 Å forming a shorter and longer hydrogen bond between the adsorbed water and the surface oxygens, the shorter bond being only 0.02 Å longer than on the (111) surface.

Bo *et al.* found a water molecule adsorbing almost perpendicular to the UO_2 (110) surface (Figure 4.3), with U-O_W and H-O_S distances of 2.64 Å and 1.61 Å respectively[108]; the U-O_W value is only 0.01 Å different from that calculated here, however the H-O_S distance here is 0.17 Å longer. Furthermore, the molecular adsorption found by Bo *et al.* had only one hydrogen bond with the surface, where the water has two hydrogen bonds in this study. The orientation of the water molecule to the surface in that study is very different to that found here, the water in this study adsorbs parallel to the surface, as found in studies on CeO_2[131] and PuO_2[132] (110) surfaces (Figure 4.3).

For comparison I optimized the geometry of a water molecule starting in the orientation found in the Bo *et al.* paper[108], the optimized geometry is shown in Figure 4.11. The U-O_W and H-O_S distances are 2.58 Å and 1.45 Å respectively, hence both significantly shorter than found by Bo *et al.*,[108] by 0.06 Å and 0.16 Å respectively. The second H-O_S distance is 2.65 Å, hence only one hydrogen bond is formed between the water molecule and the surface, compared to my initial molecule adsorption orientation, where two hydrogen bonds were formed (albeit with one longer one at 2.13 Å). This difference in geometry could have an effect on the energies, which I will discuss in Section 4.3.3.2.

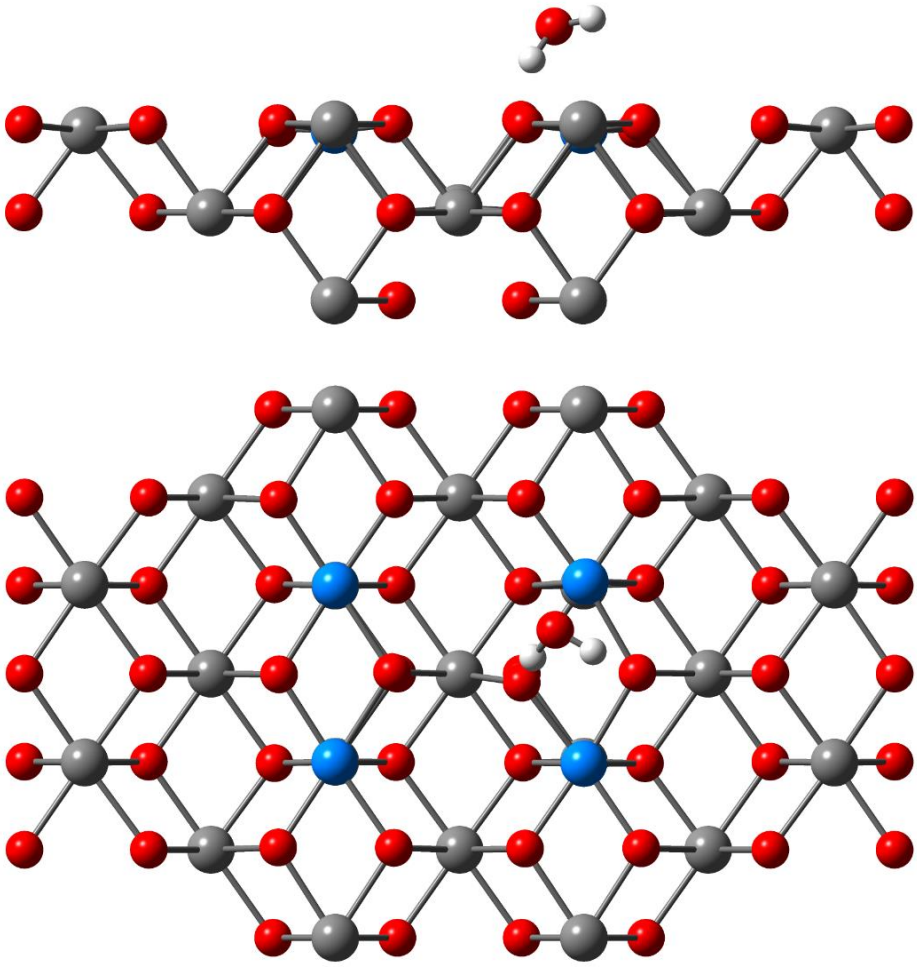

Figure 4.11 Molecular adsorption of a single water molecule in similar orientation to that from a paper by Bo *et al.*[108] on the (110) surface of a $U_4U_{21}O_{50}$ cluster. Top view shows the cluster in the plane of the surface, while the bottom view is from above the surface. Hydrogen atoms are shown in white, oxygen atoms in red and actinide atoms in blue and grey. Grey spheres represent actinide ions treated with 5f-in-core PPs.

Dissociative adsorption again forms two hydroxyl groups, the adsorbed hydroxyl has its oxygen above the actinide ion and its hydrogen tilted towards a surface oxygen, while the surface hydroxyl has its hydrogen angled towards another surface oxygen ion (Figure 4.12).

For the single dissociative adsorption the U-O_{OH} distance is 2.17 Å, 0.04 Å shorter than on the (111) surface, and 0.20 Å shorter than the bulk UO_2 U-O bond length. The H-O_S distance is 0.98 Å, 0.03 Å shorter than on the (111) surface. The bond distances calculated by Bo *et al.* for dissociative adsorption are in both cases identical to the ones calculated here.[108]

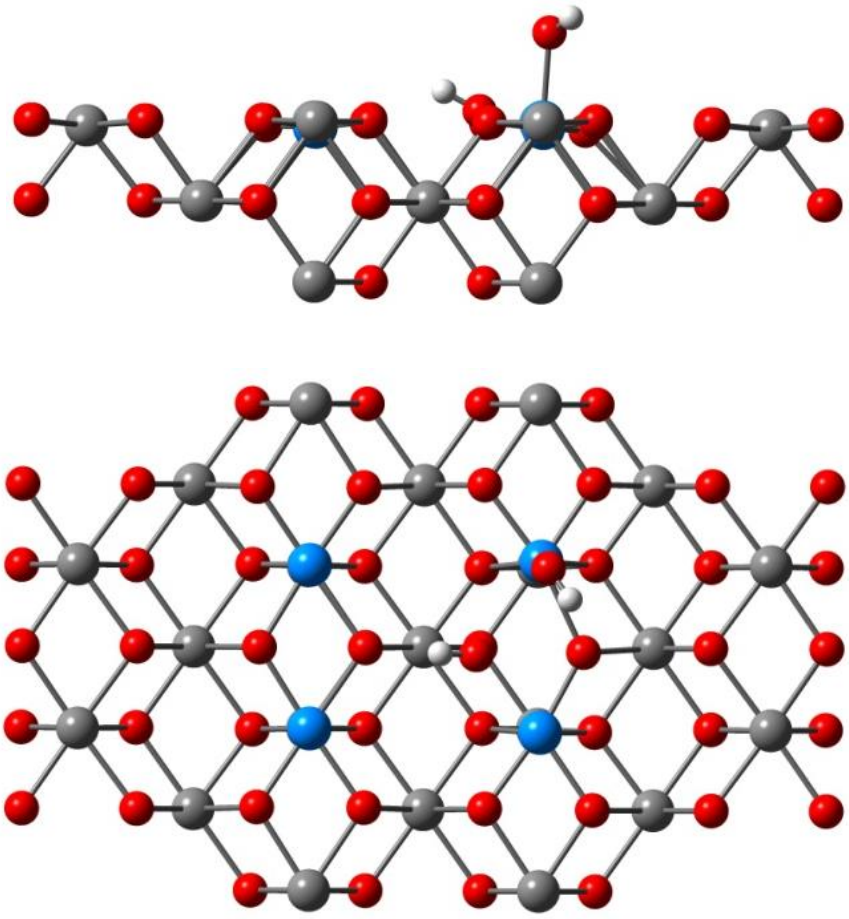

Figure 4.12 Dissociative adsorption of a single water molecule on the (110) surface of a $U_4U_{21}O_{50}$ cluster. Top view shows the cluster in the plane of the surface, while the bottom view is from above the surface. Hydrogen atoms are shown in white, oxygen atoms in red and actinide atoms in blue and grey. Grey spheres represent actinide ions treated with 5f-in-core PPs.

The Pu-O_W distance for one water molecule adsorbing molecularly on the (110) surface is 2.54 Å, 0.10 Å shorter than the U-O_W distance on the (110) surface. This distance is longer than on the PuO_2 (111) surface, by 0.04 Å. The H-O_S length is shorter on the PuO_2 (110) surface than the UO_2 (110) surface at 1.73 Å.

For dissociative adsorption the Pu-O_{OH} distance is 2.14 Å, 0.03 Å shorter than the U-O_{OH} distance, in agreement with the difference in the metals' ionic radii. Ràk *et al.* calculated a Pu-O_{OH} distance of 2.12 Å,[111] in good agreement with the value calculated here; their Pu-O_{OH} is 0.03 Å shorter than their U-O_{OH} distance, which is also found here. This Pu-O_{OH} distance is 0.06 Å shorter than on the (111) surface.

4.3.3.2 Energies

Adsorption energies were calculated for different ratios of molecular and dissociative adsorption on the UO_2 (110) surface at the SV(P) + CP level on the $U_{25}O_{50}$ cluster, with the geometries obtained at the SV(P) level on the $U_4U_{21}O_{50}$ cluster, and are shown in Table 4.8, together with data including the D3 dispersion parameters.

Site	Type	SV(P) + CP	SV(P) + CP + D3
2	1m	-1.06	-1.29
	1d	-1.60	-1.77
1,4	2m	-0.96	-1.20
	1m,1d	-1.29	-1.47
	2d	-1.55	-1.70
1,2,4	3m	-0.97	-1.20
	2m,1d	-1.22	-1.41
	1m,2d	-1.16	-1.34
	3d	-1.54	-1.71
1,2,3,4	4m	-0.90	-1.17
	3m,1d	-1.02	-1.24
	2m,2d	-1.18	-1.39
	1m,3d	-1.27	-1.45
	4d	-1.34	-1.52

Table 4.8 Adsorption energies (eV) per water molecule on the (110) surface of UO_2 modelled as a $U_{25}O_{50}$ cluster within the PEECM. Type of adsorption is denoted by m for molecular or d for dissociative. The adsorption sites (Figure 4.9) are given in the first column.

For one water molecule, dissociative adsorption is significantly more favourable (by 0.54 eV) than molecular. Bo *et al.* calculated a dissociative adsorption energy of -1.27 eV, 0.33 eV smaller than the value calculated here with SV(P) + CP. They also predict dissociative adsorption to be more favourable, calculating an energy for molecular adsorption of -0.62 eV, 0.44 eV smaller than the value in this study.[108] This preference for dissociative adsorption also holds as we increase the number of water molecules; in each case dissociated water is most favourable.

Not shown in Table 4.8 is the adsorption energy for a single water molecule adsorbing in the perpendicular orientation seen in Figure 4.11. The adsorption energy for this molecule is -1.02 eV, hence only 0.04 eV different from the value calculated for the parallel molecular adsorption seen in Figure 4.10, and still 0.40 eV larger than that found by Bo *et al.*[108] The different molecular adsorption orientations between the two studies therefore does not explain the energy difference between the two studies. It should be noted that for the orientation seen in Figure 4.11, I calculated shorter U-O_w and H-O_s distances, which could partially explain the 0.40 eV difference between mine and their results in adsorption energy for the perpendicular orientation. However, there is still a difference of 0.33 eV in the dissociative adsorption energy, where the key bond distances are the same between the two studies.

The larger adsorption energies in this study for the (110) surface could be because with the PEECM it is not possible to perform a full surface relaxation, only atoms in the centre of the cluster can be optimized. If the surface is not fully relaxed this could cause increased adsorption energies. This would have less of an effect on the (111) surface, which is more stable and hence undergoes surface reconstructions to a lesser extent. This could explain the greater differences in the energies obtained in this study to those of Bo *et al.* for the (110) surface than the (111) surface.

Table 4.9 presents analogous data for PuO_2. On the (110) PuO_2 surface, as on the (110) UO_2, dissociative adsorption is more favourable than molecular adsorption; with four water molecules the difference is 0.23 eV between all molecular or all dissociative adsorption. A preference for dissociative adsorption

was also concluded from experimental studies of water adsorption on PuO_2, and the dissociative adsorption energy was estimated to be -1.82 eV[79]. This is 0.60 eV larger than the SV(P) + CP data in this study for four adsorbing water molecules, though the inclusion of dispersion corrections reduces the difference between experiment and theory to only 0.36 eV.

Site	Type	SV(P) + CP	SV(P) + CP + D3
2	1m	-0.94	-1.25
	1d	-1.34	-1.58
1,4	2m	-1.03	-1.37
	1m,1d	-1.13	-1.39
	2d	-1.28	-1.51
1,2,4	3m	-1.00	-1.32
	2m,1d	-1.12	-1.39
	1m,2d	-1.17	-1.41
	3d	-1.22	-1.45
1,2,3,4	4m	-0.99	-1.32
	3m,1d	-1.08	-1.37
	2m,2d	-1.16	-1.43
	1m,3d	-1.13	-1.37
	4d	-1.22	-1.46

Table 4.9 Adsorption energies (eV) per water molecule adsorption on the (110) surface of PuO_2 modelled as a $Pu_{25}O_{50}$ cluster within the PEECM. Type of adsorption is denoted by m for molecular or d for dissociative. The adsorption sites (Figure 4.9) are given in the first column.

The energy for molecular adsorption is in good agreement with that of Jomard *et al.,*[132] only 0.07 eV smaller than mine for a coverage of ¼ ML. The dissociative energy is also in fairly good agreement, being 0.22 eV higher here than theirs.

Previous theoretical studies have found the (110) surface to be less stable than the (111),[111,115,116] although it is more chemically active and higher water adsorption energies are obtained.[108,111] The present work agrees with this; adsorption energies are higher on the (110) than the (111) surface.

The An-O_{OH} bond distances are shorter on the (110) than (111) surface (by 0.04 Å and 0.06 Å for UO_2 and PuO_2 respectively), which might partly explain why the adsorption energy is higher on the (110) than (111) surface. However, the An-O_w distances are longer, and so do not explain why the adsorption energy is higher for molecular adsorption on the (110) surface than the (111).

The natural charges of atoms in the water molecule, and on the surface and bonded to the water molecule, have been calculated at the SV(P) level and are shown in Table 4.10. The partial charges differ by 0.04 a.u. or less between the two systems, again the charge on plutonium is slightly greater than the charge on uranium for both molecular and dissociative adsorption. As on the (111) surface, these data suggest that the different adsorption energies are unlikely to be due to differences in ionic bonding.

Type of absorption	Atom	Natural charges/ a.u.	
		UO_2	PuO_2
1m	O_{water}	-0.92	-0.93
	H	0.53	0.52
	H	0.52	0.53
	An	1.54	1.57
1d	$O_{ads\ OH}$	-0.95	-0.93
	$H_{ads\ OH}$	0.46	0.46
	$O_{surf\ OH}$	-0.88	-0.91
	$H_{surf\ OH}$	0.53	0.52
	An	1.60	1.64

Table 4.10 Natural charges on key atoms in the $An_{19}O_{38}$ cluster representation of the AnO_2 (110) surface for adsorption of a single water molecule either molecularly or dissociatively. Type of adsorption is denoted by m for molecular or d for dissociative.

Comparing the natural charges between the (111) and (110) surfaces, it can be seen that the natural charges of the surface actinide ions are higher on the (110) surface than the (111) surface, by 0.29–0.31 a.u. for uranium, and 0.24–0.26 a.u. for plutonium. This is due to the lower coordination number of uranium and plutonium at the (110) surface (6-coordinate) than the (111) surface (7-coordinate), and so on the (110) surface there are fewer oxygen ions to transfer charge to the surface actinide ions. The higher charges of the actinide ions on the (110) than (111) surface could contribute to the higher adsorption energy observed on the (110) surface. The natural charges of the hydrogen atoms and the oxygen of the water molecule differ very little between the two surfaces, the largest difference being that the charge of oxygen in molecular adsorption is 0.05 a.u. stronger on the (110) than the (111) surface.

4.3.4 Second Layer Water

As dissociative adsorption on the (110) surface was the most stable I studied, as well as there being a clear distinction between molecular and dissociative adsorption on this surface – indicating all the water molecules would be fully dissociated – I decided to use this surface when investigating water adsorbing in a second layer above the surface.

Other theoretical studies have not looked beyond a first layer of water adsorption on AnO_2 surfaces. However, experimentally there has been debate over how strongly water is adsorbed in the second layer on PuO_2; Stakebake and Haschke interpreted experimental results as a first layer of water adsorbed as hydroxyls, followed by a second layer of strong chemisorption, with weaker physisorption above this.[120,121,136,137] Paffett *et al.* however dispute this citing the lack of distinct layers of water adsorbing beyond the first layer of water on other surfaces, and suggest that the 1st layer may adsorb more strongly but then no clear distinction occurs for water adsorbing above 1 ML.[79]

I looked at adsorption of a water molecule in the second layer. As the (110) surface has stoichiometric layers of AnO_2, there are double as many oxygen sites as there are actinide sites. With a full monolayer of coverage on the (110) surface, each actinide atom is coordinated to an adsorbed hydroxyl and half the 1st layer surface oxygen atoms are bound to a hydrogen atom, forming the surface hydroxyls (Figure 4.13).

This still leaves half of the 1st layer surface oxygen atoms undercoordinated, therefore I started by placing a water molecule in the second layer to form a hydrogen bond to this undercoordinated surface oxygen in the middle of the cluster (green sphere in Figure 4.13).

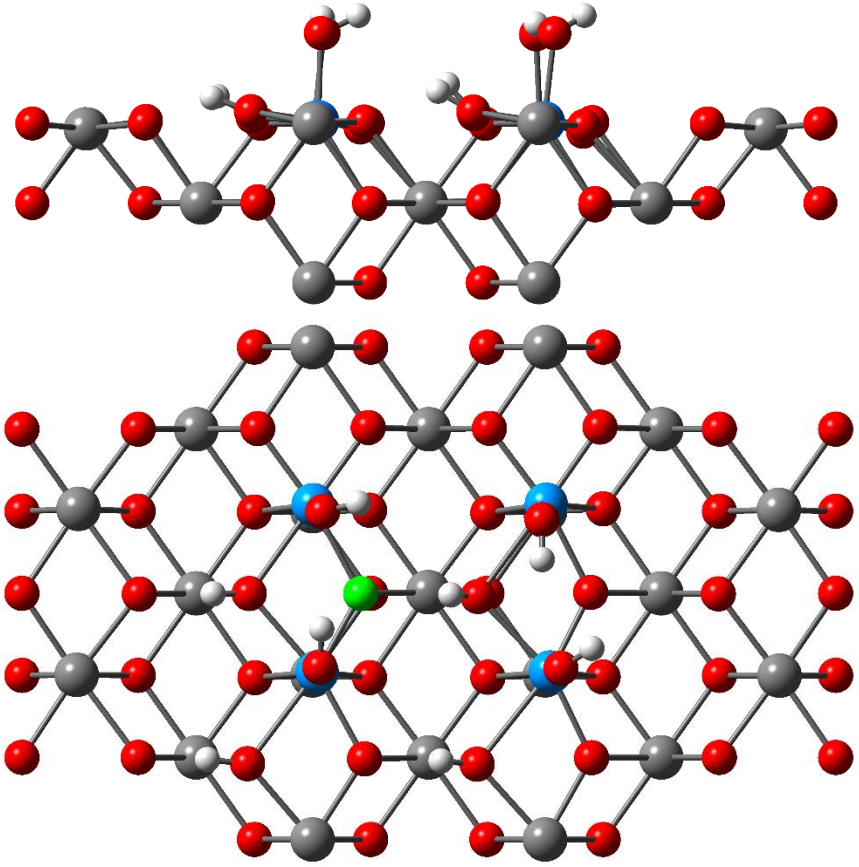

Figure 4.13 The fully hydroxylated (110) surface of a $U_4U_{21}O_{50}$ cluster. Top view shows the cluster in the plane of the surface, while the bottom view is from above the surface. Hydrogen atoms are shown in white, oxygen atoms in red (the green sphere represents an undercoordinated oxygen atom in the middle of the cluster). Actinide atoms in blue and grey. Grey spheres represent actinide ions treated with 5f-in-core PPs.

The optimized structure for the 2nd layer water molecule is shown in Figure 4.14, it forms four hydrogen bonds: one with the undercoordinated surface oxygen (1.67 Å), one with a surface hydroxyl (1.76 Å), and two with adsorbed hydroxyls (1.91 and 2.14 Å). The same method has been used that was used for 1st layer water adsorption, i.e. the geometry was optimized with the $U_4U_{21}O_{50}$ cluster, after which a single point energy calculation was performed with the $U_{25}O_{50}$ cluster, using the SV(P) basis set. The adsorption energy obtained for the second layer water molecule is -0.98 eV. The BSSE, with the two fragments taken as the hydroxylated cluster and the water molecule adsorbing in the 2nd layer, is 0.49 eV, and hence the adsorption energy including the counterpoise correction is -0.49 eV, which equates to an average of 0.12 eV per hydrogen bond (for comparison the enthalpy of a hydrogen bond in water is ~0.24 eV[138], hence the longer bonds are likely relatively weak hydrogen bonds). This is a fairly strong

adsorption in the 2nd layer, comparable with molecular water adsorption in the 1st layer on the (111) surface (-0.52 eV).

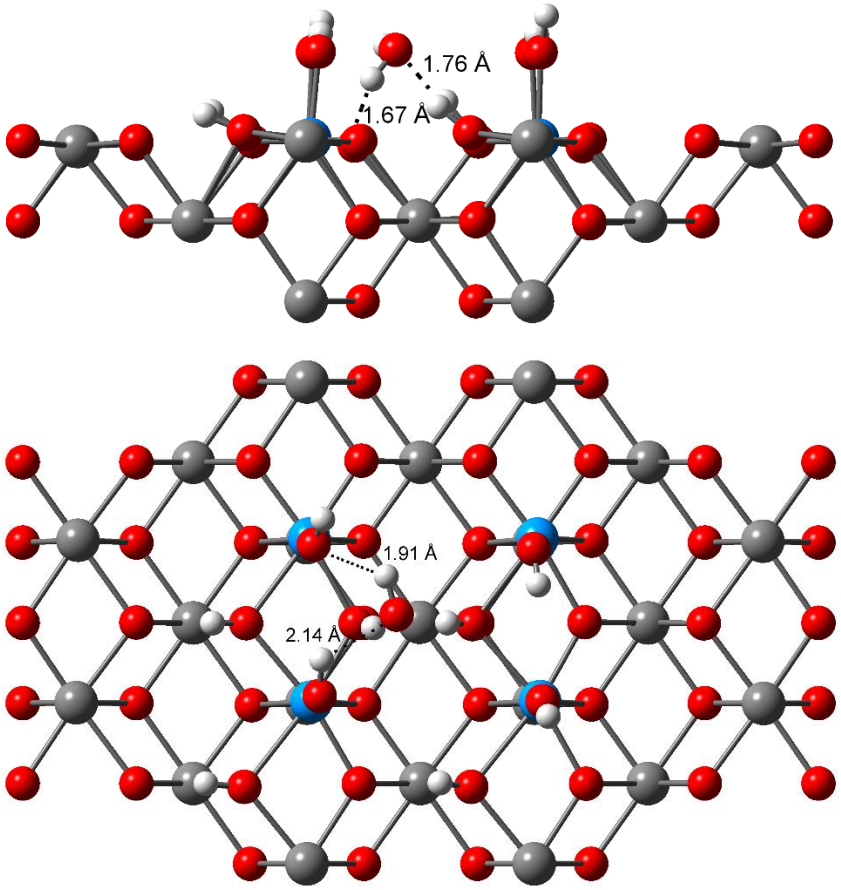

Figure 4.14 Adsorption of a second layer water molecule on the hydroxylated (110) surface of a $U_4U_{21}O_{50}$ cluster. Top view shows the cluster in the plane of the surface, while the bottom view is from above the surface. Hydrogen atoms are shown in white, oxygen atoms in red and actinide atoms in blue and grey. Grey spheres represent actinide ions treated with 5f-in-core PPs. Hydrogen bonds indicated with dotted lines and hydrogen bonds distances shown.

The same method was used to investigate water in the second layer on the hydroxylated surface of the (110) PuO_2 cluster. Again four hydrogen bonds are formed between the water molecule and the surface or hydroxyls at the surface: 1.72 Å for the undercoordinated surface oxygen, 2.03 Å for the surface hydroxyl, 1.83 and 2.03 Å for the adsorbed hydroxyls. The BSSE is slightly larger than on the UO_2 surface (0.55 eV compared to 0.49 eV on the UO_2 surface) and the adsorption energy is -0.45 eV, 0.04 eV smaller than on the UO_2 surface.

To model a fully covered cluster, I expanded the hydroxylated area to cover the whole surface cluster, by taking coordinates of the four dissociatively adsorbed water molecules in the 1st layer (from Figure 4.13) and repeating them across the

cluster. The coordinates of these four dissociatively adsorbed molecules were then optimised as well as the second layer water molecule, while the additional hydroxyl groups were kept fixed (Figure 4.15), in total there were the equivalent of 12 dissociatively adsorbed water molecules in the 1st layer of adsorption. This caused a reduction in the adsorption energy of the second layer water molecule to -0.30 eV. This reduction is most likely, in part, due to the restriction caused by the additional hydroxyl groups that were kept fixed, which leads to slightly longer hydrogen bonds (Figure 4.15).

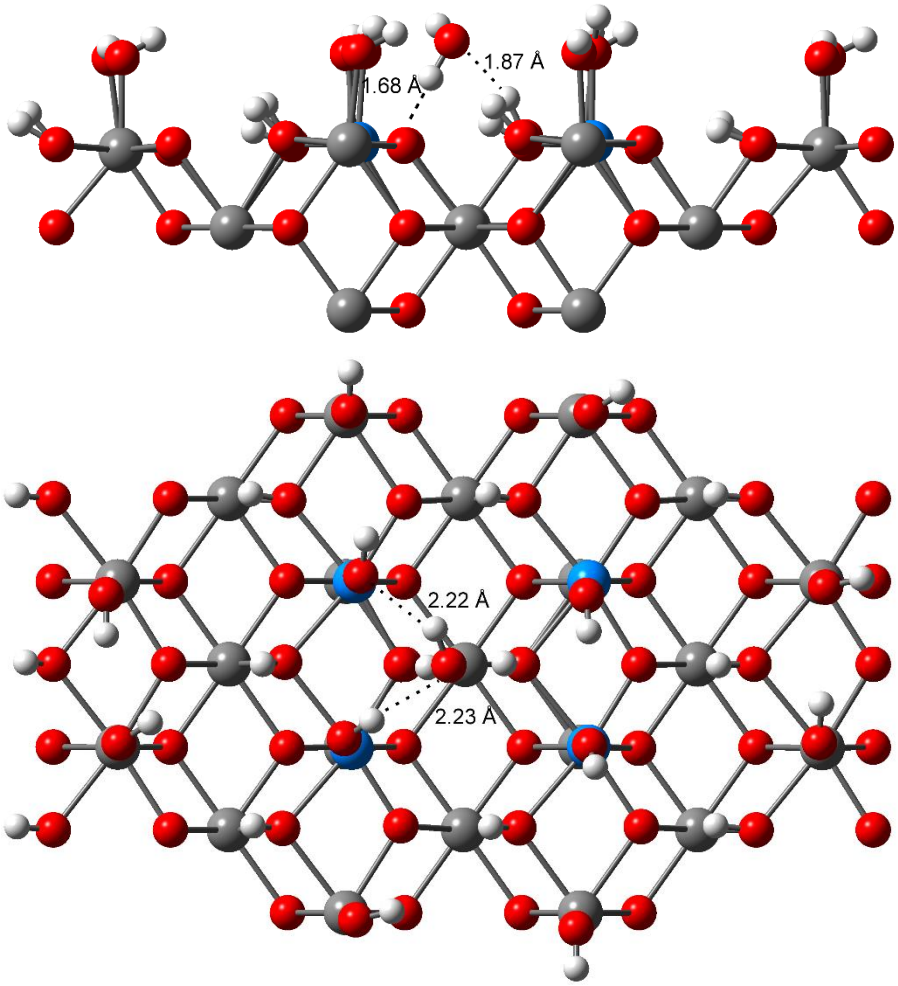

Figure 4.15 Adsorption of a second layer water molecule on the fully hydroxylated (110) surface of a $U_4U_{21}O_{50}$ cluster. Top view shows the cluster in the plane of the surface, while the bottom view is from above the surface. Hydrogen atoms are shown in white, oxygen atoms in red and actinide atoms in blue and grey. Grey spheres represent actinide ions treated with 5f-in-core PPs. Hydrogen bonds indicated with dotted lines and hydrogen bonds distances shown.

I performed the analogous calculation on the PuO_2 surface, this time there was a large increase in the adsorption energy for the 2nd layer water molecule to -0.95 eV. This large difference in the adsorption energy compared to the cluster with

four hydroxyl groups in the first layer is due to the water molecule in the 2nd layer adsorbing in a different way. The water molecule no longer hydrogen bonds to a surface oxygen atom, but forms hydrogen bonds with only surface and adsorbed hydroxyls, lying parallel to the surface (Figure 4.16).

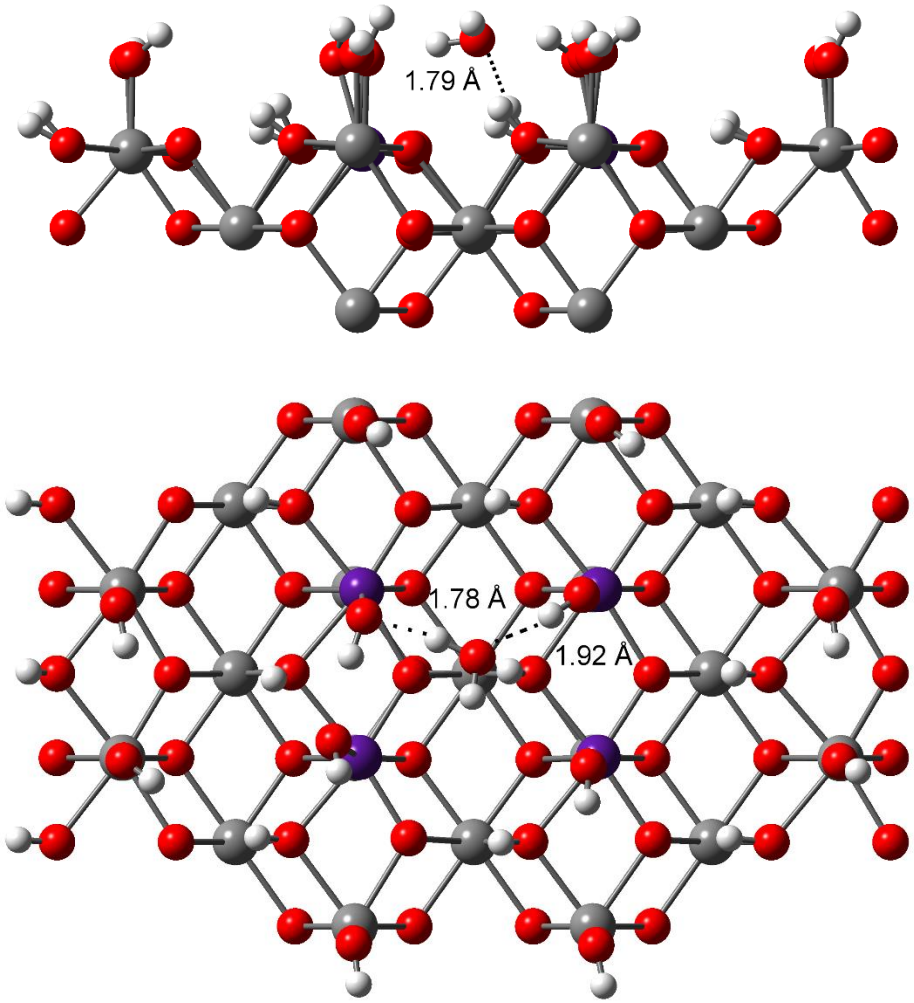

Figure 4.16 Adsorption of a second layer water molecule on the fully hydroxylated (110) surface of a $Pu_4Pu_{21}O_{50}$ cluster. Top view shows the cluster in the plane of the surface, while the bottom view is from above the surface. Hydrogen atoms are shown in white, oxygen atoms in red and plutonium atoms in purple and grey. Grey spheres represent plutonium ions treated with 5f-in-core PPs. Hydrogen bonds indicated with dotted lines and hydrogen bonds distances shown.

Three hydrogen bonds were formed with lengths of 1.78, 1.79 and 1.92 Å, this compares with four hydrogen bonds of 1.72, 1.83, 2.03, and 2.12 Å on the surface with only four hydroxyl groups in the 1st layer (where the water is hydrogen bonded to a surface oxygen atom). Although the adsorption geometry obtained from the fully hydroxylated cluster has fewer hydrogen bonds than the cluster with only four hydroxyl groups, the adsorption energy is higher, this is likely due to

there being less steric repulsion between the 2nd layer water molecule and the hydroxyl groups.

The limitations of performing static calculations of a 2nd layer water molecule need to be noted; water in the 2nd layer of the surface will be in a dynamic system, with water molecules most likely moving between the 2nd layer and higher layers above. Furthermore there are many different configurations the water molecule could adopt, dependent on the orientation of the hydroxyl groups of the 1st layer. Molecular dynamics calculations would be useful to investigate the types of configurations water adopts at the surface, whether it bonds to accessible surface oxygen atoms, or forms hydrogen bonds solely with adsorbed hydroxyl species. However the calculations here do provide information on possible configurations, indicating that water may prefer to bond with adsorbed hydroxyl species only. They also indicate that 2nd layer water adsorption could be relatively strong, as suggested by Stakebake and Haschke.[120,121,136,137]

4.4 Conclusions

On the (111) surface good agreement for both adsorption geometries and energies was found between the results calculated here, and those from a previous DFT+*U* study of water adsorption on UO_2. A mixture of molecular and dissociative adsorption was found to be most favourable when four water molecules adsorbed on the cluster, which can be attributed to hydrogen bonding between the adsorbed water molecules and hydroxyl species. Although this is in disagreement with an experimental study of water adsorption on a UO_2 (111) single crystal surface,[117] which concluded that water adsorbed molecularly on the surface, the difference in energy between molecular and dissociative adsorption is small.

Dissociative adsorption was calculated to be weaker on the PuO_2 (111) surface than the UO_2 (111), however, with multiple water molecules adsorbing a mixture of molecular and dissociative adsorption, as for UO_2, was found to be most favourable. Furthermore the adsorption geometries of water are very similar between the two systems.

On the (110) surface, the adsorption energies calculated here were greater than those found in previous DFT studies. This could be due to the embedded cluster method not being able to correctly account for surface relaxations, which leads to a greater stabilisation of the surface upon adsorption. However, as for previous studies, dissociative adsorption was calculated to be more favourable than molecular adsorption. When multiple water molecules were adsorbing to the cluster, the cases where all water molecules adsorbed dissociatively were calculated to be more favourable, indicating that the (110) surface would be hydroxylated.

Adsorption energies were much greater on the (110) than the (111) surface, as has been found in previous theoretical studies. This is likely due to the lower coordination number of surface actinide ions and, in part, to their subsequent higher charge, increasing the electrostatic attraction between the adsorbing water molecules and the surface.

Although the energies between water adsorption on the UO_2 and PuO_2 surfaces differ somewhat, water adsorbs in a similar way on both surfaces; bond distances differ by small amounts between the two systems. The most favourable type of adsorption was generally the same between the two systems: on the (111) surface a mixture of molecular and dissociative adsorption is favourable on both UO_2 and PuO_2, while on the (110) surface dissociative adsorption is favoured on both. These similarities between the two systems imply that for pristine surfaces, where no defects are present, UO_2 is a suitable surrogate system for PuO_2 to investigate water adsorption. This is important for experimental studies of water adsorption, which are particularly difficult to perform with plutonium.

5 Oxygen Vacancies

5.1 Introduction

In solid state materials defects will always be present; at surfaces, dependent on their type and concentration, defects can have significant effects on the surface reactivity and the type of adsorption that can occur. There are many different types of defects that can occur in solid state systems, however in this chapter I will focus on oxygen vacancies. I will refer to surfaces that do not contain any defects as stoichiometric surfaces, and surfaces that contain oxygen vacancies as substoichiometric surfaces.

The effect of oxygen vacancies on water adsorption has been studied in depth on other metal oxide surfaces. On the rutile (110) TiO_2 surface, despite many experimental and theoretical studies, there is still debate as to whether water adsorbs only molecularly or whether it can adsorb dissociatively on stoichiometric surfaces,[139,140] however when oxygen vacancies are present there is experimental and theoretical agreement that dissociative adsorption occurs.[141,142] On CeO_2 surfaces, calculations have shown that dissociative water adsorption is favourable to molecular on the substoichiometric surface.[131,143] On the substoichiometric Zn $(10\bar{1}0)$ surface, however, water does not adsorb dissociatively, but molecularly away from the oxygen vacancy according to DFT calculations.[144] It is clear from these studies that the presence of oxygen vacancies can have a significant impact on water adsorption.

Defect chemistry in transition metal, rare earth or actinide oxides is often hard to model with DFT; in particular, electron or hole localization due to point defects can be incorrectly described. On TiO_2 the localization or delocalization of electrons due to an oxygen vacancy has been seen to be very method dependent: with a GGA functional electrons are delocalized across the system; with GGA+*U* the extent of localization depends on the *U* value, with an increase in *U* leading to greater localization; and with hybrid functionals both scenarios can be observed, with a preference for electron localization occurring with an increase in the percentage of HF exchange used.[145] Similar results are found with cerium dioxide (a material often used as a surrogate for AnO_2 systems in experimental

studies) where the localization of electrons left from an oxygen vacancy is again dependent on the method used: GGA functionals lead to delocalization of two electrons across the system,[146] while increasing values of *U* in DFT+*U* and increasing proportions of HF exchange with hybrid functionals[22,147,148] leads to greater localization of the electrons on nearby cerium ions. A useful review discussing oxygen defects at the surface of ceria systems is given here.[149]

On AnO_2 systems, the position of the electrons left behind when an oxygen vacancy is formed has been studied less than other metal oxide systems, instead the focus has been on the oxygen vacancy formation energies.

5.1.1 Oxygen Vacancy Formation Energies

The properties of defects such as oxygen vacancies are often difficult to study experimentally – particularly for actinide systems. Theoretical studies have therefore been used to study their properties, in particular formation energies. There have been a number of periodic DFT studies that have investigated oxygen vacancies in UO_2 systems, while PuO_2, even theoretically, has not been studied in great detail.

Table 5.1 collates oxygen vacancy formation energies in bulk UO_2 and PuO_2 calculated from different periodic DFT studies. Despite most studies using similar functionals and the DFT+*U* method, there is a surprising amount of variation in the calculated values.

			Oxygen Vacancy Formation Energy/ eV	
Year	**Authors**	**Functional**	**UO_2**	**PuO_2**
2005/2006	Freyss[150,151]	PBE	6.1	5.3
2006	Iwasawa[152]	PBE+*U*	4.46	-
2009	Nerikar[153]	GGA+*U**	5.29	-
2010	Dorado[154]	PBE+*U*	5.67	-
2014	Bo[129]	PBE+*U*	6.14	-
2016	Ao[155,156]	PW91+*U*	6.79	3.76

Table 5.1 Oxygen vacancy formation energies calculated for bulk UO_2 or PuO_2 with DFT. *Specific GGA functional not mentioned in paper.

Two groups have calculated the oxygen vacancy formation energy for UO_2 and PuO_2 in different studies,[150,151,155,156] although the values differ substantially

between the groups (one set of studies used GGA and the other GGA+*U*), both found that the formation energy is higher in UO_2 than PuO_2.

The studies shown in Table 5.1 were calculated for bulk AnO_2 systems, there are fewer studies looking at point defects – in particular oxygen vacancies – at the surfaces of these systems. Bo *et al.* calculated an oxygen vacancy formation energy with the PBE+*U* exchange-correlation functional of 6.14 eV in the bulk, they also studied the vacancy formation energies at surfaces, calculating energies of 5.95 eV and 6.08 eV for 1st and 2nd layer respectively on the UO_2 (111) surface, and 5.38 eV and 5.59 eV on the UO_2 (110).[129]

Sun *et al.* investigated the effects of oxygen vacancies on surface stability and chemical activity on low index PuO_2 surfaces with DFT+*U*.[157] They calculated oxygen vacancy formation energies, where ¼ of the surface layer oxygen atoms were removed, of 2.85 eV on the (111) surface and 1.96 eV on the (110) surface, hence, as for the bulk, these energies are significantly smaller than those found on the UO_2[129] surfaces. As on the UO_2 (111) surface, there was little difference between the formation energy of a surface or subsurface oxygen vacancy, with the subsurface vacancy only 0.04 eV less stable than the surface vacancy.

Oxygen vacancies in ceria, which as mentioned in previous chapters is isostructural to AnO_2 materials, have been studied in greater detail. Molinari *et al.* calculated oxygen vacancy formation energies finding a higher value for the (111) surface (2.01 eV) than the (110) surface (1.29 eV) and, perhaps surprisingly considering the higher surface energy and lower coordination of surface oxygen atoms on the (100) than (110) surface, the (100) surface had a value higher than the (110) surface (1.61 eV).[131]

The lower oxygen vacancy formation energies on the (110) than the (111) surface that have been calculated in these studies is likely due to the lower coordination number of actinide ions on the (110) surface, as well as the higher surface energy of the (110) surface.

5.1.2 Effect of Oxygen Vacancies on Water Adsorption

Oxygen vacancies will affect how water adsorbs onto AnO_2 surfaces, from experiment it has been seen, as mentioned previously, that water adsorbs reversibly on stoichiometric UO_2,[117,118] while on substoichiometric UO_{2-x} water adsorption results in the desorption of H_2 from the surface.[117] The production of H_2 on substoichiometric surfaces implies that the water adsorbs dissociatively; a water molecule adsorbs to the defect site, with the oxygen healing the surface and the hydrogen desorbing as H_2. This would mean the substoichiometric surfaces have a preference for dissociative over molecular adsorption. This is clearly relevant to the storage of PuO_2 as any production of H_2 at the surface could contribute to pressurization that occurs.

Bo *et al.* investigated the effect of an oxygen vacancy on water adsorption on the (111) and (110) surfaces of UO_2. For molecular adsorption on the substoichiometric (111) surface they found two stable geometries: one with the molecule adsorbed in a similar geometry to the stoichiometric surface, forming a single hydrogen bond with the surface (Figure 5.1 a), and one where the water molecule adsorbs close to the vacancy, not forming any hydrogen bonds with the surface (Figure 5.1 b). On the (110) surface one stable geometry was found for molecular adsorption (Figure 5.1 c), which is similar to the geometry I found on the stoichiometric surface (Figure 4.10), but different to that found by Bo *et al*. on the stoichiometric surface (Figure 4.3).

For dissociative adsorption, they found one stable geometry on the (111) surface with a hydroxyl filling the oxygen vacancy, and the additional hydrogen adsorbing to an adjacent surface oxygen atom (Figure 5.1 d). On the (110) surface two different geometries are found, in both cases the hydroxyl group fills the oxygen vacancy, in one the other hydrogen adsorbs to an adjacent oxygen, pointing at the adsorbed hydroxyl (Figure 5.1 e), while in the other the hydrogen is adsorbed on a nearby surface oxygen, but points away from the adsorbed hydroxyl (Figure 5.1 f).

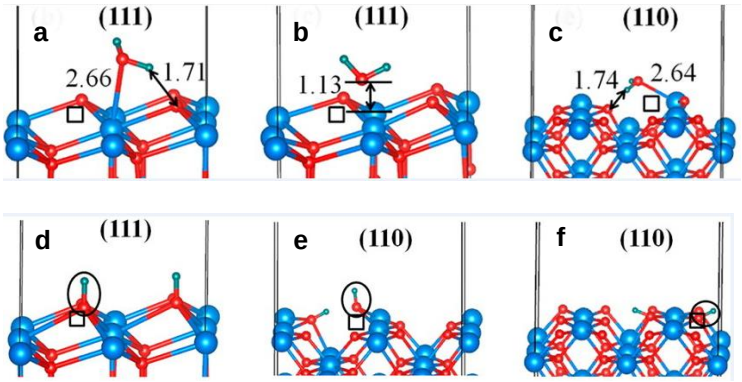

Figure 5.1 Optimized molecular (a-c), and dissociative (d-f) adsorption structures of water molecules on the substoichiometric UO_2 (111) and (110) surfaces. The oxygen and hydrogen atoms are plotted in red and green, respectively, while the uranium atoms are blue. Adapted from reference.[129]

Bo *et al.* found that in all cases the presence of an oxygen vacancy increased the adsorption energy of water, making water adsorption more stable.[129] On the (111) surface, where molecular and dissociative water adsorption had similar energies on the stoichiometric surface, the presence of an oxygen vacancy leads to a preference for dissociative adsorption. The energy of dissociative adsorption increased by 1.52 eV on the substoichiometric compared to stoichiometric surface, and by only 0.33 eV for molecular adsorption. On the (110) surface (where there was already a preference for dissociative adsorption on the stoichiometric surface), dissociative adsorption was more stable than molecular adsorption on the substoichiometric surface, the energy of dissociative adsorption increased by 0.84 eV, and molecular adsorption by 0.80 eV.

In a separate study Bo *et al*. investigated water adsorption on NpO_2 low index surfaces.[158] As for the UO_2 surface, the presence of an oxygen vacancy lead to an increase in the adsorption energy of water, however with only small increases for molecular adsorption – 0.08 eV on the (111) surface and 0.15 eV on the (100) surface (on the (110) surface a water molecule dissociated upon optimisation). There were much greater increases for dissociative adsorption with an oxygen vacancy present, 1.38 eV on the (111) surface, 0.75 eV on the (110), and 0.97 eV on the (100). It is worth noting that the large increase in the dissociative adsorption energy on the (111) surface leads to a greater adsorption energy on the substoichiometric (111) than (110) surface.

The effect of oxygen vacancies on water adsorption has been studied in more detail on CeO_2, a short but thorough overview of this area is given in Section 4.4 of a review by Paier *et al.*[149] On the stoichiometric (111) surface generally small differences are found between molecular and dissociative adsorption at low coverage (0.01–0.30 eV),[131,159–161] while water adsorption on the substoichiometric (111) surface strongly favours dissociative adsorption, with increases in the dissociative adsorption energy of up to 1.79 eV.[161] Molecular adsorption, on the other hand, has only modest increases in adsorption energy on the reduced surface, and in one case a decrease.[159]

Most studies have focused solely on the (111) CeO_2 surface, Molinari *et al.*, however, also calculated adsorption energies for water on the reduced (110) surface. They calculated an energy of -1.44 eV for dissociative adsorption on the substoichiometric (110) surface (a water molecule dissociates on optimization, therefore they give no value for molecular adsorption), this is an increase of 0.32 eV from the stoichiometric surface.[131]

On the substoichiometric surfaces dissociative adsorption restores the coordination number of the nearby metal atoms and it is clear from these studies that an oxygen vacancy causes a stabilisation of dissociative adsorption. This is perhaps unsurprising – molecular adsorption is similar on both the stoichiometric and substoichiometric surfaces, while dissociative adsorption occurs in a completely different way, with a hydroxyl adsorbing onto the oxygen vacancy site on the substoichiometric surface, instead of above a metal ion as on the stoichiometric surface.

The PEECM can work well in metal oxide systems, where the bonding is predominantly ionic, and so no covalent bonds are cleaved when producing a cluster. It also provides a useful method of studying defects in isolation, as opposed to periodic DFT where interactions can occur between defects in neighbouring unit cells and which produces concentrations of defects much higher than those found typically in experiments. Furthermore, as has been mentioned, hybrid functionals are able to account for the electronic structure in both stoichiometric and substoichiometric metal oxide systems, however, they

are computationally expensive with periodic DFT, whereas the use of hybrid functionals is more feasible with embedded cluster calculations.

Burow *et al.* initially used the PEECM to study oxygen vacancies in bulk and surface CeO_2,[22] where their calculated oxygen vacancy formation energies at the (111) surface were with in excellent agreement with a periodic DFT study using the HSE functional,[147] and in good agreement with DFT+*U* studies.[147,162] More generally embedded cluster methods have been used to study defect sites in ionic systems, such as CO_2 adsorption at oxygen vacancy sites on MgO.[163]

5.2 Computational Details

I used the same clusters as were used in Chapter 4, so that adsorption energies of water with and without an oxygen vacancy can be compared. When optimizing the geometries of the cluster an additional actinide ion in the second layer had its 5f electrons treated explicitly, as the unpaired electrons left when an oxygen vacancy is formed could localise on it. Hence geometry optimizations were performed on the $U_5U_{14}O_{37}$ and $U_5U_{20}O_{49}$ clusters (Figure 5.2 and Figure 5.3 respectively), before single point energy calculations were performed on the $U_{19}O_{37}$ and $U_{25}O_{49}$ clusters.

Initially oxygen vacancy formation energies were calculated with the following equation:

$$E_{\mathrm{form}} = E_{\mathrm{Surf+O_{vac}(opt)}} - E_{\mathrm{Surf(opt)}} + \frac{1}{2}E_{\mathrm{O_2(opt)}} \qquad (5.1)$$

Where $E_{\mathrm{Surf+O_{vac}(opt)}}$ is the energy of the cluster with an oxygen vacancy, $E_{\mathrm{Surf(opt)}}$ the energy of the stoichiometric cluster and $E_{\mathrm{O_2(opt)}}$ is the energy of the gas phase O_2 molecule. The O_2 molecule in its triplet state is used as a reference state, as opposed to the O atom, as most previous theoretical studies[129,131,150–154] use this reference state, making a comparison with our calculations more valid. As the dissociation energy of the O_2 molecule is very method dependent (e.g. it is in good agreement with experiment using hybrid functionals, while it is overestimated with GGA functionals) using the O atom as a reference state would

cause large variation in the oxygen vacancy formation energy obtained from different DFT methods.

The two electrons left when a neutral oxygen vacancy is formed are unpaired (with the same spin as the unpaired electrons on the actinide ions) as this was calculated to be more stable than the paired scenario. Hence for a calculation of the $U_{19}O_{37}$ cluster there are 40 unpaired electrons, 38 from the uranium ions, and two from the oxygen vacancy.

The BSSE was accounted for again with the counterpoise correction (CP); the stoichiometric surface was taken as the whole system, while a single oxygen atom and the cluster with an oxygen vacancy as the fragments, hence the BSSE is calculated as:

$$BSSE = E^{\mathrm{Surf+O_{vac}+O}}_{\mathrm{Surf+O_{vac}(opt)}} - E^{\mathrm{Surf+O_{vac}}}_{\mathrm{Surf+O_{vac}(opt)}} + E^{\mathrm{Surf+O_{vac}+O}}_{\mathrm{O(opt)}} - E^{\mathrm{O}}_{\mathrm{O(opt)}} \qquad (5.2)$$

As in Equation (4.2), the parts of the system with basis sets included in the calculation are shown in superscript, and the parts of the system included in the electronic structure calculation are shown in subscript. The BSSE energy calculated was then added to the energy of the stoichiometric surface and the oxygen vacancy formation energy recalculated. The CP reduces the oxygen vacancy formation energy.

For the water adsorption calculations the BSSE was calculated as in Chapter 4, Equations (4.2) and (4.3).

5.3 Results

5.3.1 Oxygen Vacancy Geometries

Oxygen vacancies were formed on the AnO_2 clusters used for the water adsorption calculations, i.e. $An_{19}O_{37}$ for the (111) surface and $An_{25}O_{49}$ for the (110) surface, with the geometry optimizations performed on the $An_5An_{14}O_{37}$ cluster for the (111) surface and $An_5An_{20}O_{49}$ for the (110) surface (see Figure 5.2 and Figure 5.3 for the additional actinide treated with a small core ECP in the second layer of the (111) and (110) surface clusters respectively). As before, geometry optimisations were performed with atoms in the QM cluster that are

coordinated only to other atoms in the QM cluster having their coordinates allowed to relax. An oxygen atom was removed in either the first or second layer, when in the 1st layer, the oxygen atom adjacent to the site of a single molecular water adsorption in Chapter 4 was chosen. The optimized geometries of the clusters containing the oxygen vacancies on the UO_2 (111) surface are shown in Figure 5.2, and on UO_2 (110) in Figure 5.3.

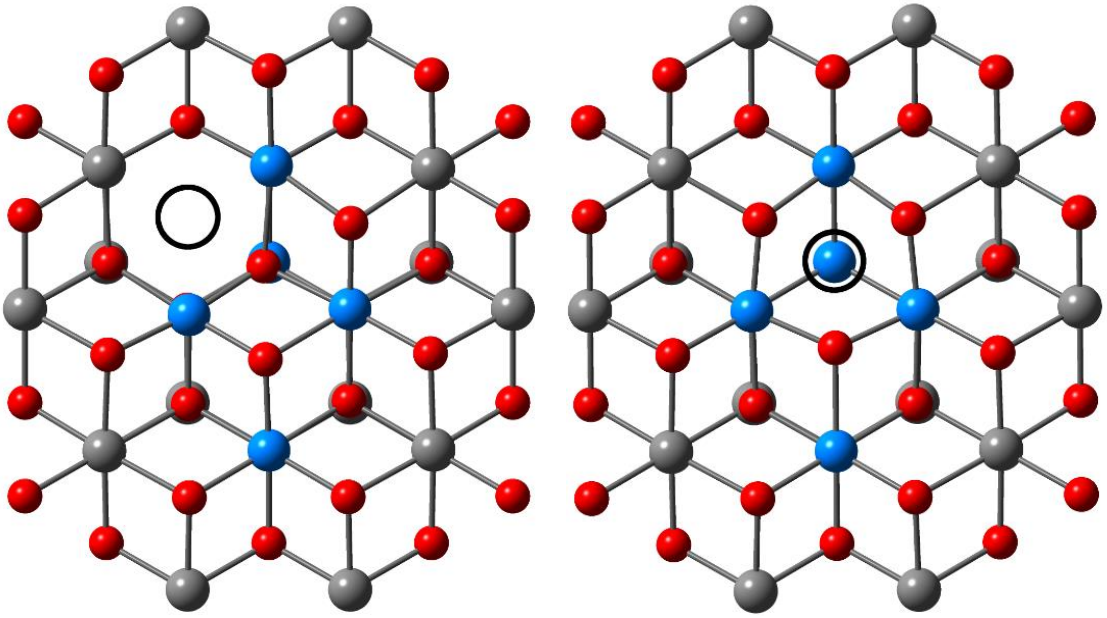

Figure 5.2 $U_5U_{14}O_{37}$ cluster containing an oxygen vacancy in the 1st oxygen layer (left) and 2nd layer (right). The cluster is viewed from above the (111) surface. Oxygen atoms are shown in red and actinide atoms in blue and grey. Grey spheres represent actinide atoms treated with 5f-in-core PPs. The position of the oxygen vacancy is indicated with a black circle. Embedding ions not shown.

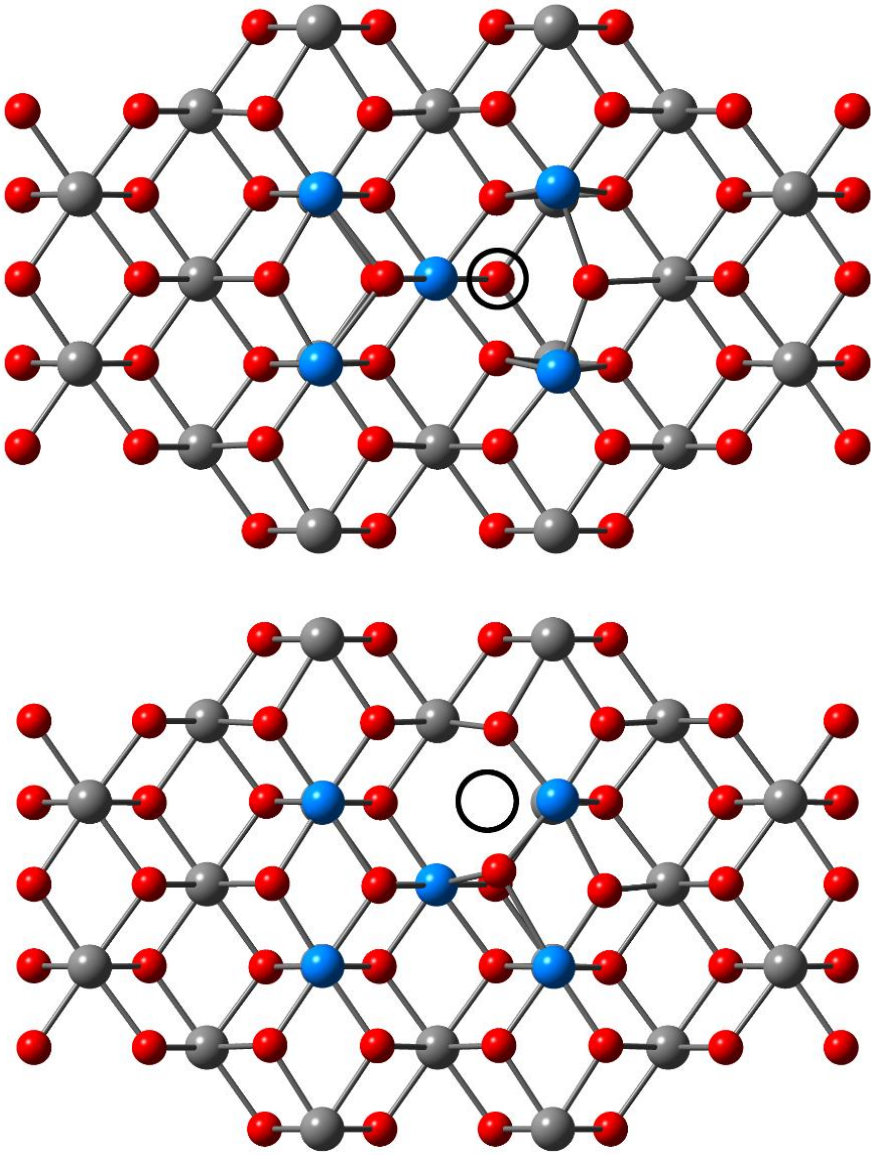

Figure 5.3 $U_5U_{20}O_{49}$ cluster containing an oxygen vacancy in the 1st oxygen layer (top) and 2nd layer (bottom). The cluster is viewed from above the (110) surface. Oxygen atoms are shown in red and actinide atoms in blue and grey. Grey spheres represent actinide atoms treated with 5f-in-core PPs. The position of the oxygen vacancy is indicated with a black circle. Embedding ions not shown.

The oxygen vacancy causes some significant movement of nearby atoms, the average displacements of the nearest neighbour atoms from the oxygen vacancy are show in Figure 5.4, negative values indicate movement of the atoms away from the oxygen vacancy, while positive values indicate movement towards the vacancy.

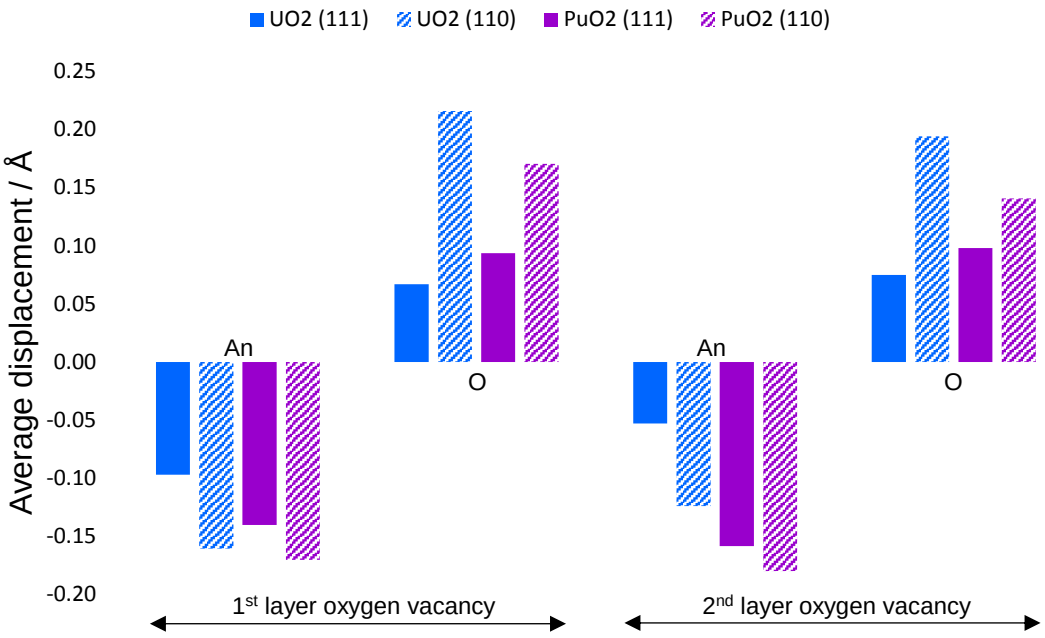

Figure 5.4 Average displacement of nearest neighbour atoms (either An or O) from the oxygen vacancy compared to the stoichiometric cluster. Positive displacements indicate movement towards the vacancy site, while negative displacements indicate movement away.

The nearest neighbour actinide atoms move away from the oxygen vacancy site; with the removal of an oxygen ion, the surrounding actinide ions are no longer shielded from each other, and hence repel each other, moving away from the vacancy. The nearest neighbour oxygen atoms, meanwhile, move towards the oxygen vacancy. Studies of oxygen vacancies in UO_2[152] and CeO_2[22] have both found the similar types of displacement of the nearest neighbour ions.

Larger displacements are seen on the (110) surface than the (111) surface. On the (110) surfaces, an oxygen vacancy in the 1st layer (top Figure 5.3), causes the adjacent oxygen atom (to the right of the oxygen vacancy in Figure 5.3) to move significantly (0.30–0.40 Å) towards the oxygen vacancy, this causes the large displacements seen in Figure 5.4 compared to the (111) surfaces.

Generally displacements are larger on the PuO_2 than the UO_2 surfaces, however, oxygen displacements on the (110) surface follow the opposite trend, being larger on the UO_2 (110) surface.

5.3.2 Oxygen Vacancy Formation Energies

Single point oxygen vacancy formation energies were performed at the geometries obtained with the $An_5An_{14}O_{37}$ and $An_5An_{20}O_{49}$ clusters for the (111)

and (110) surfaces respectively but without any 5f-in-core ECPs (i.e. on the $An_{19}O_{37}$ and $An_{25}O_{49}$ clusters). The basis set superposition error was corrected for by using the counterpoise correction method as described above, the BSSE for the oxygen vacancy formation energies was approximately 0.2-0.3 eV, and is included in the oxygen vacancy formation energies, which are shown in Table 5.2.

		Oxygen Vacancy Formation Energy/ eV	
Surface	**Layer**	**UO_2**	**PuO_2**
(111)	1st	5.92	3.63
	2nd	5.93	3.93
(110)	1st	5.15	2.38
	2nd	6.43	4.27

Table 5.2 Oxygen vacancy formation energies of UO_2 and PuO_2 on the (111) surface modelled as a $An_{19}O_{37}$ cluster and the (110) surface modelled as a $An_{25}O_{49}$ cluster within the PEECM.

The oxygen vacancy formation energies at the UO_2 (111) surface are in good agreement with Bo *et al*., who calculated energies of 5.95 eV in the first layer and 6.08 eV in the second layer.[129] For the (110) surface there is a much greater difference in the formation energies between the 1st and 2nd layers, with a vacancy being 1.28 eV more stable in the 1st layer. The calculated values here bracket the periodic DFT+*U* values of Bo *et al.* who calculated a less significant difference (5.38 eV for the first layer and 5.59 for the second layer).[129]

On CeO_2 surfaces small differences (0.01–0.18 eV) have been calculated between 1st and 2nd layer oxygen vacancy formation energies on the (111) surface,[146,164,165] in agreement with the results here (some studies even calculate the 2nd layer vacancy to be more stable).[146,148] In addition scanning tunnelling microscopy studies of the CeO_2 (111) surface have found almost equal concentrations of surface and subsurface oxygen vacancies on slightly reduced surfaces, indicating a similar formation energy for both.[165] On the (110) surface, however, larger differences have been noted between 1st and 2nd layer oxygen vacancies formation energies, with energies differing by 0.91–1.44 eV,[146,166] again this agrees with the results calculated here for both UO_2 and PuO_2, but differs to that found by Bo *et al.*[129] for UO_2.

In both this and the DFT+*U* study it is much easier to produce an oxygen vacancy in the first layer of the (110) surface than the (111), this is likely due to the lower coordination number (CN) of the 1st layer actinide on the (110) surface, CN=6, compared to the (111) surface, CN=7. This has also been noted on CeO_2 surfaces – where the coordination numbers at the surfaces are the same as in AnO_2.[148,149,162] By contrast it is easier to produce an oxygen vacancy in the 2nd layer on the (111) surface than the (110) – in the second layer the oxygen atoms are fully coordinated on both surfaces.

Oxygen vacancies on PuO_2 surfaces are calculated to be easier to form than on UO_2 surfaces, which agrees with previous theoretical calculations (see Table 5.1) which were performed on bulk AnO_2 systems. The values calculated here for the oxygen vacancy formation energy on PuO_2 surfaces are different to those calculated by Sun *et al*., however they also found a much lower formation energy on the (110) than the (111) surface.[157]

The difference in oxygen vacancy formation energy between UO_2 and PuO_2 could be due to their different redox properties. As mentioned previously, two electrons are left behind when an oxygen vacancy is formed, and these electrons can reduce the nearby metal ions. Comparing the reduction potentials of Pu^{4+} and U^{4+}, it can be seen that the potential is much larger for plutonium than uranium:[167]

$$\begin{aligned} U^{4+} + e^- &\rightleftharpoons U^{3+} \qquad E = -0.52 \\ Pu^{4+} + e^- &\rightleftharpoons Pu^{3+} \qquad E = +1.01 \end{aligned} \tag{5.3}$$

Hence Pu^{4+} is more readily reduced than U^{4+}, which could explain the higher oxygen vacancy formation energy for uranium than plutonium. The reduction potential for Ce^{4+} (E = + 1.72)[167] is even higher than Pu^{4+}, and cerium dioxide has an even lower oxygen vacancy formation energy than PuO_2, as the cerium is readily reduced to the +3 oxidation state – the readily accessible +3 oxidation state is used in cerium dioxide's applications as a sensor, in solid oxide fuel cells and oxidative catalysis in motor vehicle exhausts.[149,168]

Natural population analysis was performed on the oxygen vacancy clusters. For oxygen vacancies formed on PuO_2 surfaces there is an increase in spin density

of 0.83–0.89 a.u. on two plutonium atoms neighbouring the oxygen vacancy site, indicating that the two electrons left behind from the oxygen vacancy localize on these Pu atoms, reducing them from Pu^{4+} to Pu^{3+}.

On the UO_2 surfaces it is more complicated, for the 1st layer vacancy on the (111) surface the two electrons are spread across three uranium atoms, with increases in spin density of 0.31, 0.55, and 1.04 a.u. This is similar to results from Bo *et al.* who found that the two electrons localize on three uranium atoms near the vacancy, resulting in one U^{3+} ion and two $U^{(3+\delta)+}$ ions.[129] On the (110) surface for the 1st layer vacancy the two electrons again spread across three uranium atoms, this time with increases in spin density of 0.38, 0.52 and 0.83 a.u., however Bo *et al.* calculated the two electrons to localize on just two neighbouring U atoms, resulting in two U^{3+} ions.[129]

The fact that the two electrons are localised on two neighbouring plutonium atoms, reducing them, while for uranium they are spread across three atoms could be related to their reduction potentials. As U(IV) has a lower reduction potential it is less readily reduced, hence the electrons are not localised on two uranium atoms, but spread across three.

I wanted to see whether increasing the proportion of Hartree-Fock exchange in the functional I used would have an effect on the electron localisation with an oxygen vacancy present (the PBE0 functional uses 25% Hartree-Fock exchange). For the 1st layer vacancy on the UO_2 (111) surface I performed a single point energy calculation with the BHLYP functional (50% Hartree-Fock exchange), at the geometry optimised with the PBE0 functional. The functional has little effect on the electron localisation, with the two electrons still found across three uranium ions, with increases in spin density due to the oxygen vacancy of 0.36, 0.48 and 1.12 a.u on the uranium ions surrounding the vacancy.

5.3.3 Water Adsorption on the (111) Surface

To investigate how oxygen vacancies impact on water adsorption on the (111) surface I took the substoichiometric cluster $U_{19}O_{37}$, where the oxygen vacancy is in the 1st layer (left in Figure 5.2), and added water, adsorbing molecularly (in 2 different ways) or dissociatively, to these clusters.

For the first molecular adsorption, a water molecule was placed in the same geometry as that optimized on the stoichiometric surface, with one of the closest surface oxygen sites now being vacant (Figure 5.5). After geometry optimization of the cluster, the U-O_W bond length is 2.61 Å, slightly longer compared with adsorption on the stoichiometric surface (2.57 Å). This is 0.05 Å shorter than that calculated by Bo *et al.* with periodic DFT+*U*, who also found a shortening of the U-O_w bond length going from the stoichiometric to substoichiometric surfaces (by 0.05 Å).[129] The H-O_S distance is 1.60 Å, significantly shorter than that found on the stoichiometric surface (1.76 Å). This is also significantly shorter than the 1.71 Å calculated by Bo *et al.*, who actually found the H-O_s distance to lengthen by 0.10 Å on going from the stoichiometric to substoichiometric surface.

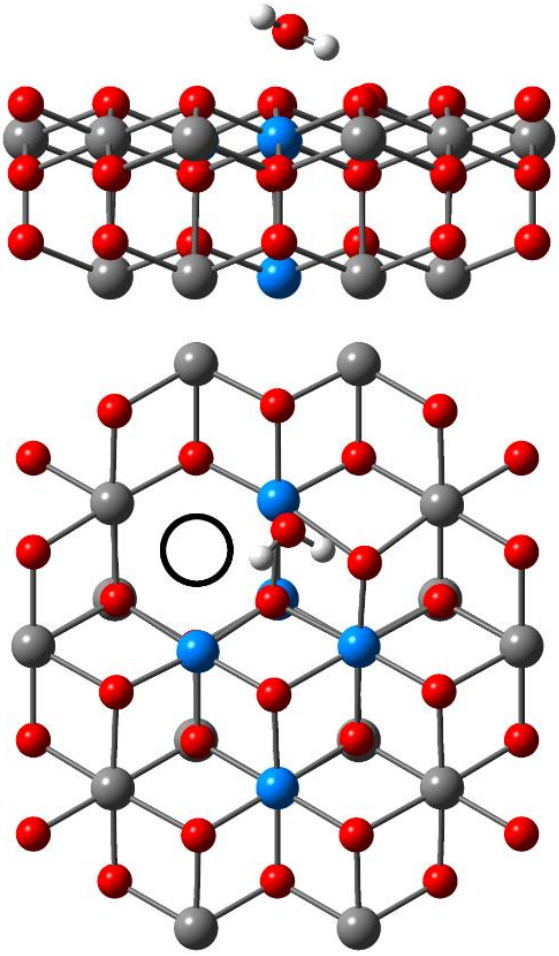

Figure 5.5 Molecular adsorption of a single water molecule on the (111) surface of a $U_5U_{14}O_{37}$ cluster. Top view shows the cluster in the plane of the surface, while the bottom view is from above the surface. Hydrogen atoms are shown in white, oxygen atoms in red and actinide atoms in blue and grey. Grey spheres represent actinide ions treated with 5f-in-core PPs. The position of the oxygen vacancy is indicated with a black circle. Embedding ions not shown.

The same method was adopted for investigating molecular adsorption on the PuO_2 (111) surface with an oxygen vacancy; the geometry of the water molecule on the stoichiometric surface was taken, and then optimized on the substoichiometric cluster at an adjacent surface oxygen site. However, on the PuO_2 surface the water molecule optimized to the dissociative configuration, indicating a low barrier between molecular and dissociative adsorption.

For the second type of molecular adsorption on the (111) cluster the water molecule was placed above the oxygen vacancy, with the hydrogen atoms pointing away from the surface, in a geometry that had been found in a periodic DFT study (Figure 5.1 b). Upon geometry optimization the water molecule moves slightly off the centre of the oxygen vacancy site and optimizes to a position between two uranium atoms adjacent to the oxygen vacancy site (Figure 5.6). The two U-O_w distances are 2.65 Å and 2.86 Å, the shorter being similar to U-O_w distance for the water molecule adsorbing above a uranium atom (2.57 Å on the stoichiometric surface, 2.61 Å with an oxygen vacancy present). As the hydrogen atoms are pointing away from the surface there is no hydrogen bonding between the water molecule and the surface, unlike for water adsorbing above a uranium atom. One of the O_w-H distances is slightly longer at 1.03 Å. The water molecule sits 1.07 Å above the oxygen vacancy, close to the 1.13 Å calculated by Bo *et al*.[129]

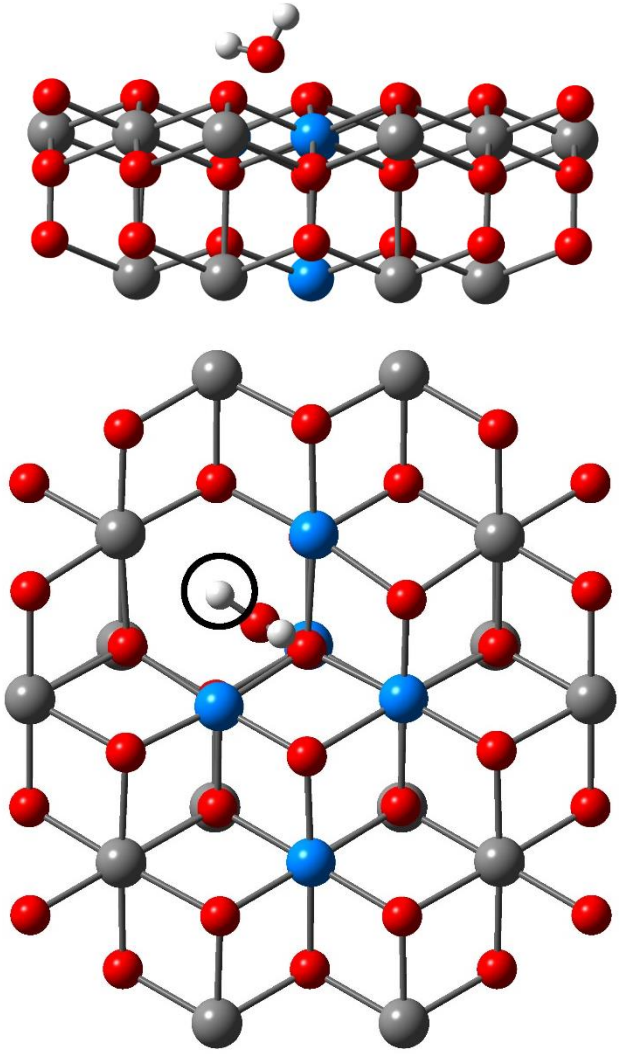

Figure 5.6 Molecular adsorption of a single water molecule on the (111) surface of a $U_5U_{14}O_{37}$ cluster above the oxygen vacancy. Top view shows the cluster in the plane of the surface, while the bottom view is from above the surface. Hydrogen atoms are shown in white, oxygen atoms in red and actinide atoms in blue and grey. Grey spheres represent actinide ions treated with 5f-in-core PPs. The position of the oxygen vacancy is indicated with a black circle. Embedding ions not shown.

A water molecule was also placed above the oxygen vacancy on the PuO_2 (111) cluster, however upon geometry optimization the water molecule moved to bond between two other surface actinide ions closer to the edge of the cluster (Figure 5.7). The adsorption geometry is similar to that on the UO_2 (111) surface – on the PuO_2 surface the Pu-O_w distances are 2.65 Å and 2.97 Å (compared to 2.65 Å and 2.86 Å on the UO_2 surface).

I wanted to compare the adsorption energies for the 2nd kind of molecular adsorption in the same position on the UO_2 (111) and PuO_2 (111) clusters, as the adsorption energy might be increased by the water molecule being closer to the

edge. Therefore I took the geometry of the optimized water molecule on the UO_2 surface, relative to the nearest uranium atom, as in Figure 5.6, and placed that on the PuO_2 surface, starting the optimization process again from this geometry, however this optimized to a dissociative adsorption.

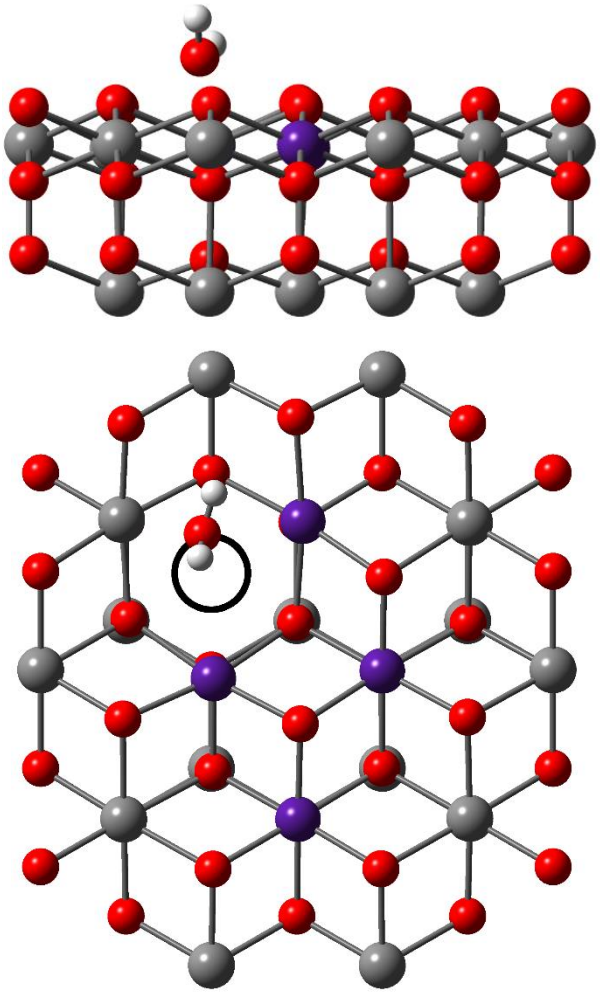

Figure 5.7 Molecular adsorption of a single water molecule on the (111) surface of a $Pu_5Pu_{14}O_{37}$ cluster above the oxygen vacancy. Top view shows the cluster in the plane of the surface, while the bottom view is from above the surface. Hydrogen atoms are shown in white, oxygen atoms in red and plutonium atoms in purple and grey. Grey spheres represent plutonium ions treated with 5f-in-core PPs. The position of the oxygen vacancy is indicated with a black circle. Embedding ions not shown.

For dissociative adsorption an OH group is placed above the oxygen vacancy, while the other hydrogen atom is placed above an adjacent oxygen site (Figure 5.8). After optimisation, the two OH groups have O-H bond lengths of 0.97 Å, on the stoichiometric surface one group has a bond length of 0.96 Å, while the other is slightly longer at 1.01 Å. The two groups lie slightly above the plane of the surface, with U-OH lengths ranging from 2.50–2.73 Å compared with 2.30–2.50

Å on the stoichiometric cluster, and the oxygen atoms in the OH groups moving by 0.46 Å in the z direction, compared with their positions in the stoichiometric cluster. Dissociative adsorption on the stoichiometric surface occurs with a very different geometry in comparison with the substoichiometric surface; on the stoichiometric surface the hydroxyl groups lie close to each other, forming a hydrogen bond. However, on the substoichiometric surface the OH groups lie over 4 Å apart and so there is no direct interaction between them.

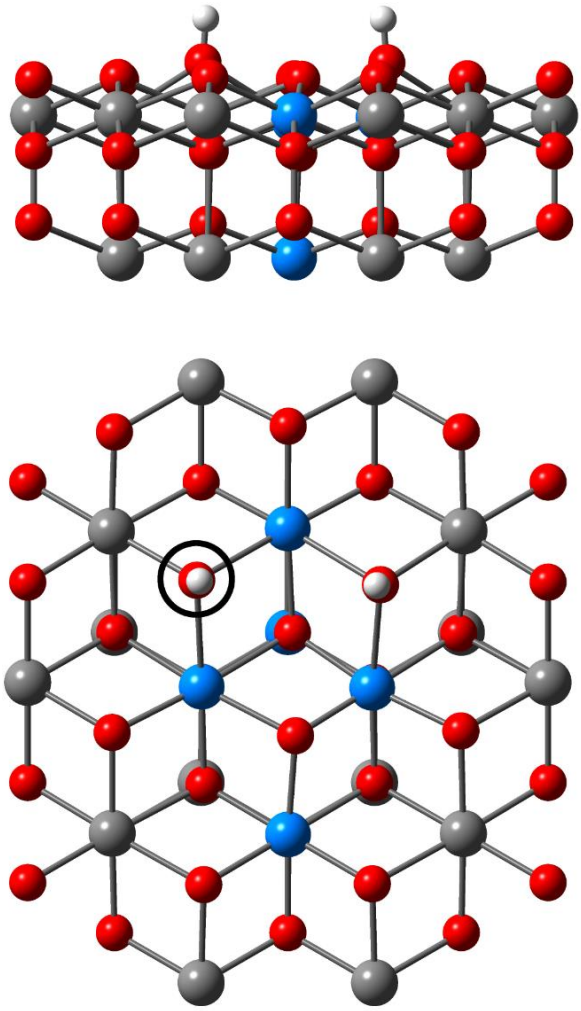

Figure 5.8 Dissociative adsorption of a single water molecule on the (111) surface of a $U_5U_{14}O_{37}$ cluster. Top view shows the cluster in the plane of the surface, while the bottom view is from above the surface. Hydrogen atoms are shown in white, oxygen atoms in red and actinide atoms in blue and grey. Grey spheres represent actinide ions treated with 5f-in-core PPs. The position of the oxygen vacancy is indicated with a black circle. Embedding ions not shown.

Adsorption occurs in a similar way on the PuO_2 surface, again the two OH groups have O-H lengths of 0.97 Å. As on UO_2 the OH groups lie above the plane of the surface, with Pu-O distances lengthening from 2.27–2.45 Å on the stoichiometric

surface to 2.48–2.65 Å on the substoichiometric surface with the dissociated water. The lengthening is due in part to the movement of the OH groups above the surface, with the oxygen atoms lying 0.44–0.46 Å higher in the z direction than on the stoichiometric surface.

Adsorption energies for the two types of molecular adsorption and dissociative adsorption on the UO_2 and PuO_2 (111) surfaces containing an oxygen vacancy are shown in Table 5.3.

	Adsorption Energy/ eV			
	SV(P) + CP		SV(P) + CP + D3	
Adsorption Type	**UO_2**	**PuO_2**	**UO_2**	**PuO_2**
Molecular1[a]	-0.58	–	-0.74	–
Molecular2[b]	-0.61	-0.81	-0.80	-1.06
Dissociative	-1.93	-2.51	-2.13	-2.77

Table 5.3 Water adsorption energies (eV) on the UO_2 and PuO_2 (111) surfaces modelled as an $An_{19}O_{37}$ cluster within the PEECM. [a] Molecular1 adsorption occurs with the water molecule adsorbing above the actinide ion, as shown in Figure 5.5. [b] Molecular2 adsorption occurs with the water molecule adsorbing above the actinide ion, as shown in Figure 5.6.

The energy for molecular adsorption on the UO_2 (111) surface does not increase much from the stoichiometric surface, only 0.06 eV or 0.09 eV for the two types of molecular adsorption on the substoichiometric surface. The values obtained here are lower than those found by Bo *et al.*, who calculated adsorption energies of -0.94 eV and -0.88 eV on the substoichiometric surface, corresponding to increases of 0.27 eV and 0.33 eV from the stoichiometric surface. There is a more significant increase for molecular adsorption on the PuO_2 surface, with the energy increasing by 0.28 eV, although this optimisation occurred with the water molecule moving towards the edge of the cluster, which could have led to an artificial increase in the adsorption energy.

Dissociative adsorption, however, is much more favourable on the substoichiometric (111) surface, with an increase in the adsorption energy of 1.30 eV from the stoichiometric surface for UO_2 (111) and an increase of 2.06 eV for PuO_2 (111). Bo *et al.* also calculated a large increase in the dissociative adsorption energy on the substoichiometric surface of UO_2 (111) (1.52 eV), the value calculated here, however, is lower than their value of -2.20 eV. The hydroxyl

formed from the dissociation of the water molecule sits in the oxygen vacancy site, hence increasing the coordination numbers of the nearby actinide ions.

There is a big difference of 0.58 eV in the dissociative adsorption energy between the UO_2 and PuO_2 (111) surfaces, this contrasts with the stoichiometric surface, where the differences between adsorption on the compounds was small. I performed natural population analysis on the substoichiometric clusters with dissociated water adsorbed; on the UO_2 surface, the two electrons from the oxygen vacancy are now localised on two uranium ions (with spin densities of 2.89 a.u. and 2.94 a.u. compared to 2.04–2.13 a.u. on the other uranium ions in the cluster, this data can be seen in Table A.1), compared to across three when the dissociated water molecule is not present. This could cause the smaller adsorption energy on the UO_2 than the PuO_2 surface (where the two electrons are localised on two plutonium ions before and after the water is adsorbed), as the dissociated water causes the two electrons to localise on two uranium ions. The same population analysis performed for the molecular adsorption on the UO_2 (111) surface shows that the electrons are as on the substoichiometric surface without water, i.e. spread across three atoms (Table A.1).

As for the stoichiometric surface, the inclusion of dispersion with the D3 parameters does not change the ordering of energies on the substoichiometric surface. Again there is a greater increase in adsorption energies on the PuO_2 than UO_2 cluster; the energies are increased by 0.16–0.20 eV on the UO_2 cluster, and 0.25–0.26 eV on the PuO_2 cluster.

5.3.4 Water Adsorption on the (110) Surface

The substoichiometric cluster $U_{25}O_{49}$, where the oxygen vacancy is in the 1st layer (top in Figure 5.3) was used to investigate water adsorption on the (110) surface. Molecular and dissociative adsorption on the cluster with an oxygen vacancy were both investigated.

For molecular adsorption a water molecule was placed in the same position it adsorbed to the stoichiometric cluster, before a geometry optimisation was performed. The water molecule adsorbs adjacent to the oxygen vacancy; the optimized structure is shown in Figure 5.9. The U-O_w bond length is 2.65 Å, the

same length as on the stoichiometric surface, it is also in good agreement with results from periodic DFT where a bond length of 2.64 Å[129] was found. The O_s-H bond lengths are 1.80 Å and 1.94 Å, compared to 1.78 Å and 2.13 Å on the stoichiometric surface, the Bo *et al.* study found the shorter O-H bond length to be 1.74 Å.[129]

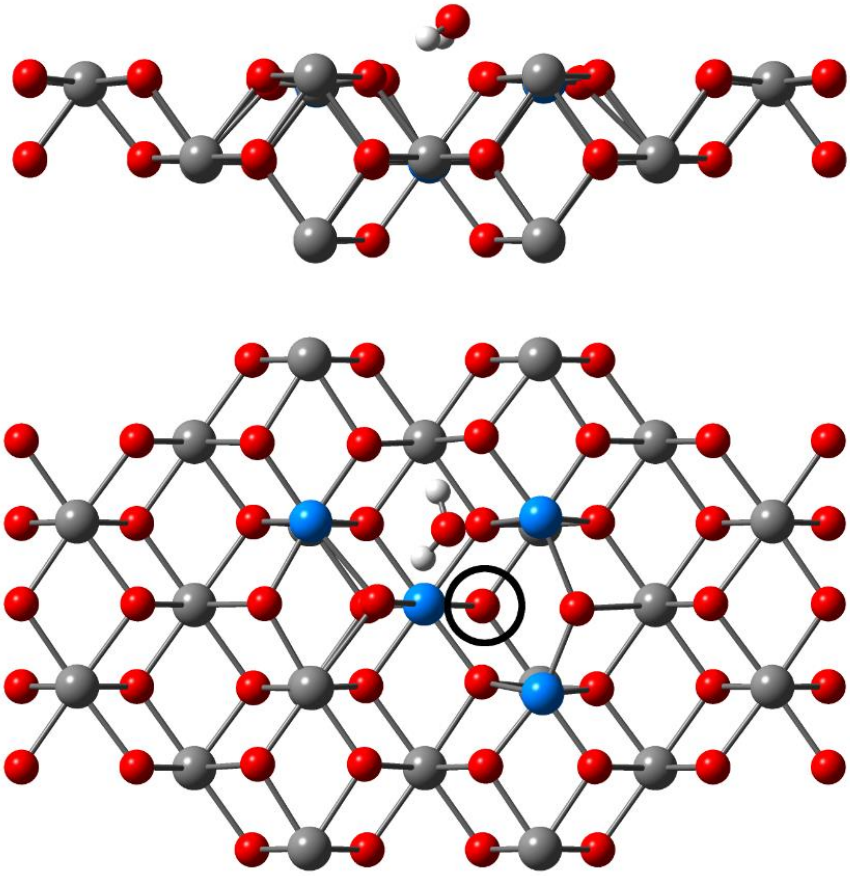

Figure 5.9 Molecular adsorption of a single water molecule on the (110) surface of a $U_5U_{20}O_{49}$ cluster. Top view shows the cluster in the plane of the surface, while the bottom view is from above the surface. Hydrogen atoms are shown in white, oxygen atoms in red and actinide atoms in blue and grey. Grey spheres represent actinide ions treated with 5f-in-core PPs. The position of the oxygen vacancy is indicated with a black circle. Embedding ions not shown.

Molecular adsorption occurs in a similar way on the substoichiometric PuO_2 (110) surface, with a Pu-O_w distance of 2.65 Å, and O_s-H distances of 1.80 Å and 1.84 Å, all longer than on the stoichiometric surface, by 0.11 Å, 0.07 Å, and 0.16 Å respectively.

For dissociative adsorption two initial structures were investigated, as had been done by Bo *et al.*[129] For the first an OH group was placed at the oxygen vacancy site, while an additional hydrogen atom was placed above an adjacent surface

oxygen site (Figure 5.10). After optimisation, the O-H bond lengths of the surface hydroxyls are 0.99 and 1.00 Å, compared with 0.98 Å on the stoichiometric surface. The oxygens of the hydroxyls lie above the surface slightly, being 0.20 Å and 0.25 Å higher than an oxygen atom in the bulk terminated surface. The two hydroxyls are pointing away from each other and so there is minimal interaction between them.

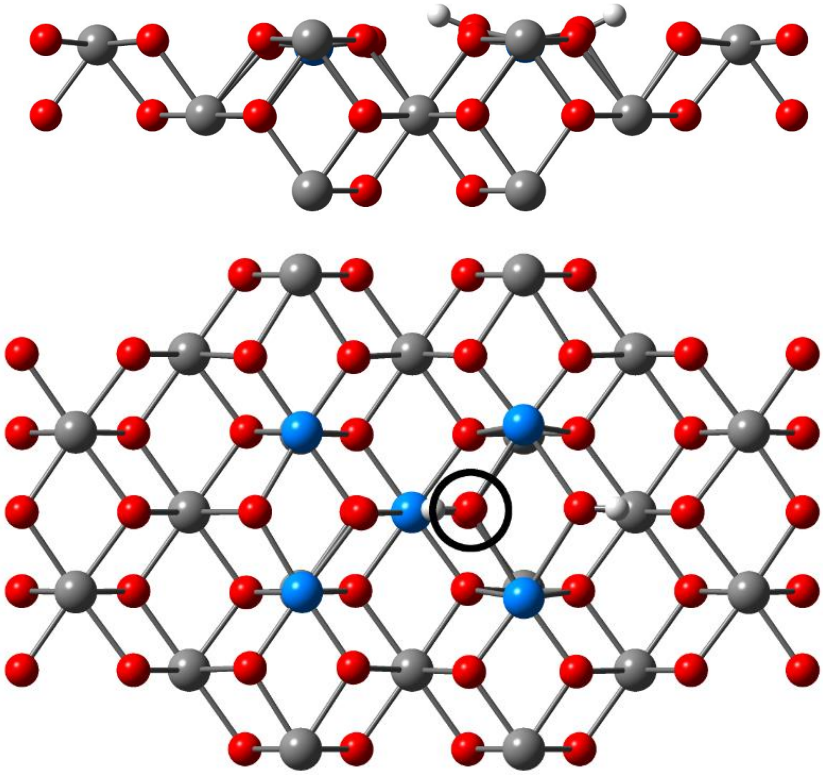

Figure 5.10 Dissociative adsorption of a single water molecule on the (110) surface of a $U_5U_{20}O_{49}$ cluster. Top view shows the cluster in the plane of the surface, while the bottom view is from above the surface. Hydrogen atoms are shown in white, oxygen atoms in red and actinide atoms in blue and grey. Grey spheres represent actinide ions treated with 5f-in-core PPs. The position of the oxygen vacancy is indicated with a black circle. Embedding ions not shown.

A similar geometry is found on the PuO_2 (110) surface, with the oxygens of the hydroxyls lying 0.21 Å and 0.22 Å higher than an oxygen atom in the bulk terminated surface.

The second structure involved placing the hydroxyl group in the same position, but this time placing the additional hydrogen on the other adjacent surface oxygen site (Figure 5.11). In this geometry a hydrogen bond is formed between the two hydroxyl groups, with an OH-OH distance of 1.63 Å. The oxygen atoms of these

hydroxyl groups lie above the surface, being 0.36 Å and 0.67 Å higher than an oxygen atom in the bulk terminated surface.

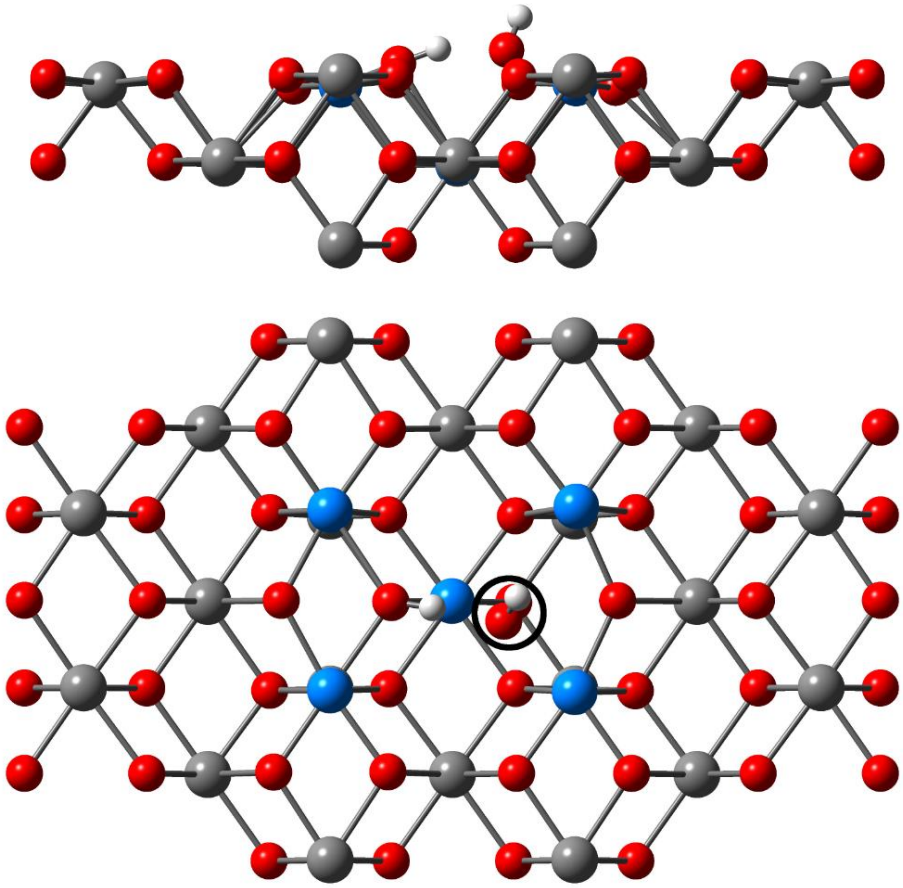

Figure 5.11 Dissociative adsorption of a single water molecule on the (110) surface of a $U_5U_{20}O_{49}$ cluster. Top view shows the cluster in the plane of the surface, while the bottom view is from above the surface. Hydrogen atoms are shown in white, oxygen atoms in red and actinide atoms in blue and grey. Grey spheres represent actinide ions treated with 5f-in-core PPs. The position of the oxygen vacancy is indicated with a black circle. Embedding ions not shown.

A similar geometry was also found on the $Pu_5Pu_{20}O_{49}$ cluster. The OH-OH distance is shorter, at 1.55 Å. The oxygen atoms of the hydroxyl groups lie 0.17 Å and 0.73 Å higher than an oxygen atom in the bulk terminated surface.

Adsorption energies for molecular adsorption and the two types of dissociative adsorption on the UO_2 and PuO_2 (110) surfaces containing an oxygen vacancy are shown in Table 5.4.

	Adsorption Energy/ eV			
	SV(P) + CP		SV(P) + CP + D3	
Adsorption Type	**UO_2**	**PuO_2**	**UO_2**	**PuO_2**
Molecular	-0.81	-1.00	-1.05	-1.36
Dissociative1[a]	-1.83	-2.29	-2.07	-2.62
Dissociative2[b]	-1.02	-1.15	-1.23	-1.45

Table 5.4 Water adsorption energies (eV) on the UO_2 and PuO_2 (110) surfaces modelled as an $An_{25}O_{49}$ cluster within the PEECM. [a] Dissociative1 adsorption occurs with the hydroxyl groups facing away from each other, as shown in Figure 5.10. [b] Dissociative2 adsorption occurs with the hydroxyl groups facing each other, as shown in Figure 5.11.

The adsorption energy for molecular water on the substoichiometric UO_2 (110) cluster is -0.81 eV, this contrasts to -1.06 eV on the stoichiometric surface, so the adsorption energy actually decreases with the presence of an oxygen vacancy.

Bo *et al.* found the opposite trend,[129] they calculated molecular adsorption to be stronger on the substoichiometric surface (by 0.80 eV), however, as discussed in the previous chapter, their molecular adsorption on the stoichiometric surface (Figure 4.3) differs significantly to the one calculated here (Figure 4.10), as well as their own adsorption geometry on the substoichiometric surface (Figure 5.1c). The substoichiometric geometry is, however, similar to ours, therefore they may have found a less stable adsorption geometry on the stoichiometric surface, which led to the much greater increase in energy when there is a vacancy present. Despite this, their value of -1.42 eV is significantly larger than the value of -0.81 eV calculated here on the substoichiometric surface.

The water molecule seems to interact via an electrostatic interaction between the surface uranium atom and the oxygen of the water molecule, as well as a hydrogen bond forming between water and a surface oxygen atom. I wanted to see whether the charges differed between the stoichiometric and substoichiometric surface, to see if this could lead to a decrease in the electrostatic interaction between the surface and the water molecule, and hence to the decrease in the adsorption energy. The natural charges are shown in Table 5.5.

	Natural Charge/ a.u.	
Atom	**$U_{25}O_{50}$ cluster**	**$U_{25}O_{49}$ cluster**
O_W	-0.92	-0.94
H	+0.53	+0.52
H	+0.52	+0.52
U	+1.54	+1.43
O_S	-0.86	-0.90

Table 5.5 Natural charges of an adsorbed water molecule and the surface uranium and oxygen atoms the water coordinates to on a $U_{25}O_{50}$ cluster representation of the UO_2 (110) surface and a $U_{25}O_{49}$ representation, which contains an oxygen vacancy.

The charges on the water molecule differ by small amounts (<0.03 a.u.) between the stoichiometric surface and one containing an oxygen vacancy. The uranium atom – which is coordinated to the vacant oxygen site – has a decrease in its natural charge of 0.11 a.u., which would indeed correspond to a weaker electrostatic interaction between the water molecule and the surface.

For dissociative adsorption, the first type, where the hydroxyls pointed away from each other, is clearly favoured, being more stable by 0.81 eV. This leads to a modest increase of 0.23 eV compared to the stoichiometric surface. The 2nd type of dissociative adsorption leads to a decrease compared to the stoichiometric surface. Although with the 2nd type there is a hydrogen bond is between the two hydroxyls, there are long An-O distances between the 2nd hydroxyl and the actinide ions, which make this adsorption less favourable.

Despite all the key bond distances for molecular adsorption on the PuO_2 (110) surface increasing on the substoichiometric surface from the stoichiometric surface, there is an increase in the adsorption energy, albeit only small (0.06 eV). There is a large increase, however, in the dissociative adsorption compared to the stoichiometric surface (0.95–1.04 eV).

Hence, as on the (111) surface, there is a large difference between the dissociative adsorption energies on UO_2 and PuO_2, with dissociative adsorption being more favourable on the PuO_2 surface. Natural population analysis of the substoichiometric UO_2 (110) surface cluster shows that after dissociative adsorption the two electrons left behind by the oxygen vacancy are localised on two uranium atoms (with spin densities on these atoms of 2.84 and 2.97 a.u., compared to 2.04–2.27 a.u. on the remaining uranium atoms, these data are

shown in Table A.2), compared to before where, as mentioned above, the electrons are spread across three atoms (with spin densities of 2.48–2.95 a.u.). It is worth noting that this does not occur with molecular adsorption on UO_2 (110), the differences between the substoichiometric surface without water and with molecular water adsorbed are small (<0.15 a.u.) and the two electrons remain spread mainly across three uranium atoms (with spin densities on these atoms of 2.50–2.85 a.u.).

Inclusion of dispersion increases the adsorption energies as before, by 0.21–0.24 eV for UO_2, and 0.30–0.36 eV for PuO_2. This further increases the difference between water adsorption on UO_2 and PuO_2.

5.4 Conclusions

I have found that 1st layer oxygen vacancies have lower formation energies than 2nd layer ones, although the difference on the (111) surface is fairly minor (0.01 eV for UO_2, 0.30 eV for PuO_2), it is much more significant on the (110) surface (up to 1.89 eV on PuO_2). As has been seen in other studies on fluorite metal oxide systems, oxygen vacancies are easier to produce on the 1st layer of the (110) surface than the (111) surface, which is related to the lower coordination number of the actinides on the (110) surface than the (111).

The formation energies of oxygen vacancies were much lower on the PuO_2 surfaces than the UO_2, which, as two electrons are left behind when an oxygen vacancy is formed and can reduce the metal ions, could be related to the fact that Pu^{4+} is more easily reduced than U^{4+}.

On the substoichiometric (111) surface there is a clear preference for dissociative adsorption, unlike the stoichiometric surface where dissociative and molecular adsorption have similar energies. This means that reduced surfaces will most likely be hydroxylated. There is a difference between UO_2 and PuO_2, with dissociative adsorption being much weaker on UO_2 – perhaps due to dissociative adsorption causing the additional electrons from the vacancy to be localised on two uranium atoms (they already are localised on two plutonium atoms without the water present). The molecular adsorption energy is similar to the

stoichiometric surface and the difference between the UO_2 and the PuO_2 surfaces are small.

On the (110) surface there is little change in molecular adsorption, while there is again an increase in dissociative adsorption, which leads to a much larger difference between the two for both UO_2 and PuO_2. There is particularly an increase on the PuO_2 surface, which (as on the (111) surface) has higher water adsorption energies than the UO_2 surface. Again this leads to a significant difference in dissociative adsorption energies between the UO_2 and PuO_2 surfaces, which may in part be due to the dissociative adsorption leading the two additional electrons on the substoichiometric surface to localise on two uranium centres (which is already the case without water adsorption for plutonium). This localisation means there is not such a significant gain in the dissociative adsorption energy from the stoichiometric to the substoichiometric surface for UO_2 as there is for PuO_2.

The much larger differences between UO_2 and PuO_2 on the substoichiometric surfaces, in terms of forming oxygen vacancies and dissociative water adsorption, could indicate that UO_2 is not as suitable a surrogate for PuO_2 when defects are present, due to the different redox chemistry of the two systems.

General Conclusions

The study of solid state systems containing actinide elements is challenging, in part due to their complex electronic structure. The PEECM provides a way to perform essentially molecular-level quantum chemical calculations while also approximating the effect of the extended solid state system. This has proved useful in studying the long range electrostatic effects on the electron density topology as well as providing a method of using hybrid functionals to study the strongly correlated actinide dioxide systems. It has also enabled the first study of oxygen vacancies in uranium and plutonium dioxide systems at infinite dilution, and shown the differences between the two systems.

In Chapter 2 it was shown that long range electrostatic effects had little impact on the electron density topology, and hence these effects were unlikely to be the cause of differences found previously between electron densities obtained from gas phase calculations, and those from experiment. Instead the differences could be due to the refinement procedure of the experimental electron density. To test this and extend the work in this thesis, the electron density obtained from theoretical calculations could be put through the experimental refinement procedure, if there was then little difference between the experimental and theoretical electron density topologies, the refinement procedure would clearly be changing the electron density.

The aim of the majority of this thesis has been to probe the interaction of water on plutonium dioxide surfaces, and to compare the adsorption of water to that on uranium dioxide surfaces. A procedure using the PEECM was developed in order to do this; geometry optimisations were performed with the SV(P) basis set, and then the final energy was altered by accounting for the BSSE with the counterpoise correction. This method was justified as, even though the adsorption energies showed a large basis set dependence, similar energies were found between SV(P)+CP calculations and those with just the QZVP basis set. To validate the SV(P)+CP method further, the adsorption energy could be investigated with the QZVP+CP, which should be closer to the SV(P)+CP energy

than just the QZVP calculation, as the BSSE should get smaller as the basis set size is increased.

As has been shown, the PEECM can be applied to both 3D bulk systems, as well as 2D surfaces, with the stable (111) and (110) actinide dioxide surfaces being studied in this thesis. As the unit cell of a system cannot be optimised with the PEECM, the experimental lattice parameters were used in this study. For the same reason the two most stable surface terminations (the (111) and (110)) were chosen, as they will have minor surface reconstructions, and so be similar to the unoptimised bulk surface termination. Less stable surfaces will undergo greater reconstructions, and will differ more from the bulk terminated surface, therefore, to study these surfaces with the PEECM, the surface unit cell should first be optimised, ideally with a periodic DFT calculation. This is currently not possible with Turbomole, whose recently implemented periodic DFT module is not currently compatible with hybrid DFT functionals – it is important the same procedure is used for the unit cell optimisation as is used for the PEECM calculations (i.e. exchange-correlation functional, basis set, etc.)

On the stoichiometric surface, water was found to adsorb similarly on the UO_2 and PuO_2 surfaces, perhaps unsurprisingly given the similar charges of the surface ions, and the similar geometric structure of both types of surface. However, on the substoichiometric surface, differences between water adsorption on UO_2 and PuO_2 surfaces become clear. The redox chemistry of the two systems is already known to differ; plutonium dioxide is more readily reduced than uranium dioxide, while UO_2 easily forms higher oxides (UO_{2+x}), (the existence of PuO_{2+x} has been hypothesised, although is still the subject of much debate). This difference in redox chemistry likely causes the notable difference in water adsorption on substoichiometric oxide surfaces; it would be interesting to see if differences occur on other defect surfaces. Because there is a difference in the oxidation potentials of UO_2 and PuO_2 (as with their reduction potentials), having oxygen interstitial atoms, or additional oxygen atoms adsorbed in the surface would be a particularly interesting defect to model.

For water adsorption, the PEECM has been shown to produce results comparable to those found from periodic DFT studies, and provide additional

insight to actinide systems. There is possibility to extend the work produced in this project to further investigate water adsorption on actinide dioxide surfaces. For example, the PEECM could be used to study other defect or adsorbed species in isolation. One route with particular industrial relevance would be to investigate how chloride ions affect water adsorption – some of the plutonium dioxide stored at Sellafield is known to be contaminated with chloride ions due to the historical use of polyvinyl chloride packaging for PuO_2. The PEECM would be useful for studying the adsorption of charged species, such as chloride ions, as they can be studied at infinite dilution. Although the adsorption of ions can be modelled with periodic DFT (by applying a countercharge to the unit cell), the defect-defect interaction between adsorbed species in neighbouring unit cells will be even greater with a charged species. More generally, the PEECM could be used to study environmentally-relevant molecule-surface interactions, e.g. radionuclides on minerals.

Appendix A - Spin Densities on Uranium Atoms

		Spin Densities/ a.u.			
	Cluster	Stoichiometric $U_{19}O_{38}$	Substoichiometric $U_{19}O_{37}$		
Uranium Atom	**Water adsorption**	No water	No water	Molecular1	Dissociative
1		2.05	2.07	2.10	2.07
2		2.05	2.08	2.07	2.12
3		2.07	2.62	2.64	2.11
4		2.06	3.10	3.04	2.89
5		2.07	2.08	2.08	2.10
6		2.07	2.07	2.07	2.09
7		2.07	2.38	2.40	2.94
8		2.08	2.11	2.10	2.13
9		2.07	2.06	2.06	2.07
10		2.07	2.07	2.07	2.09
11		2.07	2.06	2.06	2.08
12		2.07	2.07	2.07	2.07
13		2.05	2.05	2.05	2.05
14		2.05	2.05	2.05	2.05
15		2.04	2.04	2.04	2.05
16		2.04	2.03	2.03	2.05
17		2.04	2.04	2.04	2.04
18		2.04	2.04	2.04	2.05
19		2.03	2.04	2.04	2.04

Table A.1 Spin densities from natural population analysis of uranium atoms in the (111) surface, on the stoichiometric cluster without water adsorbed, the substoichiometric cluster without water adsorbed, and the substoichiometric cluster with water adsorbed molecularly or dissociatively. The numbering of uranium atoms corresponds to the numbering in Figure A.1. N.B, the ECPs shown in the figure relate to those used for geometry optimisations, spin densities were calculated with small-core ECPs for all uranium atoms.

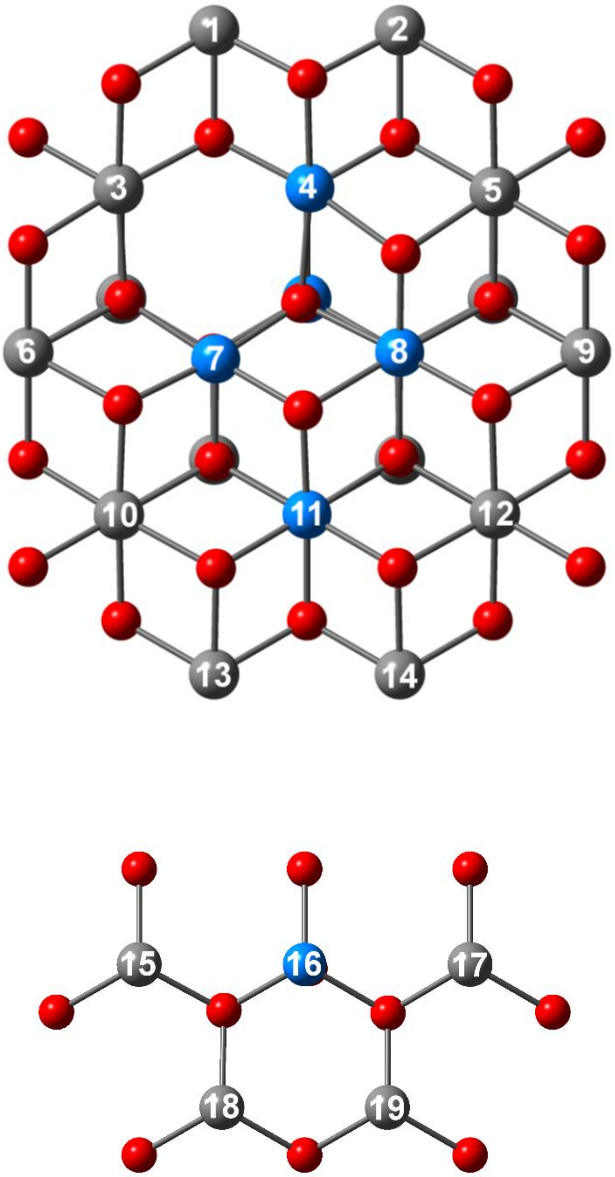

Figure A.1 $U_5U_{14}O_{37}$ cluster containing an oxygen vacancy in the 1st oxygen layer The cluster is viewed from above the (111) surface. The top image shows the entire cluster viewed from above, where the atoms in the 1st stoichiometric (O-An-O) layer can be seen, the bottom image shows the cluster with the 1st stoichiometric layer removed to show the 2nd stoichiometric layer. Oxygen atoms are shown in red and actinide atoms in blue and grey. Grey spheres represent actinide atoms treated with 5f-in-core PPs in the geometry optimisation step. Embedding ions not shown.

		Spin Densities/ a.u.			
	Cluster	Stoichiometric $U_{25}O_{50}$	Substoichiometric $U_{25}O_{49}$		
Uranium atom	**Water adsorption**	No water	No water	Molecular	Dissociative1
1		2.10	2.09	2.10	2.14
2		2.10	2.15	2.11	2.84
3		2.04	2.04	2.04	2.04
4		2.04	2.05	2.05	2.04
5		2.04	2.04	2.04	2.05
6		2.12	2.12	2.12	2.12
7		2.12	2.12	2.11	2.13
8		2.12	2.95	2.85	2.27
9		2.12	2.11	2.12	2.12
10		2.04	2.05	2.05	2.05
11		2.05	2.09	2.13	2.06
12		2.04	2.06	2.06	2.07
13		2.12	2.12	2.12	2.12
14		2.12	2.12	2.13	2.13
15		2.12	2.65	2.50	2.97
16		2.12	2.11	2.12	2.12
17		2.04	2.04	2.04	2.04
18		2.04	2.05	2.05	2.06
19		2.04	2.04	2.04	2.04
20		2.10	2.17	2.28	2.10
21		2.10	2.48	2.54	2.16
22		2.03	2.04	2.04	2.04
23		2.03	2.05	2.05	2.04
24		2.03	2.04	2.04	2.04
25		2.03	2.04	2.04	2.04

Table A.2 Spin densities from natural population analysis of uranium atoms in the (110) surface, on the stoichiometric cluster without water adsorbed, the substoichiometric cluster without water adsorbed, and the substoichiometric cluster with water adsorbed molecularly or dissociatively. The numbering of uranium atoms corresponds to the numbering in Figure A.2. N.B, the ECPs shown in the figure relate to those used for geometry optimisations, spin densities were calculated with small-core ECPs for all uranium atoms.

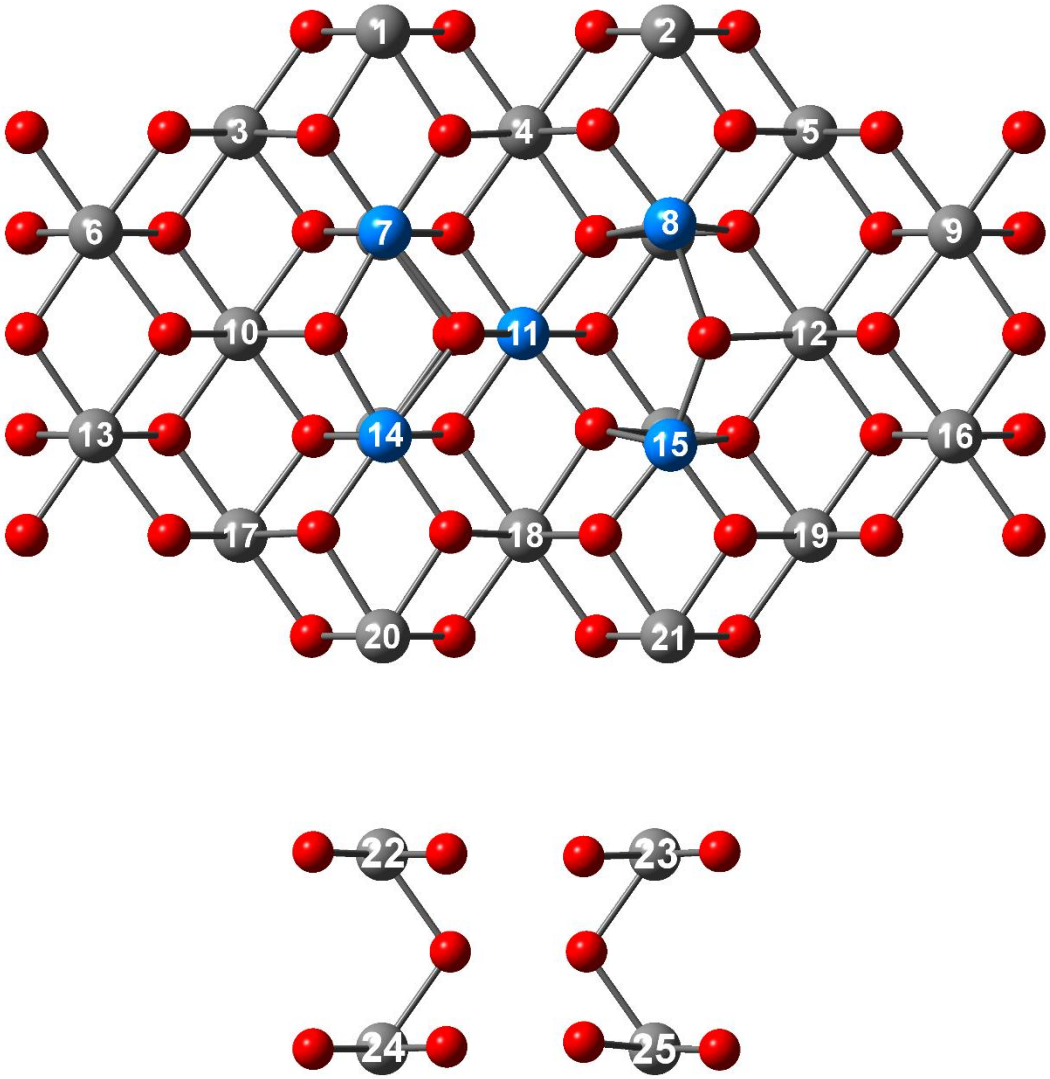

Figure A.2 $U_5U_{20}O_{49}$ cluster containing an oxygen vacancy in the 1st oxygen layer The cluster is viewed from above the (110) surface. The top image shows the entire cluster viewed from above, where the atoms in the 1st and 2nd stoichiometric (O-An-O) layers can be seen, the bottom image shows the cluster with the 1st and 2nd stoichiometric layers removed to show the 3rd stoichiometric layer. Oxygen atoms are shown in red and actinide atoms in blue and grey. Grey spheres represent actinide atoms treated with 5f-in-core PPs in the geometry optimisation step. Embedding ions not shown.

References

1 S. Cotton, *Lanthanide and Actinide Chemistry*, John Wiley & Sons, Ltd, 2006.

2 R. D. Shannon, *Acta Crystallogr. Sect. A*, 1976, **32**, 751–767.

3 J. P. W. Wellington, A. Kerridge and N. Kaltsoyannis, *Polyhedron*, 2016, **116**, 57–63.

4 J. P. W. Wellington, A. Kerridge, J. Austin and N. Kaltsoyannis, *J. Nucl. Mater.*, 2016, **482**, 124–134.

5 J. P. W. Wellington, A. Kerridge and N. Kaltsoyannis, in *WM2016 Proceedings*, 2016.

6 F. Jensen, *Introduction to Computational Chemistry*, Wiley, 2nd ed., 2007.

7 P. Atkins and R. Friedman, *Molecular Quantum Mechanics*, Oxford University Press, 5th ed., 2011.

8 R. G. Parr and W. Yang, *Density-Functional Theory of Atoms and Molecules*, Oxford University Press, 1989.

9 R. F. W. Bader, *Atoms in Molecules: A Quantum Theory*, Clarendon Press, Oxford, 1990.

10 C. F. Matta and R. J. Boyd, in *The Quantum Theory of Atoms in Molecules: From Solid State to DNA and Drug Design*, Wiley, 2007, pp. 1–34.

11 P. Hohenberg and W. Kohn, *Phys. Rev.*, 1964, **136**, B864–B871.

12 W. Kohn and L. Sham, *Phys. Rev.*, 1965, **140**, 1133–1138.

13 J. P. Perdew, K. Burke and M. Ernzerhof, *Phys. Rev. Lett.*, 1997, **78**, 1396–1396.

14 P. Maldonado, L. Z. Evins and P. M. Oppeneer, *J. Phys. Chem. C*, 2014, **118**, 8491–8500.

15 L. Petit, A. Svane, Z. Szotek, W. M. Temmerman and G. M. Stocks, *Phys. Rev. B*, 2010, **81**, 45108.

16 J. P. Perdew, M. Ernzerhof and K. Burke, *J. Chem. Phys.*, 1996, **105**, 9982–9985.

17 P. Pyykkö, *Annu. Rev. Phys. Chem.*, 2012, **63**, 45–64.

18 F. B. van Duijneveldt, J. G. C. M. van Duijneveldt-van de Rijdt and J. H. van Lenthe, *Chem. Rev.*, 1994, **94**, 1873–1885.

19 S. Grimme, *J. Comput. Chem.*, 2004, **25**, 1463–73.

20 S. Grimme, *J. Comput. Chem.*, 2006, **27**, 1787–1799.

21 S. Grimme, J. Antony, S. Ehrlich and H. Krieg, *J. Chem. Phys.*, 2010, **132**, 154104.

22 A. M. Burow, M. Sierka, J. Döbler and J. Sauer, *J. Chem. Phys.*, 2009, **130**, 174710.

23 C. G. Lambert, T. A. Darden and J. A. Board Jr., *J. Comput. Phys.*, 1996, **126**, 274–285.

24 K. N. Kudin and G. E. Scuseria, *Chem. Phys. Lett.*, 1998, **283**, 61–68.

25 K. N. Kudin and G. E. Scuseria, *J. Chem. Phys.*, 2004, **121**, 2886–2890.

26 A. Klamt and G. Schüürmann, *J. Chem. Soc., Perkin Trans. 2*, 1993, 799–805.

27 A. E. Reed, R. B. Weinstock and F. Weinhold, *J. Chem. Phys.*, 1985, **83**, 735–746.

28 F. Furche, R. Ahlrichs, C. Hättig, W. Klopper, M. Sierka and F. Weigend, *Wiley Interdiscip. Rev. Comput. Mol. Sci.*, 2014, **4**, 91–100.

29 T. A. Keith, AIMAll, *TK Gristmill Softw.*, 2014, **14.11.23**.

30 E. I. Solomon, B. Hedman, K. O. Hodgson, A. Dey and R. K. Szilagyi,

Coord. Chem. Rev., 2005, **249**, 97–129.

31 M. L. Neidig, D. L. Clark and R. L. Martin, *Coord. Chem. Rev.*, 2013, **257**, 394–406.

32 J. C. Green and P. Decleva, *Coord. Chem. Rev.*, 2005, **249**, 209–228.

33 M. J. Tassell and N. Kaltsoyannis, *Dalton Trans.*, 2010, **39**, 6719–6725.

34 I. Kirker and N. Kaltsoyannis, *Dalton Trans.*, 2011, **40**, 124–131.

35 M. P. Blake, N. Kaltsoyannis and P. Mountford, *J. Am. Chem. Soc.*, 2011, **133**, 15358–15361.

36 N. Kaltsoyannis, *Inorg. Chem.*, 2013, **52**, 3407–3413.

37 D. D. Schnaars, A. J. Gaunt, T. W. Hayton, M. B. Jones, I. Kirker, N. Kaltsoyannis, I. May, S. D. Reilly, B. L. Scott and G. Wu, *Inorg. Chem.*, 2012, **51**, 8557–8566.

38 M. B. Jones, A. J. Gaunt, J. C. Gordon, N. Kaltsoyannis, M. P. Neu and B. L. Scott, *Chem. Sci.*, 2013, **4**, 1189–1203.

39 D. E. Smiles, G. Wu, N. Kaltsoyannis and T. W. Hayton, *Chem. Sci.*, 2015, **6**, 3891–3899.

40 P. L. Arnold, A. Prescimone, J. H. Farnaby, S. M. Mansell, S. Parsons and N. Kaltsoyannis, *Angew. Chemie Int. Ed.*, 2015, **54**, 6735–6739.

41 R. Beekmeyer and A. Kerridge, *Inorganics*, 2015, **3**, 482–499.

42 A. Kerridge, *Dalton Trans.*, 2013, **42**, 16428–16436.

43 A. Kerridge, *RSC Adv.*, 2014, **4**, 12078–12086.

44 A. C. Behrle, C. L. Barnes, N. Kaltsoyannis and J. R. Walensky, *Inorg. Chem.*, 2013, **52**, 10623–10631.

45 A. C. Behrle, A. Kerridge and J. R. Walensky, *Inorg. Chem.*, 2015, **54**, 11625–11636.

46 A. R. E. Mountain and N. Kaltsoyannis, *Dalton Trans.*, 2013, **42**, 13477–13486.

47 Q.-R. Huang, J. R. Kingham and N. Kaltsoyannis, *Dalton Trans.*, 2015, **44**, 2554–2566.

48 P. Di Pietro and A. Kerridge, *Inorg. Chem.*, 2016, **55**, 573–583.

49 B. B. Iversen, F. K. Larsen, A. A. Pinkerton, A. Martin, A. Darovsky and P. A. Reynolds, *Acta Crystallogr. Sect. B Struct. Sci.*, 1999, **55**, 363–374.

50 V. V. Zhurov, E. A. Zhurova, A. I. Stash and A. A. Pinkerton, *J. Phys. Chem. A*, 2011, **115**, 13016–13023.

51 V. V. Zhurov, E. A. Zhurova and A. A. Pinkerton, *Inorg. Chem.*, 2011, **50**, 6330–6333.

52 V. Vallet, U. Wahlgren and I. Grenthe, *J. Phys. Chem. A*, 2012, **116**, 12373–12380.

53 R. Dovesi, R. Orlando, A. Erba, C. M. Zicovich-Wilson, B. Civalleri, S. Casassa, L. Maschio, M. Ferrabone, M. De La Pierre, P. D'Arco, Y. Noël, M. Causà, M. Rérat and B. Kirtman, *Int. J. Quantum Chem.*, 2014, **114**, 1287–1317.

54 N. K. Hansen and P. Coppens, *Acta Crystallogr. Sect. A Cryst. Physics, Diffraction, Theor. Gen. Crystallogr.*, 1978, **34**, 909–921.

55 P. Macchi, J.-M. Gillet, F. Taulelle, J. Campo, N. Claiser and C. Lecomte, *IUCrJ*, 2015, **2**, 441–451.

56 A. Volkov, P. Macchi, L. J. Farrugia, C. Gatti, P. Mallinson, T. Richter and T. Koritsanszky, XD2006, 2006.

57 A. A. Rykounov, A. I. Stash, V. V. Zhurov, E. A. Zhurova, A. A. Pinkerton and V. G. Tsirelson, *Acta Crystallogr. Sect. B Struct. Sci.*, 2011, **67**, 425–436.

58 A. Volkov, Y. Abramov, P. Coppens and C. Gatti, *Acta Crystallogr. Sect. A*

Found. Crystallogr., 2000, **56**, 332–339.

59 B. Dittrich, S. Scheins, C. Paulmann and P. Luger, *J. Phys. Chem. A*, 2003, **107**, 7471–7474.

60 V. G. Tsirelson, A. I. Stash, V. A. Potemkin, A. A. Rykounov, A. D. Shutalev, E. A. Zhurova, V. V. Zhurov, A. A. Pinkerton, G. V. Gurskaya and V. E. Zavodnik, *Acta Crystallogr. Sect. B Struct. Sci.*, 2006, **62**, 676–688.

61 R. Flaig, T. Koritsanszky, B. Dittrich, A. Wagner and P. Luger, *J. Am. Chem. Soc.*, 2002, **124**, 3407–3417.

62 M. S. Schmøkel, L. Bjerg, F. K. Larsen, J. Overgaard, S. Cenedese, M. Christensen, G. K. H. Madsen, C. Gatti, E. Nishibori, K. Sugimoto, M. Takata and B. B. Iversen, *Acta Crystallogr. Sect. A Found. Crystallogr.*, 2013, **69**, 570–582.

63 C.-C. Wang, T.-H. Tang and Y. Wang, *J. Phys. Chem. A*, 2000, **104**, 9566–9572.

64 J. Henn, D. Ilge, D. Leusser, D. Stalke and B. Engels, *J. Phys. Chem. A*, 2004, **108**, 9442–9452.

65 K. Götz, F. Meier, C. Gatti, A. M. Burow, M. Sierka, J. Sauer and M. Kaupp, *J. Comput. Chem.*, 2010, **31**, 2568–2576.

66 A. S. P. Gomes, C. R. Jacob, F. Réal, L. Visscher and V. Vallet, *Phys. Chem. Chem. Phys.*, 2013, **15**, 15153–15162.

67 R. Ahlrichs, M. Bär, M. Häser, H. Horn and C. Kölmel, *Chem. Phys. Lett.*, 1989, **162**, 165–169.

68 A. D. Becke, *J. Chem. Phys.*, 1993, **98**, 5648–5652.

69 S. H. Vosko, L. Wilk and M. Nusair, *Can. J. Phys.*, 1980, **58**, 1200–1211.

70 J. Tao, J. P. Perdew, V. N. Staroverov and G. E. Scuseria, *Phys. Rev. Lett.*, 2003, **91**, 146401–146404.

71 V. N. Staroverov, G. E. Scuseria, J. Tao and J. P. Perdew, *J. Chem. Phys.*, 2003, **119**, 12129–12137.

72 F. Weigend, M. Häser, H. Patzelt and R. Ahlrichs, *Chem. Phys. Lett.*, 1998, **294**, 143–152.

73 D. A. Pantazis and F. Neese, *J. Chem. Theory Comput.*, 2011, **7**, 677–684.

74 F. Neese, *Wiley Interdiscip. Rev. Comput. Mol. Sci.*, 2012, **2**, 73–78.

75 D. Cremer and E. Kraka, *Angew. Chemie Int. Ed. English*, 1984, **23**, 627–628.

76 Safe Storage of Pu, Sellafield Ltd, http://www.sellafieldsites.com/solution/nuclear-materials/safe-storage-of-pu/, (accessed October 2016).

77 Sellafield Ltd, *Sellafield Plan*, 2011.

78 Department of Energy & Climate Change, *Management of the UK's plutonium stocks*, 2011.

79 M. Paffett, D. Kelly, S. Joyce, J. Morris and K. Veirs, *J. Nucl. Mater.*, 2003, **322**, 45–56.

80 J. M. Haschke, T. H. Allen and L. A. Morales, *Science*, 2000, **287**, 285–287.

81 A. A. Sviridova and N. V. Suikovskay, *Opt. Spectrosc.*, 1967, **22**, 509.

82 B. W. Veal and D. J. Lam, *Phys. Rev. B*, 1974, **10**, 4902–4908.

83 J. Schoenes, *J. Appl. Phys.*, 1978, **49**, 1463–1465.

84 B. W. Veal and D. J. Lam, *Phys. Rev. B*, 1974, **10**, 4902–4908.

85 T. M. McCleskey, E. Bauer, Q. Jia, A. K. Burrell, B. L. Scott, S. D. Conradson, A. Mueller, L. Roy, X. Wen, G. E. Scuseria and R. L. Martin, *J. Appl. Phys.*, 2013, **113**, 13515.

86 I. Prodan, G. Scuseria and R. Martin, *Phys. Rev. B*, 2007, **76**, 33101.

87 L. Cox, W. Ellis, R. Cowan, J. Allen, S. Oh, I. Lindau, B. Pate and A. Arko, *Phys. Rev. B*, 1987, **35**, 5761–5765.

88 S.-W. Yu, J. G. Tobin, J. C. Crowhurst, S. Sharma, J. K. Dewhurst, P. Olalde-Velasco, W. L. Yang and W. J. Siekhaus, *Phys. Rev. B*, 2011, **83**, 165102.

89 A. Seibert, T. Gouder and F. Huber, *J. Nucl. Mater.*, 2009, **389**, 470–478.

90 J. J. Joyce, T. Durakiewicz, K. S. Graham, E. Bauer, D. P. Moore, J. N. Mitchell, J. A. Kennison, T. M. McCleskey, Q. Jia, A. Burrell, E. Bauer, R. L. Martin, L. Roy and G. E. Scuseria, *Mater. Res. Soc. Proc.*, 2011, **1264**, Z09-4.

91 I. D. Prodan, G. E. Scuseria and R. L. Martin, *Phys. Rev. B*, 2006, **73**, 45104.

92 K. Kudin, G. Scuseria and R. Martin, *Phys. Rev. Lett.*, 2002, **89**, 266402.

93 X.-D. Wen, R. L. Martin, T. M. Henderson and G. E. Scuseria, *Chem. Rev.*, 2013, **113**, 1063–1096.

94 S. L. Dudarev, D. N. Manh and A. P. Sutton, *Philos. Mag. Part B*, 1997, **75**, 613–628.

95 S. L. Dudarev, M. R. Castell, G. A. Botton, S. Y. Savrasov, C. Muggelberg, G. A. D. Briggs, A. P. Sutton and D. T. Goddard, *Micron*, 2000, **31**, 363–372.

96 Y. Younsuk, K. Hanchul, K. Heemoon and P. Kwangheon, *Nucl. Eng. Technol.*, 2005, **37**, 293–298.

97 B.-T. Wang, H. Shi, W. Li and P. Zhang, *Phys. Rev. B*, 2010, **81**, 45119.

98 B. Sun, P. Zhang and X.-G. Zhao, *J. Chem. Phys.*, 2008, **128**, 84705.

99 Q. Yin and S. Savrasov, *Phys. Rev. Lett.*, 2008, **100**, 225504.

100 R. Evarestov, A. Bandura and E. Blokhin, *Acta Mater.*, 2009, **57**, 600–606.

101 J.-H. Lan, L. Wang, S. Li, L.-Y. Yuan, Y.-X. Feng, W. Sun, Y.-L. Zhao, Z.-F. Chai and W.-Q. Shi, *J. Appl. Phys.*, 2013, **113**, 183514.

102 I. D. Prodan, G. E. Scuseria, J. A. Sordo, K. N. Kudin and R. L. Martin, *J. Chem. Phys.*, 2005, **123**, 14703.

103 A. Schäfer, H. Horn and R. Ahlrichs, *J. Chem. Phys.*, 1992, **97**, 2571–2577.

104 K. Eichkorn, F. Weigend, O. Treutler and R. Ahlrichs, *Theor. Chem. Acc.*, 1997, **97**, 119–124.

105 A. Moritz, X. Cao and M. Dolg, *Theor. Chem. Acc.*, 2007, **118**, 845–854.

106 W. Küchle, M. Dolg, H. Stoll and H. Preuss, *J. Chem. Phys.*, 1994, **100**, 7535–7542.

107 X. Cao, M. Dolg and H. Stoll, *J. Chem. Phys.*, 2003, **118**, 487–496.

108 T. Bo, J.-H. Lan, Y.-L. Zhao, Y. Zhang, C.-H. He, Z.-F. Chai and W. Shi, *J. Nucl. Mater.*, 2014, **454**, 446–454.

109 Y. Yun, J. Rusz, M. T. Suzuki and P. M. Oppeneer, *Phys. Rev. B*, 2011, **83**, 75109.

110 G. Jomard, B. Amadon, F. Bottin and M. Torrent, *Phys. Rev. B*, 2008, **78**, 75125.

111 Z. Rák, R. C. Ewing and U. Becker, *Surf. Sci.*, 2013, **608**, 180–187.

112 R. B. Ross, S. Gayen and W. C. Ermler, *J. Chem. Phys.*, 1994, **100**, 8145–8155.

113 P. W. Tasker, *J. Phys. C Solid State Phys.*, 1979, **12**, 4977–4984.

114 G. Jomard and F. Bottin, *Phys. Rev. B*, 2011, **84**, 195469.

115 M. Abramowski, S. Redfern, R. Grimes and S. Owens, *Surf. Sci.*, 2001, **490**, 415–420.

116 A. Tan, R. Grimes and S. Owens, *J. Nucl. Mater.*, 2005, **344**, 13–16.

117 S. D. Senanayake and H. Idriss, *Surf. Sci.*, 2004, **563**, 135–144.

118 S. D. Senanayake, G. I. N. Waterhouse, A. S. Y. Chan, T. E. Madey, D. R. Mullins and H. Idriss, *Catal. Today*, 2007, **120**, 151–157.

119 S. D. Senanayake, R. Rousseau, D. Colegrave and H. Idriss, *J. Nucl. Mater.*, 2005, **342**, 179–187.

120 J. M. Haschke and T. E. Ricketts, *J. Alloys Compd.*, 1997, **252**, 148–156.

121 J. L. Stakebake, *J. Phys. Chem.*, 1973, **77**, 581–586.

122 J. L. Stakebake, D. T. Larson and J. M. Haschke, *J. Alloys Compd.*, 1993, **202**, 251–263.

123 J. M. Haschke, T. H. Allen and J. L. Stakebake, *J. Alloys Compd.*, 1996, **243**, 23–35.

124 J. M. Haschke, T. H. Allen and L. A. Morales, *J. Alloys Compd.*, 2001, **314**, 78–91.

125 P. A. Korzhavyi, L. Vitos, D. A. Andersson and B. Johansson, *Nat. Mater.*, 2004, **3**, 225–228.

126 T. Gouder, A. Seibert, L. Havela and J. Rebizant, *Surf. Sci.*, 2007, **601**, L77–L80.

127 F. N. Skomurski, L. C. Shuller, R. C. Ewing and U. Becker, *J. Nucl. Mater.*, 2008, **375**, 290–310.

128 P. F. Weck, E. Kim, C. F. Jové-Colón and D. C. Sassani, *Dalton Trans.*, 2013, **42**, 4570–4578.

129 T. Bo, J. Lan, C. Wang, Y. Zhao, C. He, Y. Zhang, Z. Chai and W. Shi, *J. Phys. Chem. C*, 2014, **118**, 21935–21944.

130 J. C. Boettger and A. K. Ray, *Int. J. Quantum Chem.*, 2002, **90**, 1470–1477.

131 M. Molinari, S. C. Parker, D. C. Sayle and M. S. Islam, *J. Phys. Chem. C*, 2012, **116**, 7073–7082.

132 G. Jomard, F. Bottin and G. Geneste, *J. Nucl. Mater.*, 2014, **451**, 28–34.

133 X. Wu and A. Ray, *Phys. Rev. B*, 2002, **65**, 85403.

134 A. Schäfer, C. Huber and R. Ahlrichs, *J. Chem. Phys.*, 1994, **100**, 5829–5835.

135 F. Weigend, F. Furche and R. Ahlrichs, *J. Chem. Phys.*, 2003, **119**, 12753–12762.

136 J. L. Stakebake and L. M. Steward, *J. Colloid Interface Sci.*, 1973, **42**, 328–333.

137 J. M. Haschke, *J. Nucl. Mater.*, 2005, **344**, 8–12.

138 S. J. Suresh and V. M. Naik, *J. Chem. Phys.*, 2000, **113**, 9727–9732.

139 L.-M. Liu, C. Zhang, G. Thornton and A. Michaelides, *Phys. Rev. B*, 2010, **82**, 161415.

140 D. J. Wesolowski, J. O. Sofo, A. V. Bandura, Z. Zhang, E. Mamontov, M. Předota, N. Kumar, J. D. Kubicki, P. R. C. Kent, L. Vlcek, M. L. Machesky, P. A. Fenter, P. T. Cummings, L. M. Anovitz, A. A. Skelton and J. Rosenqvist, *Phys. Rev. B*, 2012, **85**, 167401.

141 R. Schaub, P. Thostrup, N. Lopez, E. Lægsgaard, I. Stensgaard, J. K. Nørskov and F. Besenbacher, *Phys. Rev. Lett.*, 2001, **87**, 266104.

142 O. Bikondoa, C. L. Pang, R. Ithnin, C. A. Muryn, H. Onishi and G. Thornton, *Nat. Mater.*, 2006, **5**, 189–192.

143 D. Marrocchelli and B. Yildiz, *J. Phys. Chem. C*, 2012, **116**, 2411–2424.

144 H. Xu, R. Q. Zhang and S. Y. Tong, *Phys. Rev. B*, 2010, **82**, 155326.

145 E. Finazzi, C. Di Valentin, G. Pacchioni and A. Selloni, *J. Chem. Phys.*,

2008, **129**, 154113.

146 Z. Yang, T. K. Woo, M. Baudin and K. Hermansson, *J. Chem. Phys.*, 2004, **120**, 7741–7749.

147 M. Ganduglia-Pirovano, J. Da Silva and J. Sauer, *Phys. Rev. Lett.*, 2009, **102**, 26101.

148 S. Fabris, G. Vicario, G. Balducci, S. de Gironcoli and S. Baroni, *J. Phys. Chem. B*, 2005, **109**, 22860–22867.

149 J. Paier, C. Penschke and J. Sauer, *Chem. Rev.*, 2013, **113**, 3949–3985.

150 M. Freyss, T. Petit and J.-P. Crocombette, *J. Nucl. Mater.*, 2005, **347**, 44–51.

151 M. Freyss, N. Vergnet and T. Petit, *J. Nucl. Mater.*, 2006, **352**, 144–150.

152 M. Iwasawa, Y. Chen, Y. Kaneta, T. Ohnuma, H.-Y. Geng and M. Kinoshita, *Mater. Trans.*, 2006, **47**, 2651–2657.

153 P. Nerikar, T. Watanabe, J. S. Tulenko, S. R. Phillpot and S. B. Sinnott, *J. Nucl. Mater.*, 2009, **384**, 61–69.

154 B. Dorado, G. Jomard, M. Freyss and M. Bertolus, *Phys. Rev. B*, 2010, **82**, 35114.

155 B. Ao and H. Lu, *Nucl. Instruments Methods Phys. Res. Sect. B*, 2016, **373**, 102–109.

156 B. Ao, R. Qiu, H. Lu and P. Chen, *Comput. Mater. Sci.*, 2016, **122**, 263–271.

157 B. Sun, H. Liu, H. Song, G. Zhang, H. Zheng, X. Zhao and P. Zhang, *J. Nucl. Mater.*, 2012, **426**, 139–147.

158 T. Bo, J.-H. Lan, Y.-L. Zhao, Y.-J. Zhang, C.-H. He, Z.-F. Chai and W.-Q. Shi, *Surf. Sci.*, 2016, **644**, 153–164.

159 Z. Yang, Q. Wang, S. Wei, D. Ma and Q. Sun, *J. Phys. Chem. C*, 2010, **114**, 14891–14899.

160 M. Fronzi, S. Piccinin, B. Delley, E. Traversa and C. Stampfl, *Phys. Chem. Chem. Phys.*, 2009, **11**, 9188–9199.

161 M. B. Watkins, A. S. Foster and A. L. Shluger, *J. Phys. Chem. C*, 2007, **111**, 15337–15341.

162 M. Nolan, S. C. Parker and G. W. Watson, *Surf. Sci.*, 2005, **595**, 223–232.

163 C. A. Downing, A. A. Sokol and C. R. A. Catlow, *Phys. Chem. Chem. Phys.*, 2014, **16**, 184–195.

164 C. Zhang, A. Michaelides, D. King and S. Jenkins, *Phys. Rev. B*, 2009, **79**, 75433.

165 F. Esch, S. Fabris, L. Zhou, T. Montini, C. Africh, P. Fornasiero, G. Comelli and R. Rosei, *Science*, 2005, **309**, 752–755.

166 Z. Yang, X. Yu, Z. Lu, S. Li and K. Hermansson, *Phys. Lett. A*, 2009, **373**, 2786–2792.

167 W. M. Haynes, Ed., *CRC Handbook of Chemistry and Physics*, CRC Press, 96th ed., 2015.

168 T. Montini, M. Melchionna, M. Monai and P. Fornasiero, *Chem. Rev.*, 2016, **116**, 5987–6041.